VYSOKÉ UČENÍ TECHNICKÉ V BRNĚ

BRNO UNIVERSITY OF TECHNOLOGY

FAKULTA STROJNÍHO INŽENÝRSTVÍ

FACULTY OF MECHANICAL ENGINEERING

ÚSTAV FYZIKÁLNÍHO INŽENÝRSTVÍ

INSTITUTE OF PHYSICAL ENGINEERING

PŘÍPRAVA A TESTOVÁNÍ SNOM SOND SPECIÁLNÍCH VLASTNOSTÍ

PREPARATION AND TESTING OF SNOM PROBES

DIPLOMOVÁ PRÁCE

MASTER'S THESIS

AUTOR PRÁCE — **Bc. JURAJ BOBEK**

AUTHOR

VEDOUCÍ PRÁCE — **prof. RNDr. JIŘÍ SPOUSTA, Ph.D.**

SUPERVISOR

BRNO 2019

VYSOKÉ UČENÍ TECHNICKÉ V BRNĚ
FAKULTA STROJNÍHO INŽENÝRSTVÍ

Zadání diplomové práce

Ústav:	Ústav fyzikálního inženýrství
Student:	**Bc. Juraj Bobek**
Studijní program:	Aplikované vědy v inženýrství
Studijní obor:	Fyzikální inženýrství a nanotechnologie
Vedoucí práce:	**prof. RNDr. Jiří Spousta, Ph.D.**
Akademický rok:	2018/19

Ředitel ústavu Vám v souladu se zákonem č.111/1998 o vysokých školách a se Studijním a zkušebním řádem VUT v Brně určuje následující téma diplomové práce:

Příprava a testování SNOM sond speciálních vlastností

Stručná charakteristika problematiky úkolu:

V současnosti se věnuje velká pozornost studiu povrchů pevných látek a modifikaci jejich vlastností. Kombinace sondových technik (SPM) a elektronové mikroskopie představuje velmi slibnou techniku, která může vést ke zcela novým možnostem přípravy a studia in situ vlastností nanostruktur. Přivést světlo k hrotu SNOM sondy (tvořené dutým vláknem) a zároveň touto sondou transportovat do blízkosti zkoumaného vzorku pracovní plyn (inertní či chemicky aktivní) a to vše v komoře elektrového mikroskopu představuje velmi technicky náročný a originální dosud nikde neřešený úkol.

Cíle diplomové práce:

V rámci práce se budou jednak vyrábět sondy pro techniku Scanning Near–field Optical Microscopy a jednak se budou tyto sondy i testovat z hlediska jejich vlastností (vedení světla a pracovního plynu do blízkosti povrchu vzorku). Zvláštní důraz bude kladen na možnost užití dutých světlovodných vláken k případné modifikaci povrchů pevných látek.

Seznam doporučené literatury:

SLABÝ, V. Příprava a testování SNOM sond se speciálními vlastnostmi, bakalářská práce, VUT v Brně, 2013.

HERTL, V. Příprava a testování SNOM sond se speciálními vlastnostmi, bakalářská práce, VUT v Brně, 2016.

GROSZKOWSKI, J. Technika vysokého vakua, SNTL, Praha 1981.

POLIO, F., CUCINOTTA, A., SELLERI, S. Photonic Crystal Fibers: Properties and Applications, Springer, 2007.

Termín odevzdání diplomové práce je stanoven časovým plánem akademického roku 2018/19

V Brně, dne

L. S.

prof. RNDr. Tomáš Šikola, CSc. ředitel ústavu	doc. Ing. Jaroslav Katolický, Ph.D. děkan fakulty

Abstrakt
Fotonická krystalická vlákna (PCF) představují slibný nástroj pro spojení technik známých z mikroskopie rastrovací sondou, elektronové mikroskopie a systémů pro vstřikování plynu. Přivedení světla a přenos pracovního plynu současně do blízkosti vzorku umístěného uvnitř elektronového mikroskopu přináší nové možnosti experimentů. PCF by mohly být použity nejen k charakterizaci nebo modifikaci struktur na mikroskopické úrovni, ale také k jejich výrobě. Tato práce se zabývá výzkumem literárních zdrojů s tématikou fotonických krystalů s důrazem na PCF. Leptání PCF pomocí kyseliny fluorovodíkové bez poškození jejich vnitřní struktury je experimentálně studováno s velkou precizností. Optické vlastnosti závislé na geometrii PCF jsou testovány pro různé modifikace PCF. Dále se práce zabývá spojením PCF s mikroskopií atomárních sil a následnou integrací do elektronového mikroskopu.

Summary
Photonic crystal fibers (PCF) represents a promising tool for connecting techniques known from scanning probe microscopy, electron microscopy and gas injection systems. To bring light and transfer working gas simultaneously to the vicinity of a sample located inside the electron microscope introduces new possibilities for experiments. PCF could be used not only to characterize or modify structures at microscopic level, but also to fabricate them. This work covers a literature research of photonic crystals with an emphasis on PCF. Etching in hydrofluoric acid of the PCF without damaging its inner structure is experimentally studied with great care. Optical properties dependent on the geometry of the PCF are tested for various modifications of the PCF. Furthermore, the thesis deals with the connection of the PCF with an atomic force microscope and subsequent integration into the electron microscope.

Klíčová slova
fotonický krystal, fotonická krystalická vlákna, mikroskopie atomárních sil, systém vstřikování plynu, optická mikroskopie v blízkém poli

Keywords
photonic crystal, photonic crystal fibers, atomic force microscopy, gas injection system, scanning near field optical microscopy

BOBEK, J.*Příprava a testování SNOM sond speciálních vlastností.* Brno: Vysoké učení technické v Brně, Fakulta strojního inženýrství, 2019. 62 s. Vedoucí prof. RNDr. Jiří Spousta, Ph.D.

I hereby declare that the master thesis Preparation and testing of SNOM probes was written by me, under the supervision of prof. RNDr. Jiří Spousta, Ph.D. I furthermore declare that all the sources of information used in this master thesis are properly quoted.

Bc. Juraj Bobek

My sincere gratitude goes towards my supervisor prof. RNDr. Jiří Spousta, Ph.D., for providing excellent guidance not only on topics concerning the work on this thesis, but also serving as a great mentor for all the things that exceed beyond.

I am thankful to my colleagues and friends that made this work possible. I am thankful to Ondrej Černek for being a good team player. I am thankful to Ing. Zdeněk Nováček, Ph.D., for having a quick wit. I am thankful to Ing. Petr Bábor, Ph.D., for many consultations. I am thankful to Ing. Mgr. Tomáš Šamořil, Ph.D., for immense help. I am thankful to Ing. Zbyněk Dostál, Ph.D., for endless discussions of all things optical.

I am thankful to all the people whom spent their time with me in the laboratories of the Institute of Physical Engineering and made it more enjoyable.

I am thankful to my family for a tremendous support during my studies.

This work was carried out with the support of CEITEC Nano Research Infrastructure (ID LM2015041, MEYS CR, 2016–2019), CEITEC Brno University of Technology.

Financial support from the Thermo Fisher Scientific is gratefully acknowledged.

Bc. Juraj Bobek

Contents

Introduction

A photonic crystal fibers (PCFs), also known as microstructured or holey fibers, are a novel kind of optical fibers. To guide the light, PCFs utilizes a photonic band gap phenomenon which is an essential characteristic of photonic crystals. A photonic band gap acts on a photon in a similar fashion as an electronic band gap acts on an electron. It prohibits some wavelengths of light from passing through the PCF.

PCFs were introduced for the first time in the early 1990s, and manufactured for the first time in the 1996 [1]. As the PCFs provide new ways to control and guide light, they became a major focus area of many research groups in the world. PCFs found their way into the fields such as astronomy, biology, metrology, micromachining, microscopy, telecommunication, sensing, spectroscopy and so on. A variety of scientific papers and books have been published, describing these new fibers, their physics and applications.

Optical properties of photonic crystals depend on the periodic geometry alignment of slabs (each slab is characterized by its dielectric function) which the photonic crystal consists of. Concerning this geometry factor, there are three types of photonic crystals (determined by the number of directions in which the periodicity occurs): one dimensional, two dimensional and three dimensional photonic crystals. In this work, we focus on two dimensional photonic crystals, as PCFs fall into this category of photonic crystals. We briefly mention Bragg fibers which are one dimensional photonic crystals.

In the first chapter we introduce photonic crystals and their optical properties. Then, in the second chapter, we proceed with describing the PCFs. We discuss the guiding mechanism of light, and compare with conventional optical fibers. It is important to state that one type of the periodically arranged slabs in the PCFs that we work with, is simply, air. This hollow type of capillary slabs forming the PCF is utilized as a route for transferring various types of gases along the PCF.

Utilizing the experiences of our colleagues from the Institute of Physical Engineering in the fields of scanning near-field optical microscopy (or scanning probe microscopy in general) and vacuum technology, we aim to combine the PCFs with scanning probe microscopy techniques in order to be able to perform topography measurements (which is the first step of SNOM measurements). Furthermore, we aim to utilize the hollow structure of the PCFs as a gas injection system (or as we name it, NanoGIS). For these purposes, in close collaboration with Mr. Ondrej Černek (currently in his third year of bachelor study period) we developed an experimental station within a scanning electron microscope (Tescan Vega) located in the laboratories of the IPE and performed many experiments.

First step in modification of the PCFs consists in stripping down the protective acrylate coating layer in order to expose the silica cladding of the PCF for the following etching in hydrofluoric acid. This is described in the third chapter. Etching is used in order to thin down the cladding of the PCF to acquire less mass (gluing the PCF onto tuning fork changes its oscillating frequency which is heavily dependent on the mass of the glued object). It turned out that this task is not as simple as one would assumed. We stumbled upon many issues with the etching process. Mainly, underetching the acrylate coating and overetching of the microstructured region of the hollow capillaries. We aimed to tune the etching process as much as possible with little to no ambiguity left, in order to make it repeatable and without much effort. It is possible that in the future we will abandon the etching process (if it turns out that it is not necessary for our application) or try different

approach of thinning down the cladding silica material, e.g. via the grinding process utilizing a grinding wheel. Grinding a D shaped profile of the PCF is implemented for example in article [2].

Next step in modification of the PCFs includes an adjustment the fiber's endpoint. In the fifth chapter, we discuss the process of attaching a SNOM probe onto a solid core of a PCF. This SNOM probe is made from conventional optical fiber using Turner etching method [3].

Final step consists in gluing the etched PCF onto the tuning fork. We are using tuning forks that are common in the field of SPM with known parameters. Basically, there are two options on how the PCF will be glued onto the tuning fork; either the PCF will be put alongside one arm of the tuning fork or perpendicular to it. Whilst the first option results in oscillations of the PCF parallel with the surface of the sample (shear mode), the second option results in oscillations perpendicular to the surface of the sample. For the SNOM, the shear mode is more common, however we are using SPM NenoVision LiteScope [4], where currently the shear mode is not fully implemented. Additional limitation consists in a limited space due to integration of the SPM in Tescan Vega SEM, we are limited in the height from the sample to the objective of the electron microscope. Thus, care must be taken in designing the probe holder and the way we are gluing the PCF onto the tuning fork.

1. Photonic crystals

In this chapter we introduce a photonic crystals (PCs). In short, PCs are a marriage of solid-state physics and electromagnetism. According to their geometrical structure, there are one dimensional, two dimensional and three dimensional PCs. Simple schemes representing each type of the PC are shown in the figure 1.1. We discuss Maxwell's equations of electromagnetism and Bloch-Floquet theorem, in order to introduce a photonic bandgap (PBG). The PBG represents a range of frequencies of the light, that are prohibited from guiding through the PC. Main sources of the information provided in this chapter are from publications [5] and [6].

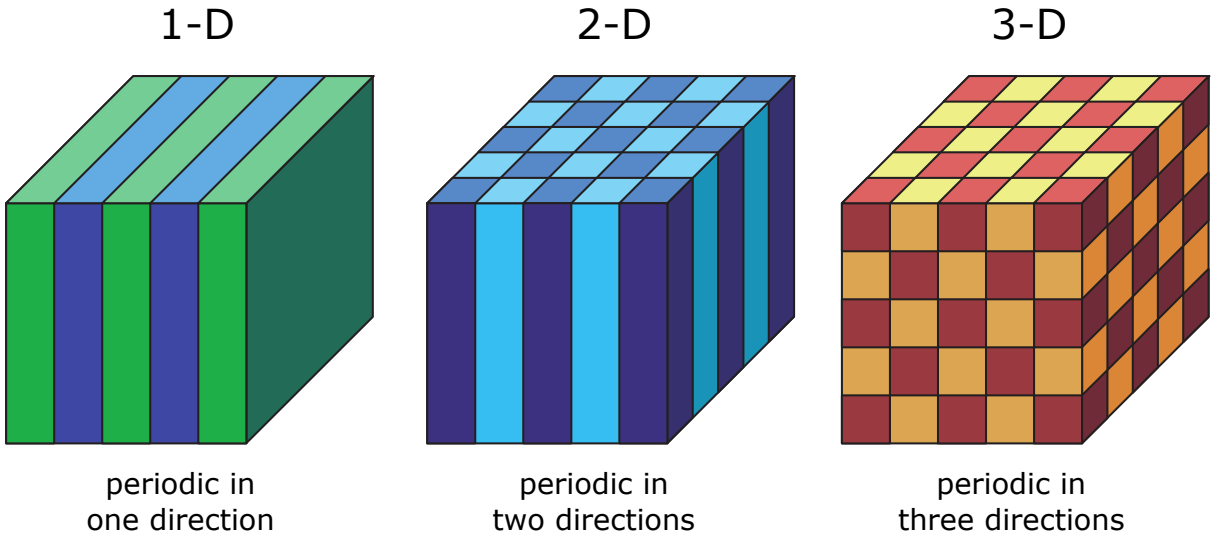

Figure 1.1: A simple schemes representing photonic crystals implemented in one, two and three dimensions. Periodically arranged materials, each with a different dielectric constant, are distinguished by color. Adapted from [5].

1.1. Maxwell equations revision

In this section we review the Maxwell equations which are necessary to study the propagation of light in the PCs. We will derive an equation Eq.(1.12) which in combination with the symmetry principles of a periodically arranged systems, gives rise to the PBG. The Maxwell equations expressed in SI units [7] have the following form:

$$\vec{\nabla} \times \vec{E} = -\frac{\partial \vec{B}}{\partial t}, \tag{1.1}$$

$$\vec{\nabla} \times \vec{H} = \vec{J} + \frac{\partial \vec{D}}{\partial t}, \tag{1.2}$$

$$\vec{\nabla} \cdot \vec{D} = \rho, \tag{1.3}$$

$$\vec{\nabla} \cdot \vec{B} = 0, \tag{1.4}$$

where $\vec{E}$ and $\vec{H}$ are the macroscopic electric and magnetic fields, respectively. $\vec{D}$ and $\vec{B}$ are the electric and magnetic induction fields, respectively. $\vec{J}$ is the free current density,

ρ is the free charge density. All of these are potentially functions of the position and time. We assume these 4 approximations. First, the field strengths are small enough, so that any non-linearity effects can be neglected. Second, the mixed dielectric material is macroscopic and isotropic. Third, there is no frequency dependence of the dielectric function ϵ_r. Fourth, the dielectric function ϵ_r is purely real and positive. With these 4 approximations, we obtain a relations between the macroscopic and microscopic fields:

$$\vec{D} = \epsilon_0 \epsilon_r \vec{E}, \tag{1.5}$$

$$\vec{B} = \mu_0 \mu_r \vec{H}. \tag{1.6}$$

For most dielectric materials, μ_r is close to 1, in that case, ϵ_r is the square of the refractive index n ($n = \sqrt{\epsilon_r}$). In optics we are interested in the cases, where no currents or charges are present. Thus, combining Eq.(1.5) and Eq.(1.6) with the Maxwell equations yields:

$$\vec{\nabla} \times \vec{E} = -\mu_0 \frac{\partial \vec{H}}{\partial t}, \tag{1.7}$$

$$\vec{\nabla} \times \vec{H} = \epsilon_0 \epsilon_r \frac{\partial \vec{E}}{\partial t}, \tag{1.8}$$

$$\vec{\nabla} \cdot \epsilon_r \vec{E} = 0, \tag{1.9}$$

$$\vec{\nabla} \cdot \vec{H} = 0. \tag{1.10}$$

Combining Eq.(1.7) with Eq.(1.8), we eliminate $\vec{E}$ and obtain an equation for $\vec{H}$ only (similarly, we can obtain an equation for $\vec{E}$):

$$\vec{\nabla} \times \left(\frac{1}{\epsilon_r} \vec{\nabla} \times \vec{H} \right) = -\epsilon_0 \mu_0 \frac{\partial^2 \vec{H}}{\partial t^2}. \tag{1.11}$$

We are considering only solutions that are harmonic in time, with their dependence on time as $\mathrm{e}^{-i\omega t}$. Thus, if we put $c = 1/\sqrt{\epsilon_0 \mu_0}$, we can change the Eq.(1.11) into:

$$\vec{\nabla} \times \left(\frac{1}{\epsilon_r} \vec{\nabla} \times \vec{H} \right) = \left(\frac{\omega}{c} \right)^2 \vec{H}. \tag{1.12}$$

This equation represents a Hermitian eigen-value problem over an infinite domain, and generally produces a continuous spectrum of eigen-frequencies ω [6]. This equation together with the divergence equations from the Maxwell equations (Eq.(1.9) and Eq.(1.10)) tells us everything we need to know about $\vec{H}$. Solving this equation for a given structure ϵ_r, gives us the eigen-modes of $\vec{H}$ and the corresponding eigen-frequencies. If we consider the case of a periodically arranged dielectric structure ϵ_r, things become much more interesting. To solve this problem, one could take advantage of some of the results from quantum mechanics, such as the orthogonality of modes, variational theorem or perturbation theory. The reason, why the Eq.(1.12) is expressed with $\vec{H}$ instead of $\vec{E}$, is of mathematical convenience, numerical calculations are simpler. To recover $\vec{E}$ from $\vec{H}$, we use Eq.(1.8):

$$\vec{E} = \frac{\mathrm{i}}{\omega \epsilon_0 \epsilon_r} \vec{\nabla} \times \vec{H}. \tag{1.13}$$

To conclude, the left side of the Eq.(1.8), that is $\left(\vec{\nabla}\times\frac{1}{\epsilon_r}\vec{\nabla}\times\right)$, represents an eigen-operator. The term $\left(\frac{\omega}{c}\right)^2$ represents an eigen-value (or eigen-frequency) and $\vec{H}$ represents an eigen-mode. The eigen-operator is a Hermitian operator, this means that the eigen-frequencies ω are real, eigen-modes are orthogonal and eigen-modes are complete (they give all solutions).

1.2. Bloch-Floquet theorem revision

In this section we review a topics concerning the consequences of a periodically arranged systems. If the eigen-operator is a periodic function of position, then the Bloch-Floquet theorem[1] applies [8], and the solution to such Hermitian eigen-problem is again, periodic function:

$$\vec{H}\left(\vec{r},t\right)=e^{i\left(\vec{k}\cdot\vec{r}-\omega t\right)}\vec{H}_{\vec{k}}\left(\vec{r}\right), \tag{1.14}$$

where $\vec{H}_{\vec{k}}\left(\vec{r}\right)$ is a periodic function of position, it is a periodic envelope of the planewave represented by the term $e^{i\left(\vec{k}\cdot\vec{r}-\omega t\right)}$. The right side of Eq.(1.14) represents a Bloch wave. Because $\vec{k}$ is conserved quantity, there is no scattering of the Bloch wave. Because $\vec{H}_{\vec{k}}\left(\vec{r}\right)$ is given by finite unit cell, eigen-frequencies ω are discrete and ω becomes $\omega_n\left(\vec{k}\right)$. When the eigen-frequencies are plotted as a function of $\vec{k}$, they form a dispersion curves which is shown in the figure 1.2, it represent a map of what states could exist and can interact.

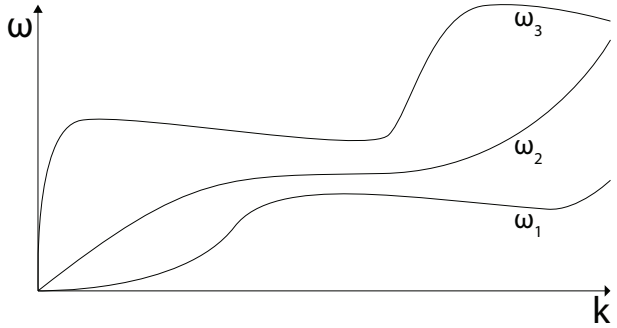

Figure 1.2: A dispersion diagram showing a splitting of the dispersion curves into a sets of curves, each representing one eigen-mode.

When we substitute Eq.(1.14) into Eq.(1.11), we find:

$$\left(\vec{\nabla}+\mathrm{i}\vec{k}\right)\times\frac{1}{\epsilon_r}\left(\vec{\nabla}+\mathrm{i}\vec{k}\right)\times\vec{H}_{\vec{k}}=\left(\frac{\omega}{c}\right)^2\vec{H}_{\vec{k}}, \tag{1.15}$$

which satisfies the reduced Hermitian eigen-problem.

This equation in combination with the orthogonality of the eigen-functions and a fact, that the lowest band solves a variational problem, are forming the gap in the dispersion diagram, i.e. a photonic bandgap.

[1]The Bloch-Floquet theorem is proven as the translation operator of the crystal lattice commutes with the Hermitian operator [9] or [10].

This knowledge can be utilized for computing PBGs. For example, a simple case of an one dimensional PC is realized in a form of a multilayer film (or Bragg reflector). The system is periodic in the z direction, and homogeneous in the xy plane. A scheme showing a multilayer film is shown in the figure 1.3.

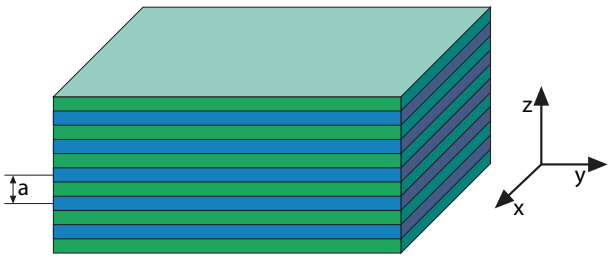

Figure 1.3: The multilayer film, a one-dimensional photonic crystal. The system consists of alternating layers of materials (blue and green) with different dielectric constants, with a spatial period a. We imagine that each layer is uniform and extends to infinity along the x and y directions, and we imagine that the periodicity in the z direction also extends to infinity. Adapted from [5].

The PBG of such multilayer flim is shown in the figure 1.4. The dielectric constants are ϵ_h=13 and ϵ_l=1. The widths of the layers are 0.2a and 0.8a, respectively.

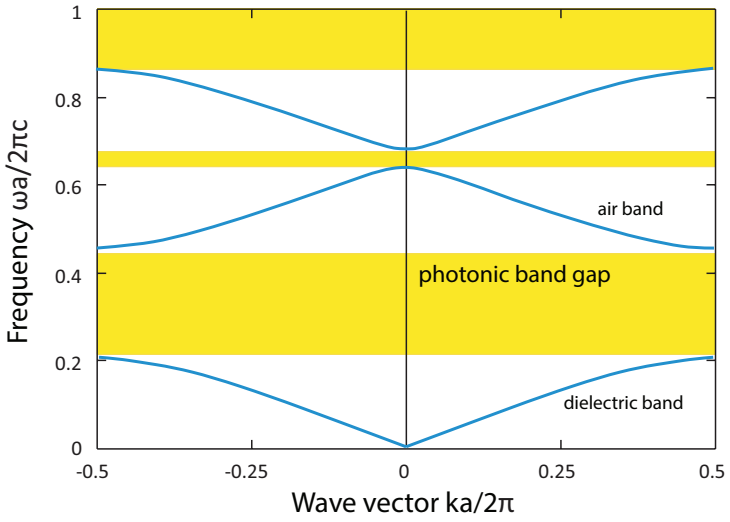

Figure 1.4: The photonic band structure of a multilayer film with lattice constant a and alternating layers of different widths. The width of the ϵ_h=13 layer is 0.2a, and the width of the ϵ_l=1 layer is 0.8a. Adapted from [5].

1.3. Applications

In this section we introduce several examples of PCs's applications. The PCs were first introduced in 1987 in articles considering the works in the fields of strong localization of light [11] and inhibition of spontaneous emission [12]. In this works it was shown that the specific arrangement of periodically repeated dielectric structures acts as a optical barrier and for certain frequencies the propagation of light can be suppressed.

Although, one could think that the approximations used to derive relations between the macroscopic and microscopic Maxwell equations were too constraining, use of a perturbation theory can make up for it and introduce several interesting phenomena. Point defects can create resonant cavities, line defects can create waveguides. For example, lossless bends are utilized through line defects [13], transmission through such material is shown in the figure 1.5.

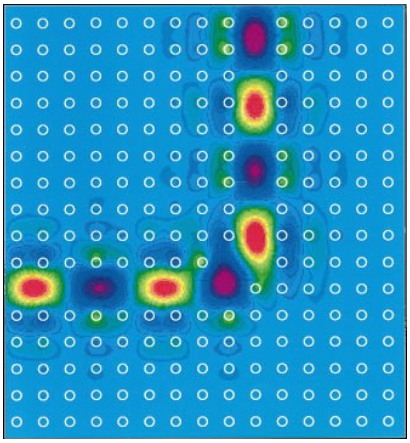

Figure 1.5: Electric field pattern in the vicinity of the bend for frequency $\omega = 0.353 \times 2\pi c/a$. The electric field is polarized along the axis of the dielectric columns. Adapted from [13].

Interesting application of the PCs reaches into optical computing. The PCs can be used as a logic gates (NOT, AND, OR, etc.) or optical memory. An implementation of a NOT gate using a PC by exploiting its optical nonlinearity, is shown in the figure 1.6. The presence of an optical pulse at the input gives no light at the output, and the absence of an optical pulse gives light at the output of the waveguide. Thus, the presence of a pulse at the input denotes a logical one, and the absence of a pulse denotes a logical zero [14].

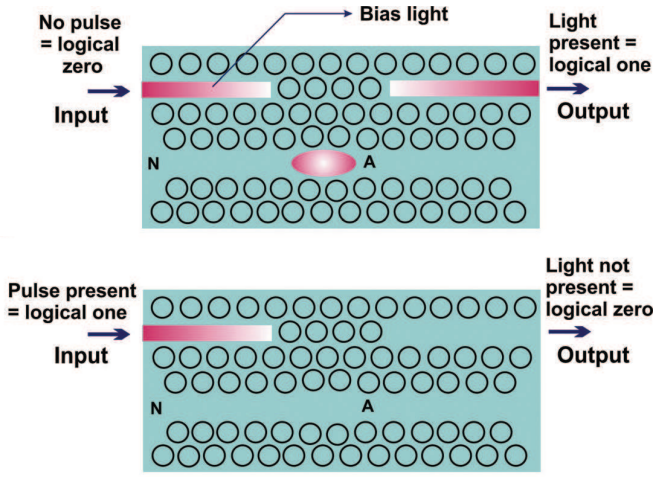

Figure 1.6: Implementation of NOT operation using a photonic crystal slab. Adapted from [14].

2. Photonic crystal fibers

In this chapter we aim to describe a basic working principles of the photonic crystal fibers (PCFs). The main source of information will be a publications [15] and [16]. We briefly discuss optical guiding properties of the PCFs. After that, we describe the manufacturing process of the PCFs, following by a various examples of applications.

A simple schemes shown in the figure 2.1 demonstrate a various types of the optical fibers that currently exist. Besides conventional optical fibers, there are three main types of the PCFs: Bragg fibers, photonic bandgap (hollow-core) fibers and index guiding (solid-core) photonic crystal fibers. The PCFs could be divided into a more specialized groups, however as we are working only with the basic types of the PCFs, these groups are not examined any further[1]. A more detailed schemes and explanation for each type of the optical fiber is presented in the following text in this chapter. Bragg fibers are considered only as a curiosity in the next paragraph.

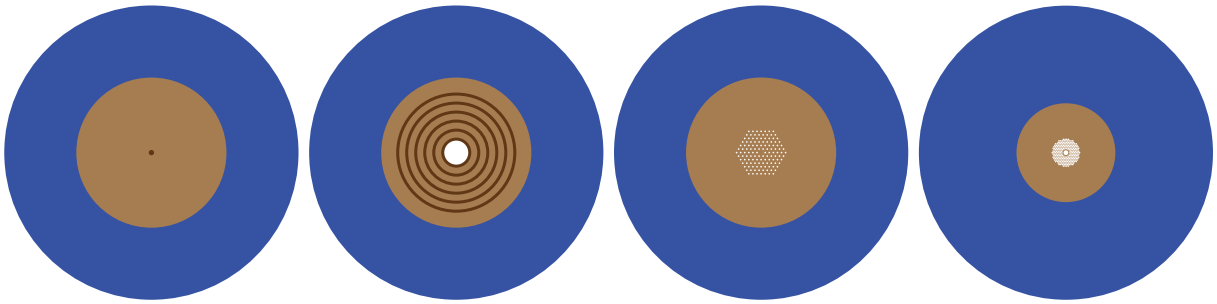

Figure 2.1: A schemes of various types of optical fibers. From the left to the right scheme: conventional optical fiber, Bragg fiber, solid-core PCF, hollow-core PCF. Blue layer represents a protective acrylate layer, brown layer is the cladding. Microstructured regions of the PCFs are visible. More detailed and descriptive schemes are presented further in this chapter.

Bragg fibers, sometimes called OmniGuide[2] fibers, represent an one dimensional type of the PCFs with a periodicity of the dielectric layers realized only in a radial direction. Naturally, the Bragg fibers utilize a device called the Bragg mirror (or a multilayer reflector) as a cladding of the optical fiber [17]. A Bragg mirror is the simplest device using the principles of the photonic crystals only in a one direction. It consists of a periodic stack of two alternating dielectric layers. These two alternating layers are visible in the appropriate scheme in the figure 2.1. The core of such fibers may or may not be hollow. Theoretical studies have shown that a hollow-core Bragg fibers could be feasible, given the possibility of attaining a large refractive index contrasts between the successive layers [18]. Indeed, the first working experimental hollow-core Bragg fiber has already been demonstrated, and had in some wavelength ranges losses that are orders of magnitude smaller than any conventional optical fiber [19].

[1] A curious reader could find a vital information e.g. in the mentioned publications [15] and [16].
[2] Named after the manufacturing company.

2.1. Optical properties

There are three mechanisms that could be utilized in guiding the light through an optical fiber. For conventional fibers, total internal reflection is used. For PCFs, either modified total internal reflection is used in solid-core PCFs or photonic bandgap guidance is used in hollow-core PCFs.

Firstly, we briefly mention the conventional optical fibers as we are using them for some of the test experiments.

2.1.1. Conventional optical fibers

Conventional optical fibers use a total internal reflection mechanism to guide the light. In the rest of this work, we refer to the conventional optical fibers as a SM600 fibers[3] [20].

A scheme of the SM600 fiber is shown in the figure 2.2. The fiber consists of a three layers: core, cladding and coating. An optical signal propagates through the core which has a higher index of refraction than the cladding and thus assuring total reflection at the core-cladding interface. Both, the core and the cladding, are made of a silica glass, however the core is doped to assure higher index of refraction. The coating has a protective function and is made out of acrylate. Some of the parameters of the SM600 fibers are listed besides the scheme in the figure 2.2. The manufacturer does not provide the core diameter, however provides the mode field diameter for light with wavelength of 633 nm. These fibers are also called index guiding fibers.

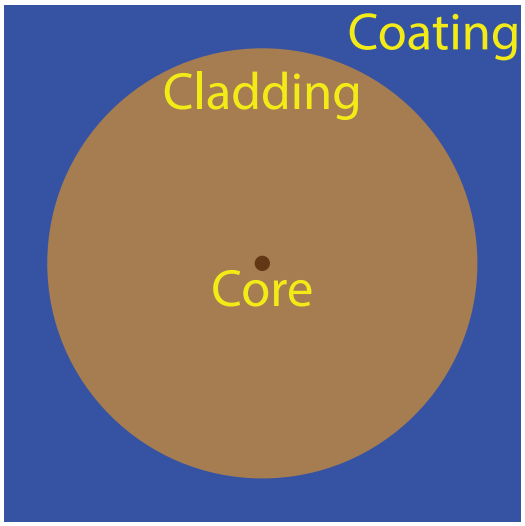

Fiber parameter	Value	Note
Coating diameter	245 µm	
Cladding diameter	(125 ± 1) µm	
Mode field diameter	(3.6 - 5.3) µm	At 633 nm
Coating material	Dual acrylate	
Numerical aperture	0.10-0.14	Nominal

Figure 2.2: A scheme of a conventional optical fiber, with a codename SM600. A table containing a list of important parameters of the fiber is included.

[3] Their codename is selected after the manufacturer, we gave codenames for the other two types of the fibers as well.

2.1.2. Solid-core PCFs

Solid-core PCFs, sometimes called an index guiding holey fibers, use a modified total internal reflection mechanism to guide the light. In the rest of this work, we refer to the solid-core PCFs as a LMA5 fibers [21].

A scheme of the LMA5 fiber is shown in the figure 2.3. Some of the parameters of the LMA5 fibers are listed besides the scheme in the figure 2.3. The numerical aperture holds true for a light with a wavelength of 1064 nm.

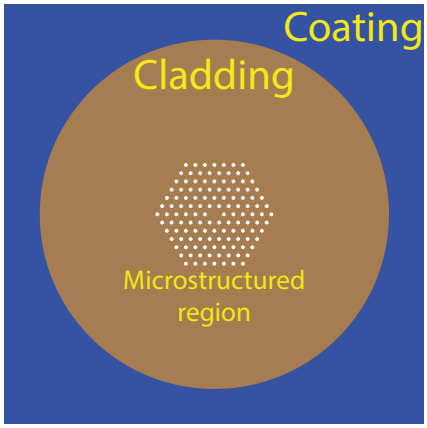

Fiber parameter	Value	Note
Coating diameter	(245 ± 10) µm	
Cladding diameter	(125 ± 2) µm	
Core diameter	(5 ± 0.5) µm	
Microstructured region	approx. 40 µm	
Coating material	Acrylate	
Numerical aperture	0.2 ± 0.02	at 1064 nm

Figure 2.3: A scheme of a solid-core PCF, with a codename LMA5. A table containing a list of important parameters of the fiber is included.

LMA5 fibers guide light by utilizing a two dimensional PCF as a cladding. Although, the periodic structure is not implemented for its PBG. As the cladding has a cross section that is filled with a triangular lattice of air holes and the core is solid, the average index of the cladding is lower. Therefore, LMA5 fibers guide light through a modified form of total internal reflection. Because the cladding is composed of a mixture of silica and air, which have high dielectric contrast, the LMA5 fibers exhibit a strong optical confinement. This is utilized e.g. for enhancing nonlinear effects or creating unusual dispersion phenomena.

The LMA5 fibers have a endlessly single-mode property, even for short wavelengths. A proper geometry design of the cladding allows that only the fundamental mode is guided [22]. This can be utilized to design large-mode area fibers, which can be employed for high power delivery, amplifiers and lasers. By doping the core to reduce its refractive index for shorter wavelengths, the guiding can be turned off completely.

2.1.3. Hollow-core PCFs

Hollow-core PCFs use a photonic bandgap guidance mechanism to guide the light. In the rest of this work, we refer to the solid-core PCFs as a HC532 fibers [23].

A scheme of the HC532 fiber is shown in the figure 2.4. Some of the parameters of the HC532 fibers are listed besides the scheme in the figure 2.4. The numerical aperture holds true for a light with a wavelength of 532 nm.

HC532 fibers utilize a PBG to confine light, rather than the index guiding phenomenon. Bandgap confinement allows light to be guided within its hollow core. This reduces the effects of losses, nonlinearities and other effects that are with bulk materials. First such a fiber was introduced by Knight et al. [24] in 1998 and its scheme is shown in the figure 2.5.

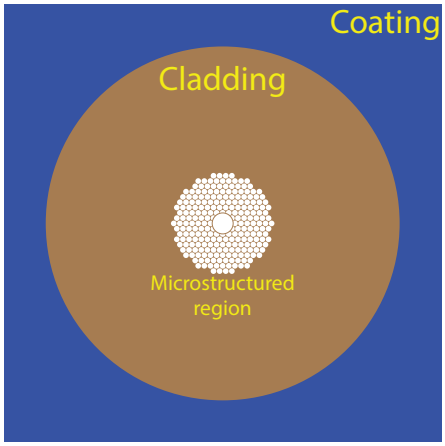

Fiber parameter	Value	Note
Coating diameter	(241 ± 20) µm	
Cladding diameter	(81 ± 5) µm	
Core diameter	(4.8 ± 0.5) µm	
Microstructured region	approx. 23 µm	
Coating material	Acrylate	
Numerical aperture	0.2	at 532 nm

Figure 2.4: A scheme of a hollow-core PCF, with a codename HC532. A table containing a list of important parameters of the fiber is included.

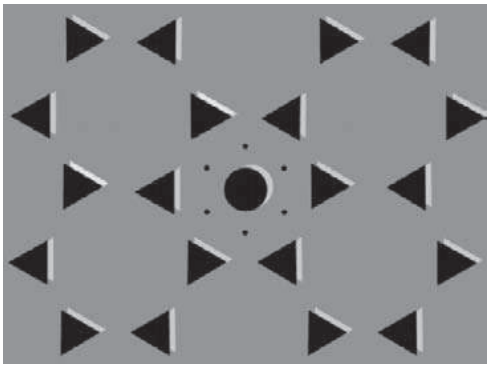

Figure 2.5: Schematic of the cross-section of the first photonic bandgap PCF with a honeycomb air-hole lattice, adapted from [24].

2.2. Fabrication

In this section, we discuss the fabrication process of the PCFs. There are two major methods to fabricate the PCFs: Stack-and-draw technique and extrusion fabrication process.

The stack-and-draw technique was introduced by Birks et al. in 1996 [25]. First, the preform of the fiber is created, which represents the macroscopic version of the desired structure. The preform is realized by stacking a capillary silica tubes and rods to form the desired air-silica structure, as shown in the figure 2.6. Then, the preform is drawn down on a fiber-drawing tower, extending its length and reducing its cross section, from a diameter of 20 mm to a (80-200) μm one. The fibers are drawn at the temperatures around 1900 °C. During the fabrication, parameters such as time dynamics, temperature and pressure, are being controlled.

This method allows a high level of flexibility in the design of the preform. Both, the core size and shape can be controlled, as well as the profile of the cladding region. An example of a PCF's cross section is shown in the figure 2.7, the preform consists of a solid, empty and doped glass regions. This method is used in fabrication of the hollow-core PCFs [26].

The extrusion fabrication process enables formation of a silica-air preforms, that are not attainable by stacking capillaries. In the preform fabrication process, a molten glass

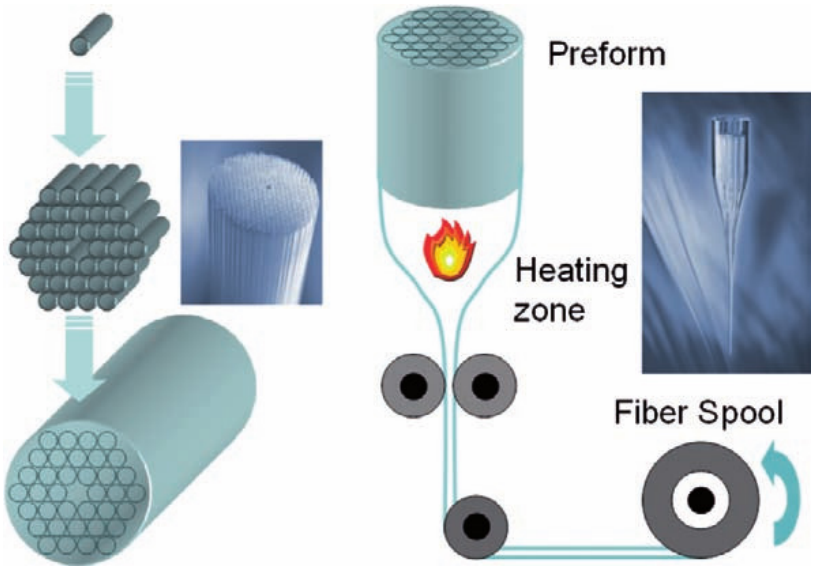

Figure 2.6: Scheme of the PCF fabrication process. Adapted from [15].

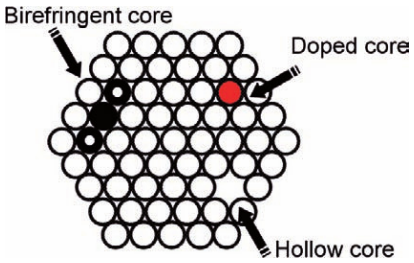

Figure 2.7: Example of a PCF's cross section. Adapted from [15].

if forced through a die containing a pattern of designed holes. Using this method almost any structure can be produced, whether crystalline or amorphous. Using this method, the first non-silica glass PCF was manufactured in 2002 by Kiang et al. [27]. The three-step procedure used for manufacturing a highly nonlinear PCF is shown in the figure 2.8. In the first step, a preform and jacket tube are extruded. In the second step, the preform is reduced to a cane on a fiber-drawing tower. In the last step, the cane is inserted into the jacket tube, which is drawn down to the final fiber.

Besides these two methods, it is worth to mention that there are microstructured polymer optical fibers and OmniGuide fibers. The microstructured polymer optical fibers have been presented and fabricated in 2001 [28]. The mechanism of guiding a light is the same as in PCFs. They are drawn under relatively low temperatures associated with polymers, e.g. polymethyl methacrylate. The fabrication process is presented in article [29], and the air-hole pattern is drilled into the preform using CNC mill. The OmniGuide fibers are manufactured using a cigar-rolling technique [19].

2.3. Applications

In this section we briefly mention some of the more interesting applications in which the PCFs find their versatility. In the article written by Wu et al. [30], the authors are

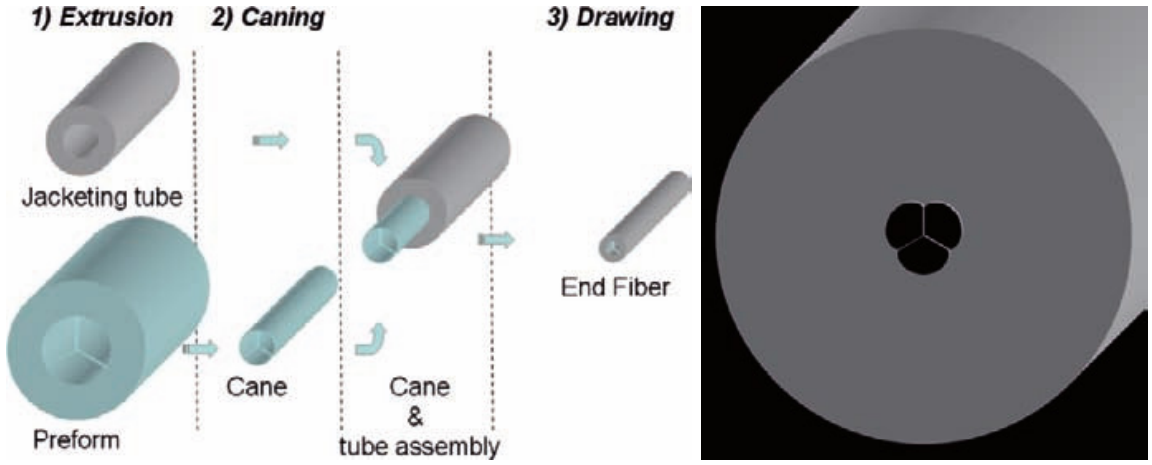

Figure 2.8: Scheme of the fabrication process of the extruded SF57 glass PCF in the left image. Schematic of the cross section of the fiber in the right image. Adapted from [26].

manufacturing a D-shaped sensor made from PCF. The sensor is shown in the figure 2.9. The Au film that is deposited onto the PCF's polished surface is used as a surface plasmon resonance sensor (SPR). The authors are investigating the influence of the polished depth, air hole size, lattice constant and refractive index on the sensing abilities. The authors also show an approach how such polishing is being accomplished by the grinding process.

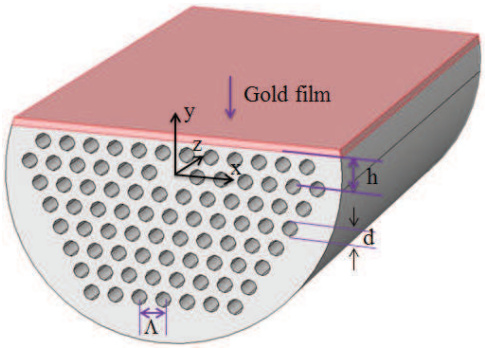

Figure 2.9: Schematic diagram of the SPR sensor based on D-shaped photonic crystal fiber in 3D model. The PCF polished surface is perpendicular to the y axis. Adapted from [30].

The article written by Vaiano et al. [31] represents a roadmap for various "Lab on Fiber" technologies and devices, in which the most interesting for us is the lab in fiber category. Most of the applications in the article are focusing on a biosensing. The authors cited in the article are using solid and hollow-core PCFs mostly for surface-enhanced Raman scattering. One of the most interesting techniques presented in the article, uses a controlled melt-filling technique for creating a metal nanowires directly in the solid-core PCF's capillaries. This way we could manufacture a tip on the PCF's endpoint which would be utilized in AFM. This technique was presented by Schmidt et al. [32] in 2011, and the process of manufacturing such nanowires is shown in the figure 2.10.

Initially, a metal wire is inserted in a single hole silica tube. Then the capillary containing the wire is spliced to a PCF. By heating the spliced section to the melting temperature of Au (around 1064 °C) and by applying at the same time a high pressure

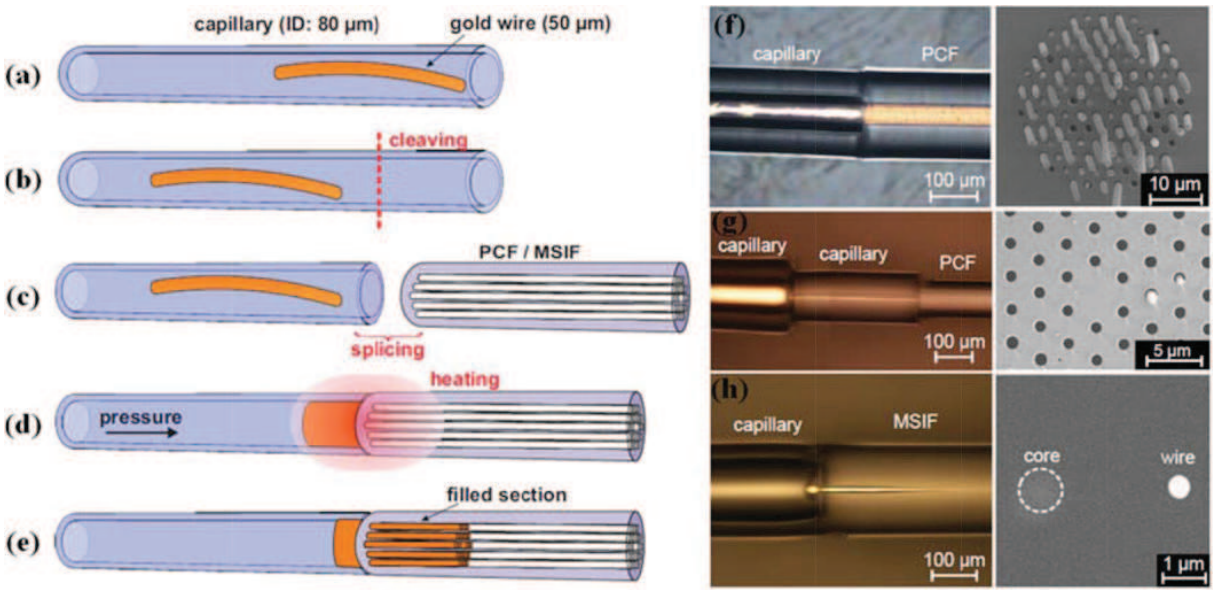

Figure 2.10: (a-e) Schematics of the technique used to create a metal nanowires directly in PCF capillaries. (f-h) Microscope image of the splicing point (side view) and SEM images of the fiber end-faces: (f) a solid-core-PCF with all its channels filled with Au, (g) a PCF selectively filled with Au, (h) a conventional fiber with a parallel Au nanowire. Adapted from [32].

argon gas through the second end of the capillary, the Au melts and infiltrates within the PCF holes. Fine temperature control is needed to avoid the holes collapse, which can occur at the softening temperature of silica (about 1400 °C). Clearly, the set of materials that can be infiltrated with this technique is limited by their melting temperature. The metal filled PCFs exhibited dips in transmission spectrum due to the excitation of surface plasmons at the metal-glass interface. Finally, the authors also demonstrated the possibility to fill with Au just two holes by using the selective filling technique based on a single hole capillary [32].

3. Hydrofluoric acid etching

First step in the modification of the PCF consists in etching the silica cladding layer of the PCF in the 40% hydrofluoric (HF) acid. In order to etch the silica cladding, it is necessary to remove the acrylate coating of the PCF. This could be done by using a standard layer stripping tool [33] (scissors-like tool), available e.g. from ThorLabs. This tool is shown in the figure 3.1. The reason why we are etching the cladding is to lower the diameter of the PCF. This cuts down the time that is necessary to apply further modifications to the PCF, e.g. etching by the focused ion beam. Another reason to etch the cladding is to lower the PCF's weight. Because the PCF is being glued to the tuning fork that is used in a scanning probe microscope, we do not want to alter the weight of the tuning fork (and the weight distribution), as it could negatively interfere with the tuning fork's oscillations.

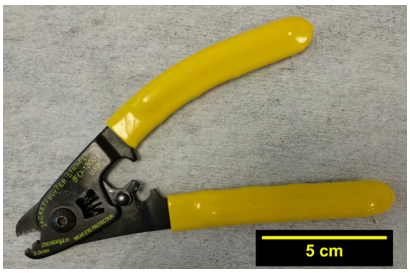

Figure 3.1: A photograph of the layer stripping tool used to strip down the acrylate coating of the fibers used in this work.

As it was previously discussed in this work, there are three types of the optical fibers used: conventional optical fibers (SM600), solid-core PCF (LMA5) and hollow-core PCF (HC532). With the stripping tool, the easiest fibers to strip down the acrylate coating are the SM600 fibers. Considering the LMA5 fibers, the stripping is slightly more difficult than stripping down the SM600 fibers, but still manageable, despite both having almost the same coating and cladding diameters. The difference could originate from the fact that the SM600 fibers have a double acrylate layer as a coating. On the other side, the HC532 fibers, due to different cladding diameter than the rest of the fibers, are a challenge to strip down. The stripping tool can not strip down the acrylate coating completely, there always remain some leftovers. To fully strip down the HC532 fibers, it is necessary to use a scalpel. The scalpel is used in a way that its razor edge is set perpendicular to the PCF's cladding, and is moved along the PCF's cladding with a slight pressure applied. This process is shown in the figure 3.2.

In order to not expose the microstructured region of the PCF directly to the HF acid, we decided to strip down the acrylate coating in the middle of the fiber and then etch this stripped down part of the fiber. This is shown in the figure 3.3. The proposed method of etching the fiber in the middle is not conventional, however at the moment represents the only feasible option. In our experiments with the HF acid etching we used a two slightly different approaches. In our first approach we inserted the PCF into the HF acid even to its acrylate coating, thus the HF acid could rise under the acrylate coating and underetch it. This is not desirable, as it will be shown later in the text. In our second approach, we aimed to reduce the underetching of the acrylate coating as much as possible.

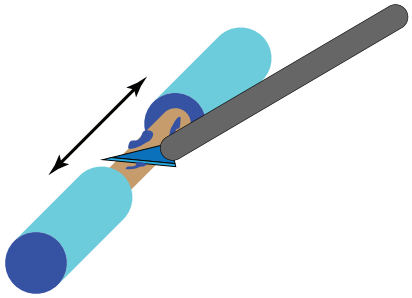

Figure 3.2: A scheme representing a principle of removing the acrylate leftovers from the PCF using a scalpel. The PCF has already been stripped down with the use of a stripping scissors. The blue part represents the acrylate layer, the brown part represents the cladding of the PCF.

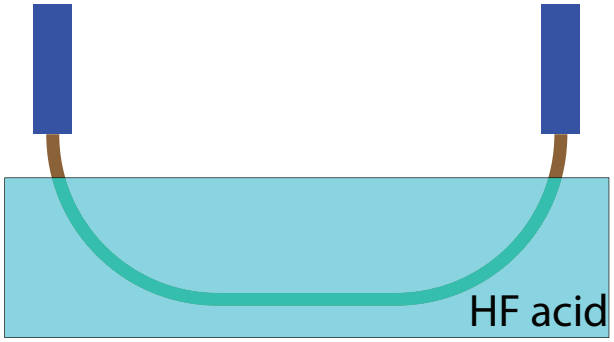

Figure 3.3: A scheme representing the HF acid etching process of the PCF. The stripped down PCF is inserted into the HF acid in a way that there is not contact of the PCF's microstructured region with the HF acid.

One could etch the endpoint of the fiber, if this endpoint would have been covered with a HF acid resistant material, for example by PMMA. We did not want to use this approach of gluing the fiber's endpoint in order to not introduce any glue leftovers to the remaining, etched fiber. Because a glue could rise, due to the capillary forces along the fiber and thus, be present. One could perhaps strip down a longer part of the fiber, glue the endpoint, etch the fiber in the HF acid and cut the remaining fiber far enough, where there is no residual glue left. However, the PCFs are quite expensive, thus we are abandoning this technique. Another issue is the rising of the HF acid under the glue itself, thus we would have to glue a longer part of the fiber's endpoint, so the HF acid can not underetch it and damage the microstructured region.

Another option on how to reduce the cladding diameter, is to use a grinding tool, which is used e.g. for making a D-shaped form of the fiber (used e.g. for biosensing applications [31]). Making a D-shaped fiber is perhaps less difficult problem than reducing the diameter of the fiber by etching in the HF acid. However it would be necessary to rotate the fiber along its axis and then slightly push the grinding wheel against the rotating fiber in order to reduce the cladding equally. In the article [30], authors are grinding the PCF with a grinding apparatus and checking the amount of the removed cladding material via an optical throughput of the PCF while grinding the cladding even down to the microstructured region. In our case, we want to keep the microstructured region intact, thus this optical throughput method would possibly not be viable, as the optical

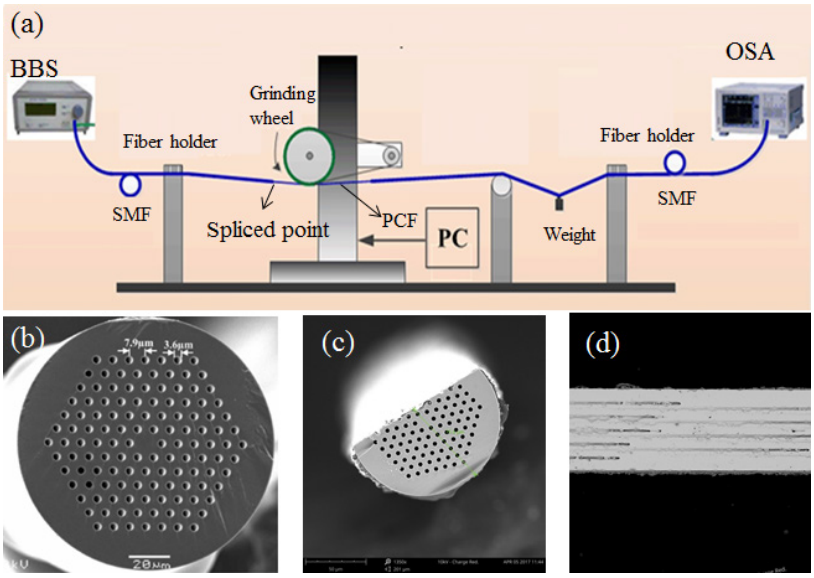

Figure 3.4: (a) Optical fiber side-polished system. (b) SEM image of the PCF before polishing. (c) The cross section of the D-shaped PCF with gold-coated. (d) The side-polished surface of the D-shaped PCF with gold-coated. Adapted from [30].

throughput could not depend on the amount of removed cladding material as much. A scheme representing the grinding process for manufacturing the D-shape out to the PCF is shown in the figure 3.4. Authors use a broadband light source (BBS) with a range from 1250 nm to 1650 nm and an optical spectrum analyzer (OSA) are employed to online monitoring the transmission spectrum during the polishing process. The PCF's polished surface is gently cleaned using an air-laid paper with water to remove residual silica dust. The polishing process is stopped at the stage when the polishing surface appears near the PCF's core region and with a power loss of approximately 3 dB in air [30].

As it was said previously, in our first approach we were inserting the PCFs to the HF acid even with its acrylate coating. This led to underetching of the acrylate coating. A Tescan Vega SEM images of an underetched and not underetched (result of the second approach to the HF acid etching) acrylate coating of the LMA5 fibers are shown in the figure 3.5. The underetching not only makes the whole etching part more chaotic, it seems almost impossible to predict how much of the HF acid will rise under the acrylate. Next, it makes a little space between the etched fiber and its acrylate layer, which could interfere with the oscillations of the fiber. This could be resolved with gluing the underetched acrylate coating, however as it was mentioned, we aim to remove any sort of glues applying onto the fiber. We decided that we aim to minimize the possible contact of the HF acid with the acrylate layer (in our second approach to the HF acid etching). Another issues arise from the HF acid having a low boiling point, thus it evaporates more easily. Even when the acrylate coating is not in direct contact with HF acid, the HF acid vapors could reach the acrylate and underetch it. This was especially an issue when the air conditioning system in the laboratory was down. When the ambient temperature was higher, it was clear that the usual etching times were too high, the etching process was faster and the HF acid reached the microstructured region. Moreover, there was a smaller amount of the HF acid left in the etching beaker after the etching, because of the increased evaporation rate.

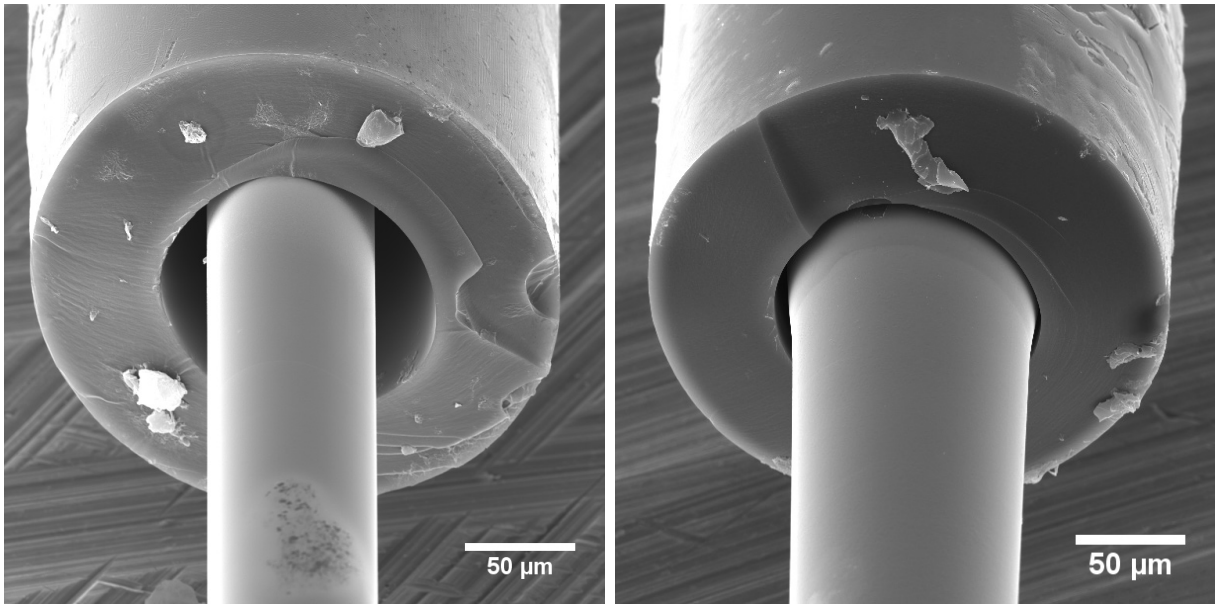

Figure 3.5: SEM image of an underetched acylate coating of the LMA5 fiber is in the left image (result of the first approach). Not underetched one is in the right image (result of the second approach).

Another issue could consist in making the cladding too thin, from the experiments performed in this work it seems that the optical throughput of the PCFs is not limited by the amount of removed cladding, however thin cladding could lead to an increased risk of a potential mechanical breakage of the fiber.

In our first attempt to etch the fibers, we made a simple PTFE holder for the fibers, shown in the right image of the figure 3.6. We locked the fiber in the PTFE holder and then inserted it into the PTFE beaker, shown in the left image of the figure 3.6. The maximum length that the acrylate coating could have been stripped down was determined by the spacing between the arms of the PTFE holder, that is up to 25 mm. It is clear that using this approach, the acrylate coating is fully inserted into the HF acid which leads to its underetching.

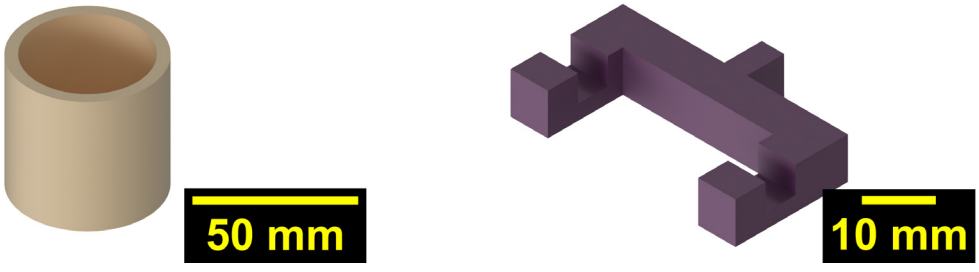

Figure 3.6: Our first attempt to etch the fibers. A PTFE beaker is in the left image and a PTFE holder is in the right image. The fiber is inserted into the holder and locked, then it is inserted into the PTFE beaker.

To estimate, how much time it will require to etch the cladding of the PCFs, we run an experiment where we were etching SM600 fibers, as its cladding is made of the same material as the cladding of the PCFs. We etched the SM600 fibers several times and for

each etching, we increased the etching time. We proposed that the speed of the etching of a cylindrical component should be constant during the etching process. However, there are some assumptions that we did not put in our considerations. We neglected the fact, that the ability to etch of the HF acid slightly drops down during the etching, whether it is because the HF acid looses its power, or it evaporates. Another assumption that we did not put in our considerations is concerning the etching of a cylinders with a diameters that are too low, the etching might be different. Let us imagine that the speed of the etching is proportional to the surface area of the component that is being etched. For a cylindrical component, that is the surface of its shell, thus:

$$v \propto S = 2\pi rh, \tag{3.1}$$

where v is the etching rate, r is the radius of the cylinder, h is its height and S is its shell area.

Analogous to a relation between velocity rate of an object, time interval and change of its position:

$$\mathrm{d}t = \frac{\mathrm{d}x}{v}, \tag{3.2}$$

we could assume that a similar relation holds true for etching rate of a cylindrical component, if we put a change of volume of the cylindrical component as the change of position, so $\mathrm{d}x = \mathrm{d}V = 2\pi rh\mathrm{d}r$. This results in a relation:

$$\mathrm{d}t \propto \frac{2\pi rh\mathrm{d}r}{2\pi rh} = \mathrm{d}r. \tag{3.3}$$

The amount of the etched material of a cylindrical component expressed as a reduction of its radius is linearly proportional to the time it took to etch it. We test this assumption and it holds true at least to some extend.

We made a two measurements showing a dependence of the diameter of the SM600 fiber's cladding on the etch time. In both measurements, the etching volume was 8 ml and we removed a 1 cm long part of the acrylate coating. In the first set of values, we set the etch times up to 40 min, see upper graph in the figure 3.7. The fibers were not coated with the Au layer, thus the fibers were charging in the SEM. Due to this charging, the measured diameters could be incorrect. As this can be seen in the value of the diameter of the fiber, that was not etched (in the graph, etch time = 0 min). This value does not agree with the value stated in its datasheet. Nevertheless, the linear proportionality emerges.

Then we proceeded to make a measurement of the fibers that were coated with the Au layer[1], however with etch times only up to 20 min, see bottom graph in the figure 3.7. If we look at the diameter of the non etched SM600 fiber, we see that it agrees with the value stated in its datasheet. Thus, the assumption on the linear dependence of the reduced diameter of the fiber's silica cladding on the etch time is confirmed and we could use this values to predict the etch times that are necessary to reduce the diameter of the PCF's cladding. However, this was tested only with a 1 cm long acrylate coating removed and with the acrylate coating fully immersed in the HF acid. Thus, when etching a longer cladding, the etch times could be slightly higher relative to the values given in the experiment and should be taken into consideration.

[1] After the etching procedure.

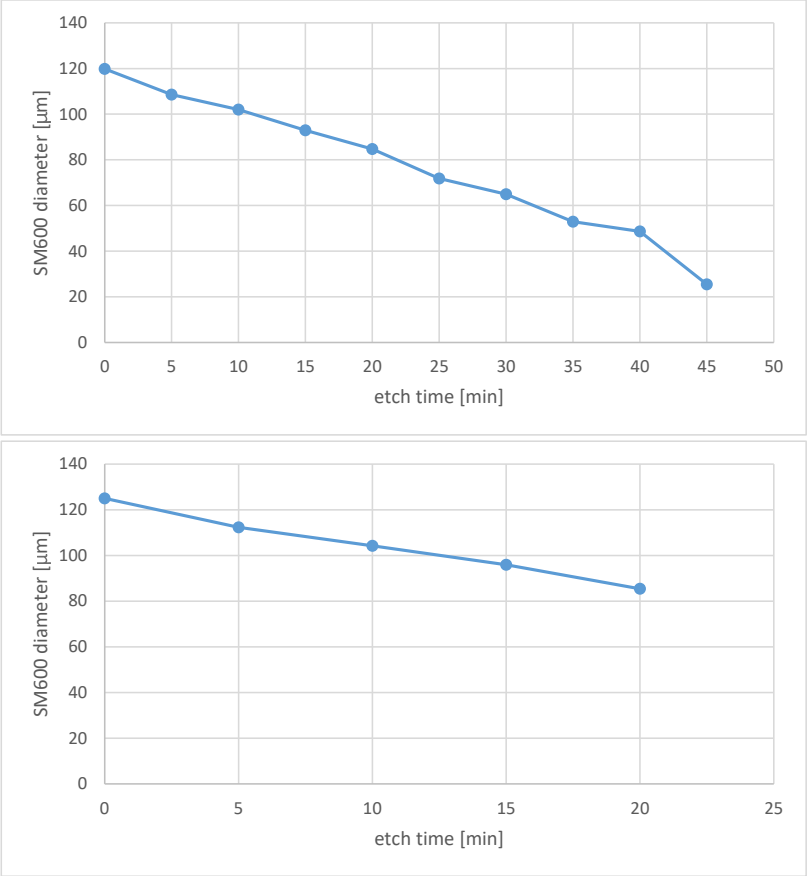

Figure 3.7: Above, etching of the SM600 fiber's cladding that was not coated with an Au layer after the etching procedure. Bellow, etching of the SM600 fiber's cladding that was coated with an Au layer after the etching.

As it was mentioned, we came to a conclusion that underetching of the acrylate coating is undesired and we decided, that we remove a larger portion of the acrylate coating, and that it is not in direct contact with the HF acid. The PTFE beaker for implementing this requirement is shown in the figure 3.8.

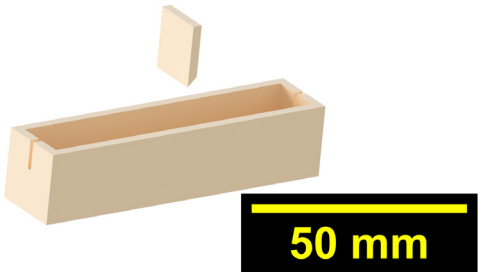

Figure 3.8: The PTFE beaker used in the second approach to the HF acid etching decreases the negative effect of underetching of the acrylate coating.

The fibers that are being etched in this beaker have a 60 mm long part of the acrylate coating stripped down. The stripped fibers are put into the sockets that are located at the opposite sides of the beaker. Then the fiber is locked using a PTFE locking bit, that is

inserted into the beaker and a slight force is applied against the fiber. This way, only the cladding is immersed in the HF acid. Although, the rising of the HF acid is still present (probably can not be removed absolutely), the underetching of the fiber is reduced. There are still HF acid vapors that could underetch the acrylate coating, this could be resolved by inserting the beaker inside a gas chamber filled with a inert gas of a higher pressure, or by blowing the inert gas at the beaker. This beaker allows (the previous one too) etching of a long enough fibers, that after the etching is done, the etched fibers can be cut in half, and thus obtain two etched fibers in one sessions. However, because of stripped acrylate coating being longer, possibility of breaking the fiber is increased, thus caution is required. Implementing this approach to the etching, the only remaining variables in the etching process are the ambient temperature, which should be stable, as long as the air conditioning system works. In the etched fibers, there is a transient area located at the acrylate coating cut, approx. 10 mm long, where the cladding is reduced from its default diameter to that of the desired one. Then, in the rest of the etched fiber, the diameter of the cladding stays constant.

We tested this beaker only with the LMA5 fibers, as we were sadly informed by the manufacturer, that they canceled selling their HC532 model. In our first attempt, we set the etching time according to the previous experiments to 35 minutes, which it turned out is the right etching time to reach its microstructured region. We consecutively etched another LMA5 fiber and the result was the same, i.e. the etching is reproducible. The results of etching the both LMA5 fibers are in the figure 3.12. This figure also shows the quality of the cut of the fibers. The cutting of the fibers is discussed in the next section.

3.1. PCF cutting

After the HF acid etching process, the fibers are cut using a fiber cleaver tool [34]. The cleaver is shown on the photograph in the left image of the figure 3.9. The process of the cutting is shown in the scheme on the right image of the figure 3.9.

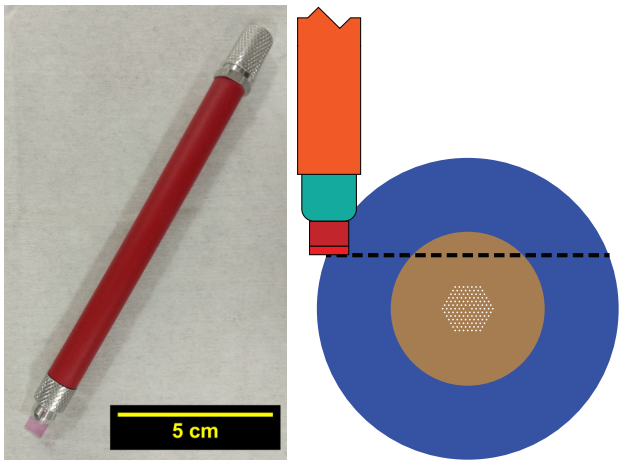

Figure 3.9: The fiber cleaver is in the left photograph. A scheme showing the cutting process of the fibers is in the right image.

The idea is to make an one cut, perpendicular to the fiber and then bend the fiber in a way, that it naturally breaks. When making the cut, it is important not to cut through

the fiber completely. This process is for the PCFs tedious, as one could easily damage the microstructured region. Also, this process is easier, if the fiber is stripped down of its acrylate coating, as we can have visual confirmation of the cut. When we are cutting through the acrylate coating, we can not tell if we cut through the acrylate coating or not.

The quality of the cut has a major effect on the optical output of the fiber. This is especially true for the PCF, because of their microstructured region. A comparison between a properly and not-properly cut PCF is in the following figures. First, we compare the four cuts of the LMA5 fiber which are shown in the figure 3.10. A Tescan Vega SEM was used to acquire this images. This fibers were not etched, they were only cut, and serve as an examples of the cutting quality. They have been also stripped down of their acrylate coating.

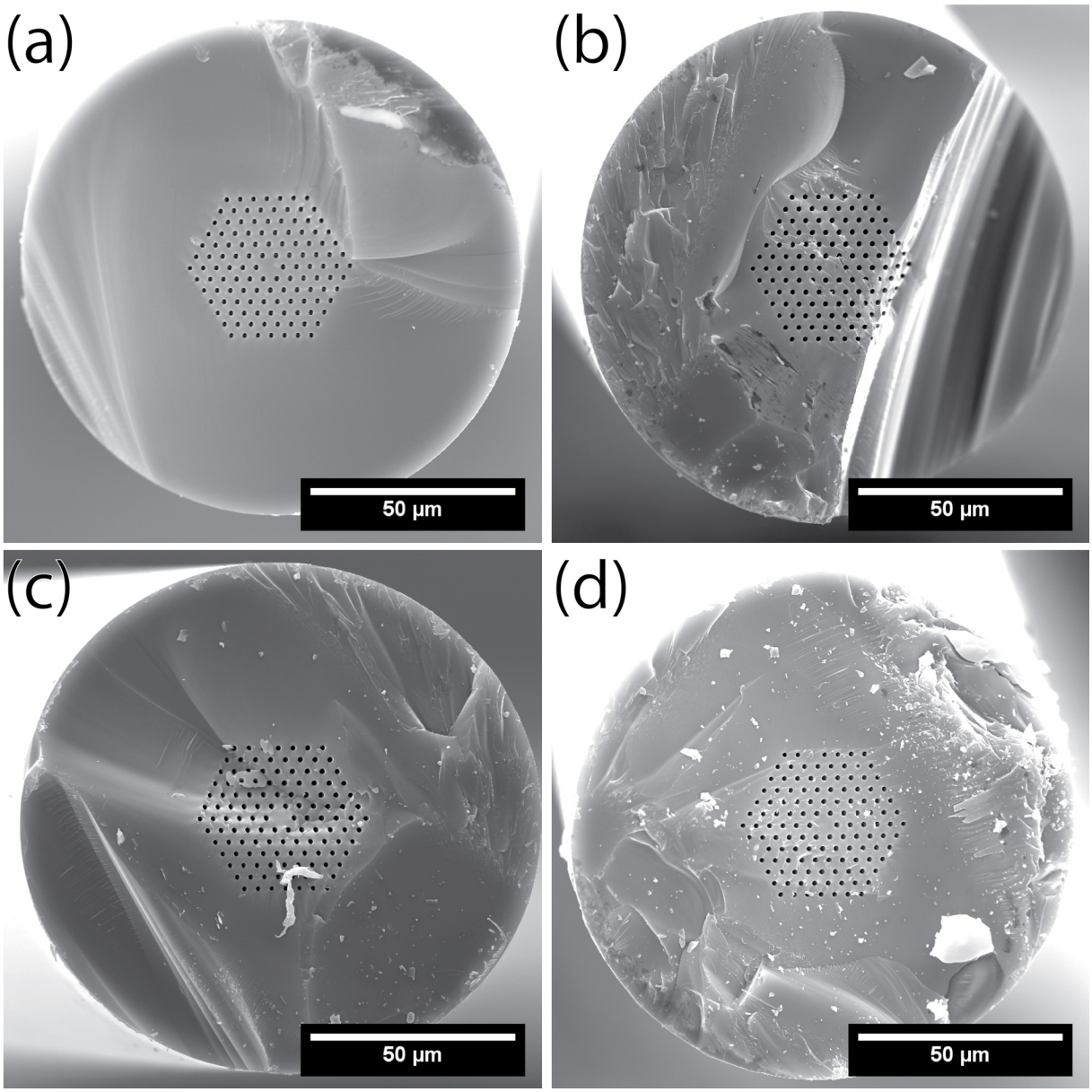

Figure 3.10: Examples of a cut LMA5 fibers that were not etched, only striped of their acrylate coating.

Properly cut LMA5 fiber is shown in the image 3.10 (a). In the bottom left corner of the image, there is a visible path which points to the place, where we cut the fiber. The upper right area shows a fairly amount of damage, however the rest of the fiber (and especially the microstructured region) is intact and smooth. The image 3.10 (b) shows, that we cut too deep and damaged the microstructured region. The image 3.10 (c) shows similar example as the image (a), however the surface is not that high-quality. The last image 3.10 (d) shows an example where the fiber was cut through completely, there is fairly amount of debris left on the surface of the cross section. Although the microstructured region is not damaged, the overall quality of the surface is low in comparison with the image (a).

Cutting the HC532 fibers is even more difficult than cutting the LMA5 fibers because the HC532 fibers have a microstructured region that is more sensitive to breaking. This is clear when inspecting images, that have been taken using Tescan Vega SEM, and are shown in the figure 3.11. The walls of the hexagonal holes, that make the microstructured region are much thinner than the ones in LMA5 fibers, hence they are more breakable. The left image in the figure 3.11 shows a lot of debris left on the cross section. Also, the core seems to be highly shattered. In comparison, in the image 3.11 there is almost no debris present and the core is of a higher quality. As these fibers are no longer available at the manufacturer, we decided that no further testing will be done using these fibers.

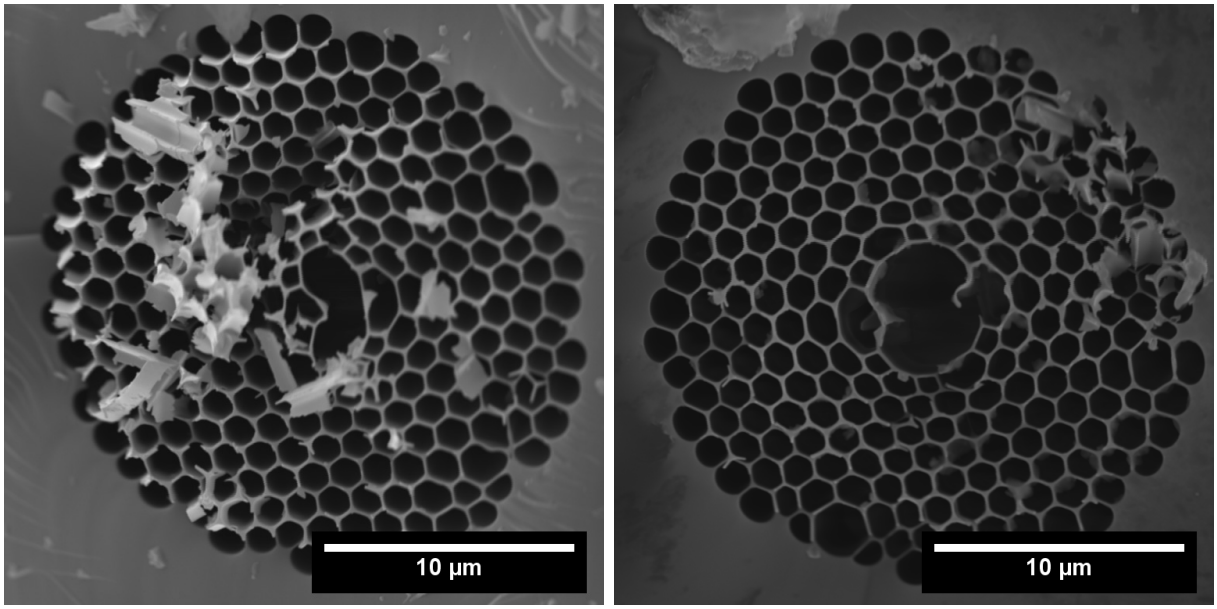

Figure 3.11: Examples of a cut HC532 fibers that were not etched, only striped of their acrylate coating.

Finally, the images showing a quality of the cut of the etched LMA5 fibers, are shown in the figure 3.12. These fibers were etched for a 35 minutes in a 40% HF acid using the second approach[2]. After the etching, they were cut in the middle of the stripped down acrylate coating. That means, that the etched tips were approx. 3 cm long. It is visible that the cut cross section of LMA5 fiber in the right image is charging, as it is no longer coated by Au after the cutting.

[2]Described on page 21.

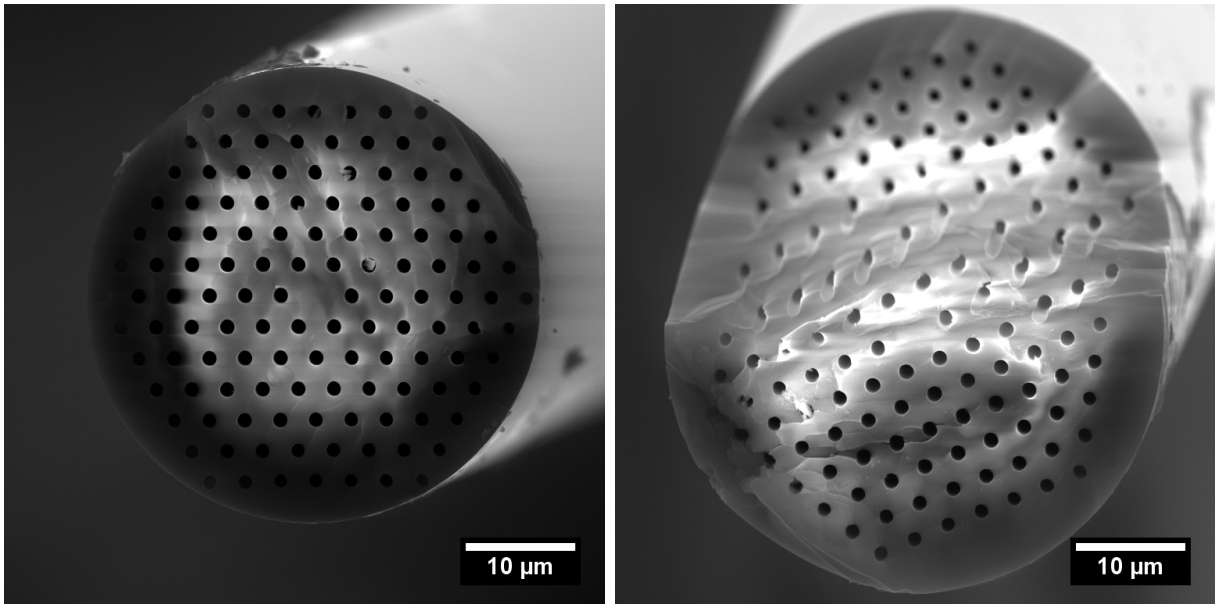

Figure 3.12: Cut and etched LMA5 fibers after 35 min etching in a 40% HF acid using the second approach. The two fibers in the figure are a different fibers.

After the etching and cutting is done, the fibers could be inspected in the optical microscope or could be coated with a thin metal layer using the Kaufman deposition chamber located in the laboratories of IPE (IBAD technique). The standard procedure of the thin metal coating is to coat the fiber first with a 3 nm Ti adhesion layer. Then the fibers are coated with a 200 nm layer of Au. It is important to mention that the thicknessmeter shows a value that is not correct as the fibers have different position relative to the target in comparison to the thicknessmeter. Also, as the fibers are being coated with the layer, they are being rotated in order to coat them uniformly. Expected thickness of the individual deposited layers is smaller than the value measured by the thicknessmeter. However, in most cases this does not play a major role in coating the PCFs, as the reason of the coating is reduced purely to having the fibers conductive for the SEM imaging (to have a right amount of the coated metal is more important in coating the conventional SNOM probes made from conventional optical fibers).

4. LBIS: Laser Beam Insertion System

In this chapter, we discuss an optical section of this diploma thesis. We introduce two major assemblies: one assembly to guide the laser beam into the PCF and the other assembly to investigate the light coming out of the PCF on the other side. We introduce a several test cases of various fibers.

4.1. LBIS assembly

In order to guide the laser beam into the PCF (or any other type of fiber) while keeping the PCF insulated inside of a vacuum chamber, glass viewport must be used. Laser beam insertion system (LBIS) is an optical assembly which allows us to guide the laser beam into the PCF (located in the vacuum chamber) through the viewport.

The LBIS was designed with a help of Ing. Zbyněk Dostál, Ph.D. The LBIS is designed in a way that it fits onto a gas injection system (GIS) which together form an united assembly with a codename of NanoGIS.

A rendered view of the LBIS is in the figure 4.1. Autodesk Inventor 2019 was used for assembling and rendering. The list of used components is included in the appendix. The assembly utilizes the standard ThorLabs's cage system.

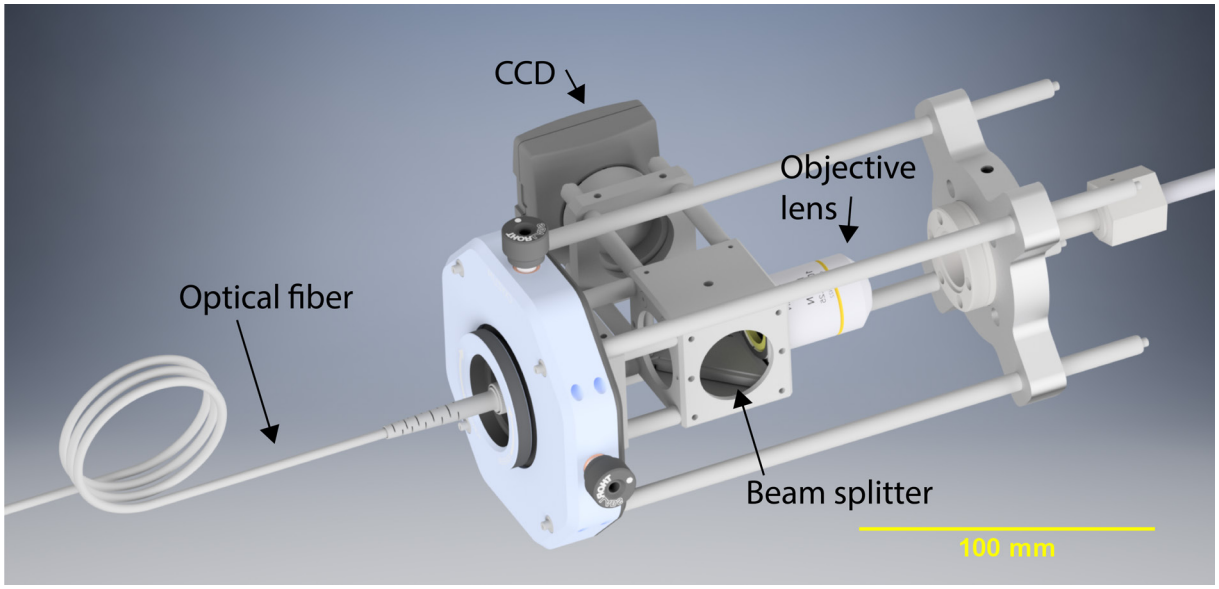

Figure 4.1: A rendered image of the laser beam injection system. The laser beam enters the LBIS via an optical fiber leading from a laser head platform (mentioned in the following text) attached onto a collimator (with PC/FC port) which is mounted onto the XYZ translation stage of the LBIS.

A laser beam optics is mounted onto a XYZ translation stage. The laser beam optics consists of a beam splitter, an objective lens, a tube lens and a CCD camera. The objective lens is used to focus the laser beam into the PCF located inside the vacuum chamber. The beam splitter is used for the CCD camera in order to have an image of the PCF. The

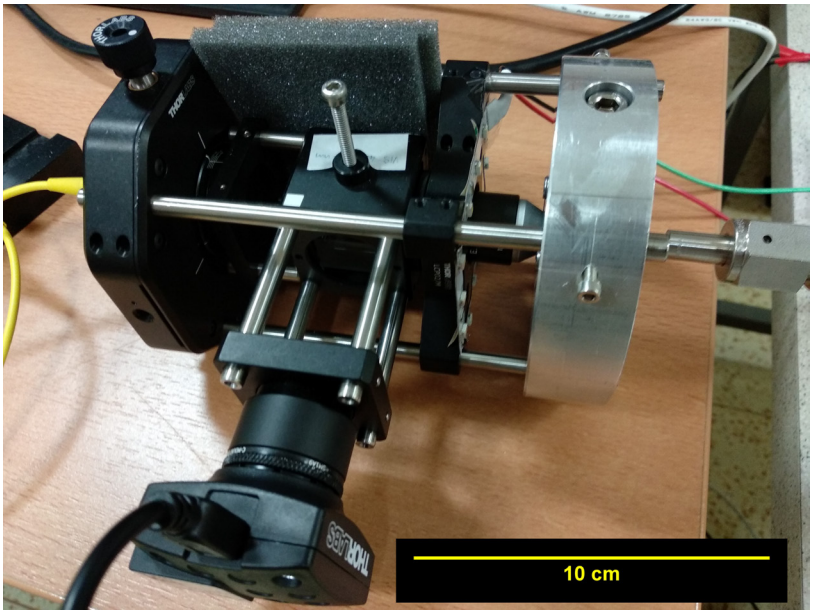

Figure 4.2: A photograph showing the laser beam insertion system. The optical fiber is yellow. The green and red fibers power the LED lighting.

LBIS is mounted onto the GIS utilizing ThorLabs's cage system rods at which an adapter is mounted. This adapter is used to mount the GIS.

Major task was to put the assembly together, as the laser beam is being focused only via the objective lens and the image sharpness formed on the CCD is dependent not only on the objective lens, but also on the tube lens. Our goal was to reach a state when one could claim that a sharp image of an object (in this case, the point of entry to the PCF) imaged in the CCD was corresponding to the laser beam being in the focus. A focused laser beam means simply that its beam spot has the smallest diameter possible. In order to reach this state of the mutual correspondence between sharp image and focused laser beam, we used a silicon wafer with a scratch marks on it. We were imaging the laser beam and the scratch marks illuminated with a LED lighting. By changing the relative distance between the tube lens and the objective lens, we could achieve a bright image of the scratch marks and an image of the laser beam with a spot size with the smallest diameter achievable, see figure 4.3.

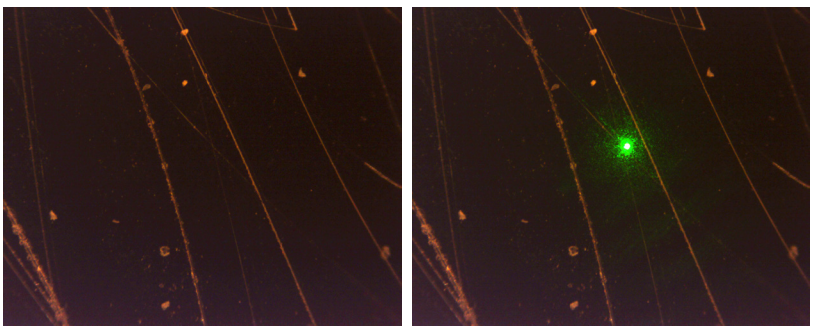

Figure 4.3: A testing image for correlating a sharp image with a focused laser beam. Scale bar is not included as there is no reference to the real dimensions. Brightness and contrast were altered to enhance the scratch marks.

After we successfully found the optimal position of the tube lens, tube lens is locked in this position. As the whole assembly is very sensitive to any kind of mechanical impulses, it is not easy to achieve this state. Another issue is that our assembly has relatively large depth of focus. There is approx. 1 mm of an uncertainty in the distance between the objective lens and the tube lens.

Major drawback of the current LBIS is quite high sensitivity to the mechanical interference. This issue could be addressed in the future work on this project by changing all manually controlled parts for motor controlled parts, making the whole assembly more robust and shorter in order to lower the moment of inertia. Another possibility is to make this assembly static and make a translation system for the PCF itself which is inserted inside the vacuum chamber.

A platform for mounting a various types of laser heads was developed. This platform is used to guide the laser beam directly from the laser head into the collimator (with PC/FC port) to which an optical fiber is attached. This optical fiber leads to the LBIS. The collimator is mounted onto a XY translation stage. A rendered view of the laser mounting platform is in the figure 4.4. Autodesk Inventor 2019 was used for assembling and rendering. The list of used components is included in the appendix.

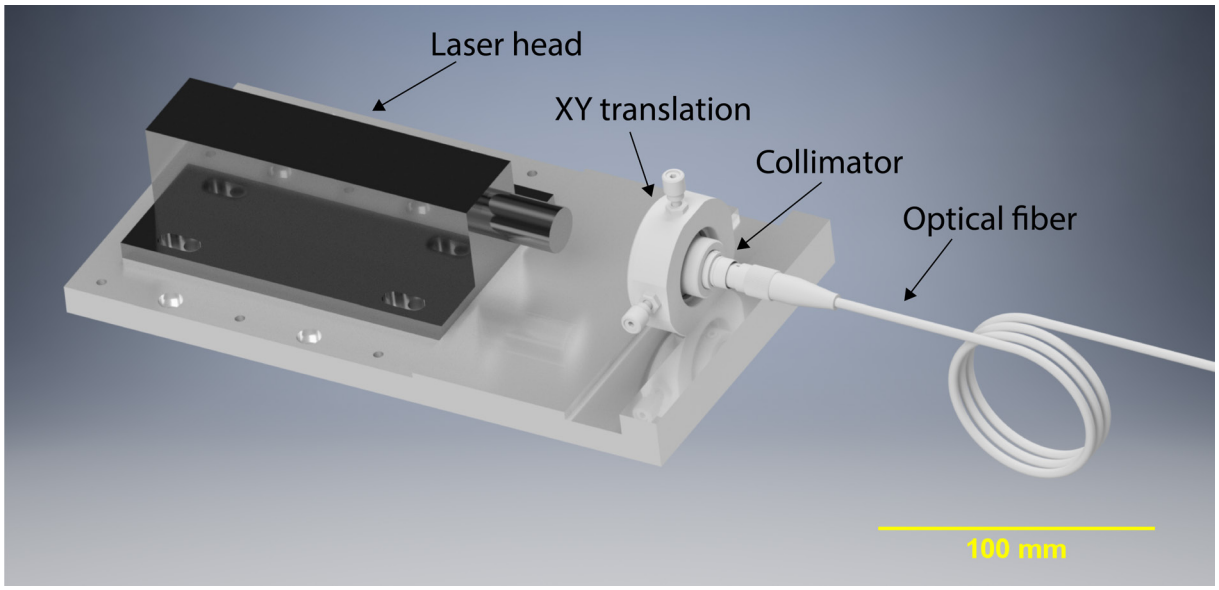

Figure 4.4: A rendered image of the laser mounting platform. The laser beam enters the optical fiber which is attached onto a collimator (PC/FC port) which is mounted onto the XY translation stage. The platform is designed in order to fit various types of laser heads. The optical fiber leads to the LBIS.

Currently, there are two laser sources available, however we are using a conventional laser head located in the left photograph in the figure 4.5. The laser, that we use in this diploma work, is a single longitudinal mode green laser working at 532 nm wavelength made by the company CNI [35]. This laser has a maximum optical output of 20 mW. Additionally, we have in our possession a diode pumped solid state laser made by ThorLabs [36] of a maximum optical output of 40 mW. As ThorLabs sells this diode separately, one must buy an actively controlled heat sink and a controller which can control both, the temperature and the optical output of the laser diode. As this items are not cheap, we decided, that we only use an aluminum heat sink as a passive temperature control and a lab bench power supply to drive the laser diode. As it is stated in the datasheet

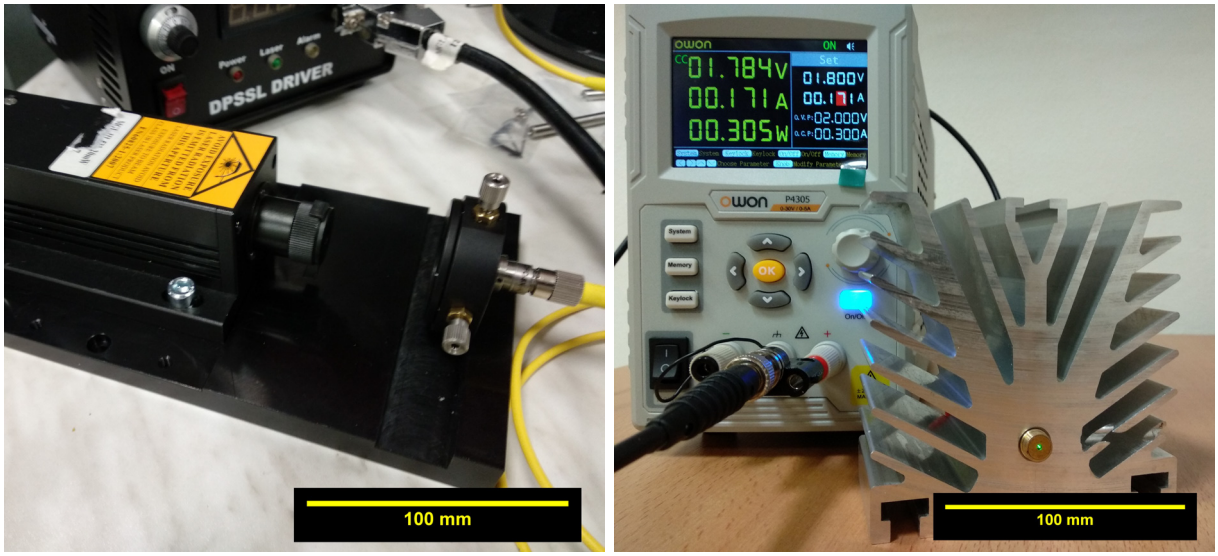

Figure 4.5: A photographs of the two currently available laser sources. A CNI laser head attached to he laser mounting platform is in the left photograph, the laser driving unit is visible in the background. A ThorLabs DPSS laser diode inserted into an aluminum heat sink is in the right photograph.

[36], an interval of the operating temperatures is from 25 °C to 30 °C. This requirement makes it basically impossible for the passive heat sink to be satisfactory. There are plans for the future to upgrade with a thermoelectric cooler (TEC) controller [37] available from ThorLabs and a Peltier module [38] capable of cooling the laser diode down. The TEC available at ThorLabs has an implemented software, so it is easily controlled by the user, however it requires a computer. A rendered image of a possible model of an implementation of the ThorLabs DPSS laser diode onto the XYZ platform of the LBIS is in the figure 4.6. Autodesk Inventor 2019 was used for rendering and assembly.

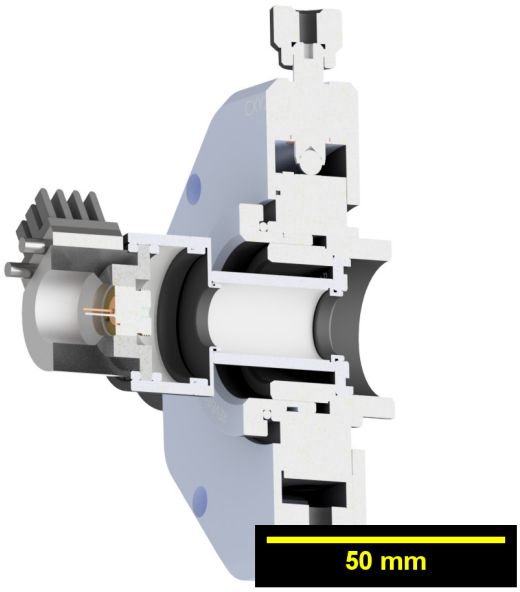

Figure 4.6: A rendered image of a possible model of the ThorLabs DPSS laser diode implemented in the LBIS directly.

The laser diode has also a protection against electrostatic discharge and a reverse voltage. This protection is made out of a parallel combination of a fast Schottky diode [39] used as a reverse voltage protection and a Zener diode [40] used as an electrostatic discharge protection. Simple schematic is shown in the figure 4.7. The laser diode is connected with the lab bench power supply [41] via the BNC cable of a length of 1 m in order to reduce the cable's parasitic capacitance. The motivation for using a laser diode on its own is that it can be mounted onto the XYZ translation platform of the LBIS and thus reduce a portion of the light intensity loss at the optical fiber connections. There is an assembly prepared for the laser diode, however it was not implemented yer as this was not a priority. This could be resolved in the future work on this project. The aluminum heat sink is compatible with the laser head platform. The laser diode was tested, it is fully functional, however, as we currently do not own the TEC controller, we are using the CNI laser.

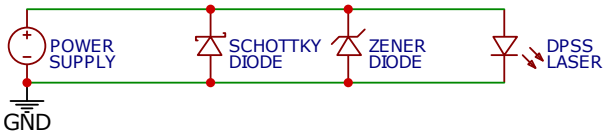

Figure 4.7: A schematic of the ThorLabs DPSS laser diode with a protection element consisting of a Schottky and a Zener diode.

4.2. Laser Beam Insertion System testing

For a testing purposes of the LBIS we used three types of fibers: SM600, LMA5 and HC532. These three types of fibers were discussed in the Photonic crystal fibers chapter on page 9. In the figure 4.8, there is a set of images captured by the CCD of the LBIS. Each column represents corresponding type of the fiber. From the left column to the right: SM600, LMA5 and HC532. In the first row, an image of the point of entry of the fiber is captured. In the second row, an image of the point of entry of the fiber with a laser on is captured. The scale bar in the bottom right image fits every image in this figure. The process of focusing the laser into the fiber is as follows. First, the fiber is put in the focus via the Z part of the XYZ translation stage. Then the laser beam is turned on and the XY part of the XYZ translation stage is used to direct the laser beam into the fiber. Finally, utilizing the optical microscope (discussed in the following text), the XY transition is carefully adjusted in order to get a maximum intensity of the light coming from the PCF in the optical microscope. As it was mentioned, low mechanical stability is complicating this process. Slight bump into the table could result in a loss of light.

Comparing the second row in the figure 4.8, first noticeable detail is in a different sharpness of the laser beam spot size for each individual fiber. We are not completely sure why it is that sometimes the laser beam spot is small and sharp and sometimes it is not. However, the laser beam spot looks almost always larger on the SM600 than on the rest of the fibers. This could be due to the fact, that the SM600 is a solid core conventional optical fiber and various physical phenomena taking place at the interface could contribute to the larger beam spot size. For comparison, additional image of the laser beam spot formed on the SM600 is displayed in the figure 4.9, with the same scale bar as in the previous figure. The quality of the laser beam spot is noticeably different.

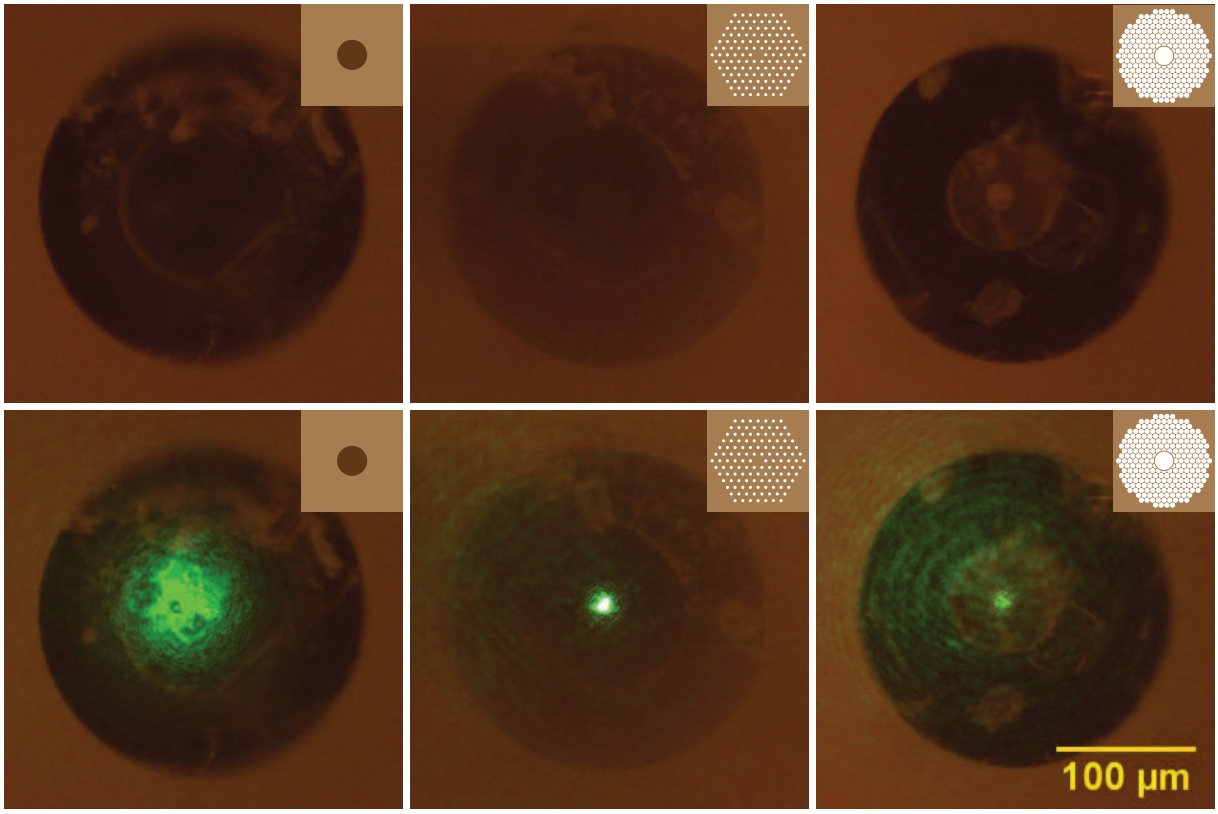

Figure 4.8: A testing images of the points of entry of various types of fibers captured by the LBIS CCD camera. From the left column to the right: SM600, LMA5 and HC532. Both rows of the images are taken with a LED lighting on. The images in the first row are taken with a laser off, and the images in the second row are taken with a laser on. This images correspond to the images which are used in the figure 4.12.

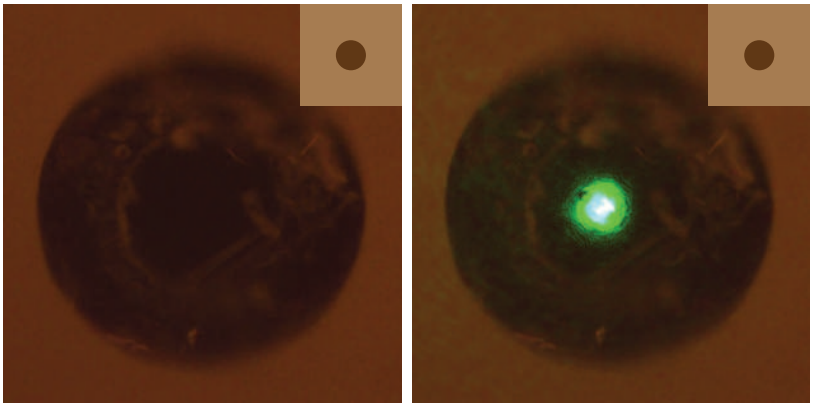

Figure 4.9: A laser beam spot formed on the points of entry of two different SM600 fibers. For comparing purposes of the laser beam spot size. Same scale bar as in the figure 4.8.

4.3. Optical microscope

4.3.1. Optical microscope assembly and testing

In order to investigate an optical output of the PCFs, we developed in collaboration with Ing. Zbyněk Dostál, Ph.D., an optical microscope. Our approach was to keep the optical

assembly as modular as possible for potential future upgrades and with enough degrees of motion for the sample to allow us a full view on the PCF's endpoint.

The microscope consists of two main parts: the optics body and a sample holder, both assembled on an optical table. The optics body is mounted onto a rotation platform to allow us to analyze the PCFs through various (azimuthal) angles. The optics body consists of three elements: objective lens, tube lens and monochromatic CCD camera. Between objective lens and tube lens, a beam splitter cube is inserted in order to keep the microscope modular for possible future applications. The objective lens are inserted into a micro translation stage for fine focusing. The sample holder consists of three linear translation platforms and one rotation platform. All together, with rotation of the microscope, we have 5 degrees of motion to investigate the PCFs. Via this microscope, one could investigate the dependence of the intensity of light coming from the endpoint of the PCF to the CCD on the azimuthal angle. Or utilizing the beam splitter, we could add another source of light and try to focus it via the optical microscope to the tip of the PCF and thus capture it.

The microscope assembly is realized utilizing ThorLabs's cage system and consists mainly of items which can be bought directly from ThorLabs. Only a few parts of the assembly were designed and manufactured in the workshops of the IPE. A rendered view on the microscope is in the figure 4.10. Autodesk Inventor 2019 was used for assembling and rendering. The list of used components is included in the appendix. The photograph of the microscope is in the figure 4.11.

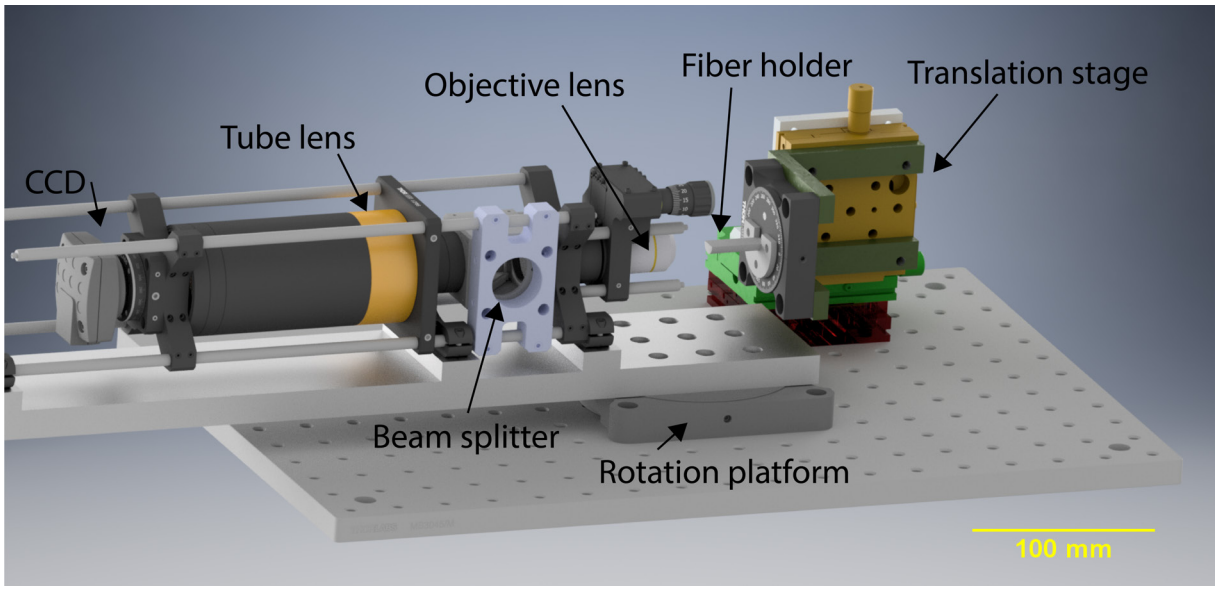

Figure 4.10: A rendered image of the optical microscope assembly. Optics body realized via ThorLabs's cage system is mounted onto a rotation platform. PCF is put onto a holder mounted onto a rotating platform which is mounted onto a 3 dimensional translation stage.

One of the main reasons to develop this microscope was to have an accessible and a fast way to investigate the PCF immediately after the first steps of the PCF's modifications (for example etching in the HF acid). Another major advantage is an option to have a look at the quality of the PCF's endpoint which is crucial. If the microstructured region is damaged, optical guiding properties of the PCF are attenuated. Damaged microstructured capillaries leads also to limited gas flow.

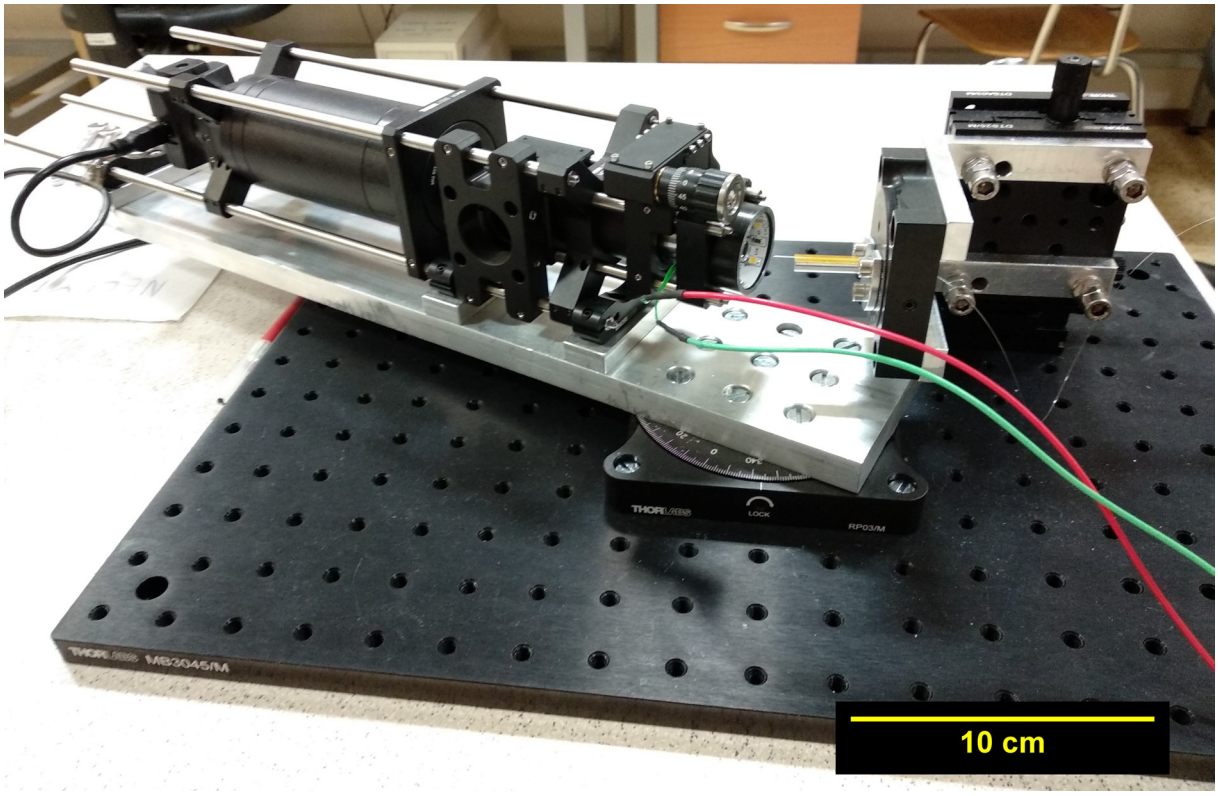

Figure 4.11: A photograph of the optical microscope assembly.

In the figure 4.12, there are three columns of images, each column containing 3 images captured by the CCD camera of the optical microscope. Each column represents different type of fiber. From the left column to the right: SM600, LMA5 and HC532. These fibers were not modified, they were only cut using the standard cleaver tool [34]. Scale bar is showed only in the bottom right image and fits every image in this figure. The first row represents the fiber's endpoint illuminated with a microscope LED lighting, the second row shows the same area, however with the laser on and the third row is as the second, but with the LED lighting off. To show details of the microstructured region of the SM600 and LMA5 fibers, brightness and contrast were changed in the images in the first two rows of the figure. Due to this change, there is a difference in intensity and shape of the beam profile between the second and the third row of the figure. However, brightness and contrast of the third row were not changed. The first column representing the SM600 fiber could be blurry, however was focused via the microscope in order to gain a sharpest image of the beam spot possible. It seems that this beam spot is doubled, it could be due to bad cut of the fiber. According to the data sheet of the LMA5 [21], the beam profile should have hexagonal profile, which to some extent is observable in the corresponding image. In the case of the LMA5, there is a square pattern of bright dots arranged around the beam spot visible. This will be addressed later in the text. Considering the somehow flawed beam spot of the HC532, this could be due to not properly cut the fiber's endpoint which is often an issue, at least for fibers containing any sort of the microstructured region.

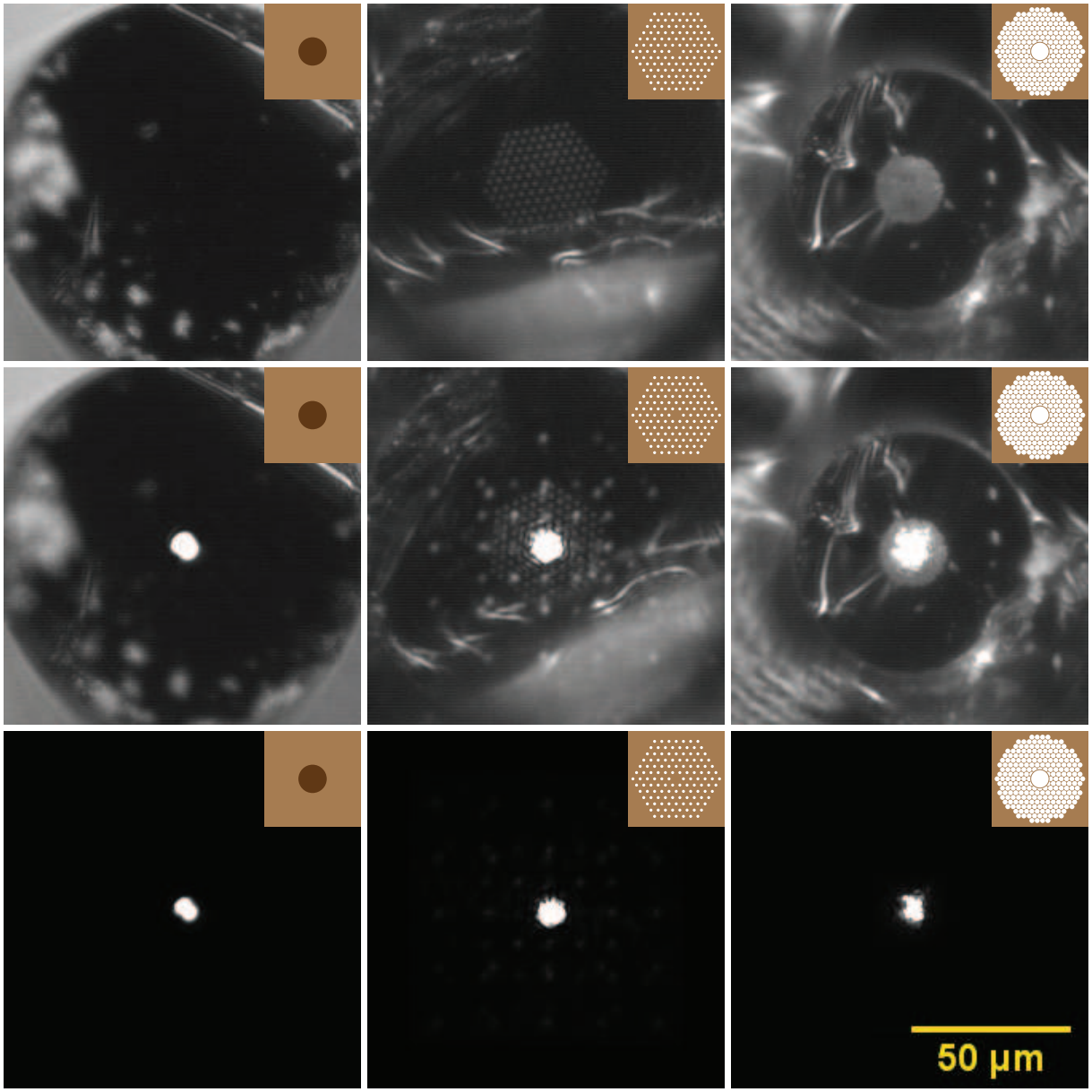

Figure 4.12: A testing images captured by the optical microscope of various types of the fiber's endpoints. From the left column to the right: SM600, LMA5 and HC532. From the first row to the third one: illuminated fiber's endpoint with laser off, illuminated fiber's endpoint with laser on, not illuminated fiber's endpoint with laser on. This images correspond to the images which are used in the figure 4.8.

4.3.2. Various test cases

Cutting of the fibers was discussed in the previous text. The quality of the cut usually improves the optical output of the fiber. In the figure 4.13 we could see, that the quality of the optical output was changed after we cut the fiber's endpoint of the LMA5 fiber. This fiber was etched in the HF acid to a diameter slightly above the diameter of the microstructured region. Although we do not have a direct comparison between an unetched LMA5 fiber and an etched LMA5 fiber (down to its microstructured region), we could estimate that the optical output stays high even for the etched fiber. The square-like diffraction pattern will be discussed at the end of this chapter.

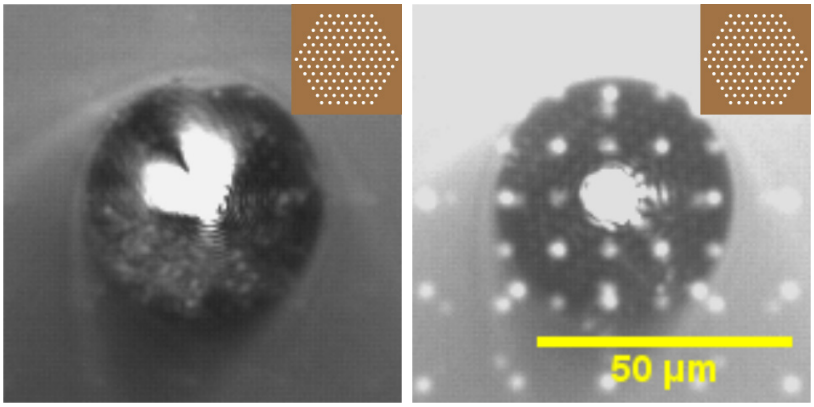

Figure 4.13: The impact of the quality of the fiber cut on the optical output of the LMA5 fiber. Brightness and contrast were changed in order to show the impact of the quality of the cut not only on the beam profile, but also on the microstructured region. In a case of a good cut, the microstructured region is not damaged and is visible. The diffraction pattern will be discussed further in the text.

Here are some of the examples of an interesting phenomena that occurred. For example, if we kept the shutter of the laser head just slightly open, we significantly reduced the laser beam spot size at the entry of the fiber. This lead to a lower intensity of the optical output of the LMA5 fiber. This is shown in the figure 4.14.

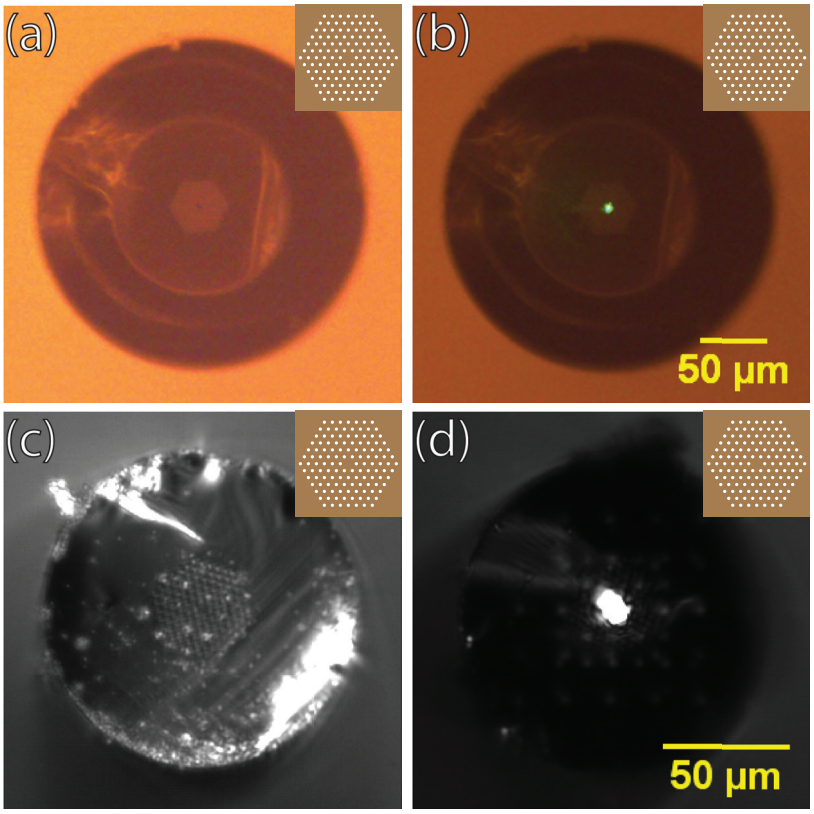

Figure 4.14: An experiment showing an optical output of the LMA5 fiber with a laser head shutter not fully opened. Brightness and contrast were altered in the left column. Hexagonal profile of the laser beam spot emerges.

In the figure 4.14, part (a) represents an overview of the LMA5 fiber's point of entry. In the part (b) of the figure, this point of entry is illuminated with a laser, the laser beam spot is smaller in comparison with a laser spot shown in the figure 4.12. Parts (c) and (d) correspond to the parts (a) and (b), respectively and show the fiber's endpoint on the other side of the fiber. Even with a laser head shutter not fully opened, we can observe optical output in the optical microscope.

Next, we look at the optical output of the LMA5 fiber that was covered with an Au layer in the Kaufman deposition chamber. Estimated thickness of the Au layer is 200 nm, however as this was discussed, the real thickness could be smaller. The electron microscope images are in the top row of the figure 4.15. This fiber was not etched in the HF acid, however the fiber's diameter was reduced via the focused ion beam (FIB) in the SEM Tescan Lyra3 in Ceitec VUT. The etching process via the FIB was time consuming due to the LMA5 fiber having a large cladding. That is the reason why we etched only a small length of the fiber. There is a curtain-like pattern in the top most-right image emerging at the bottom part of the image, this is a side effect after the FIB etching process.

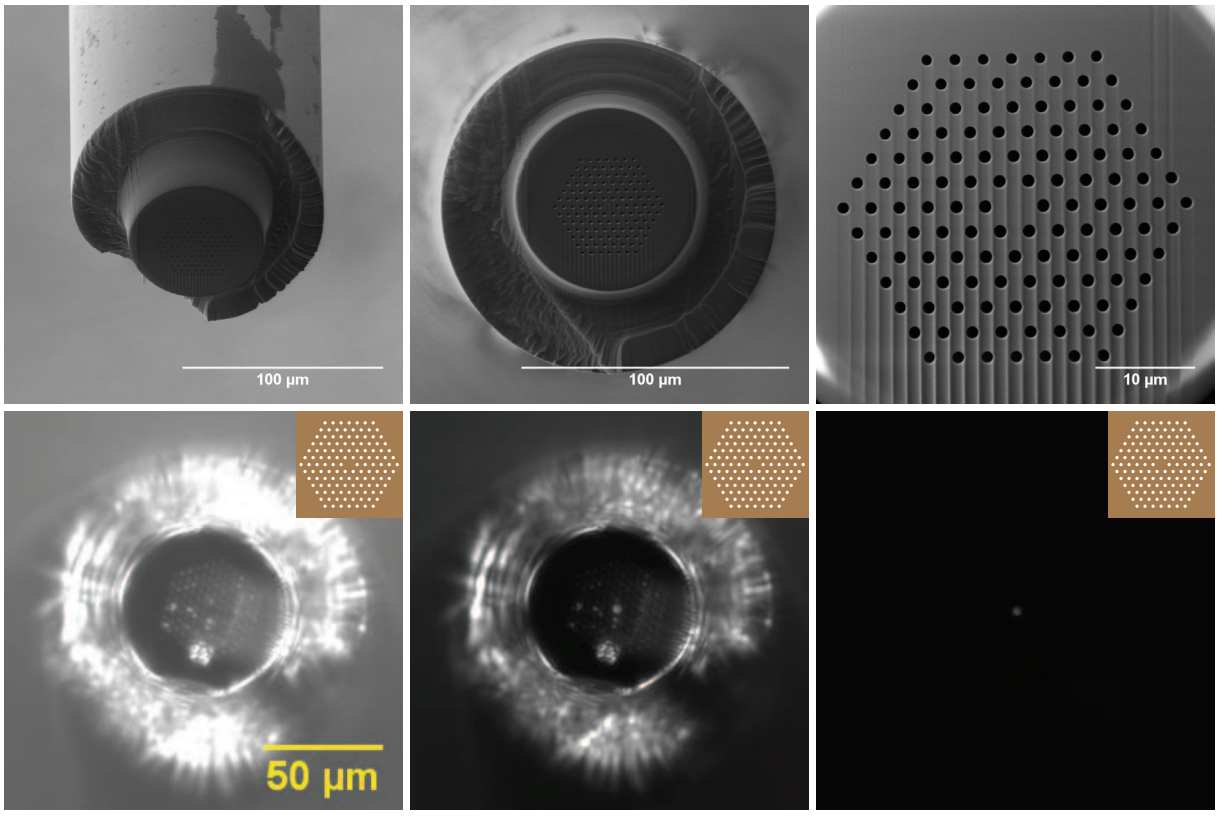

Figure 4.15: Top row represents an electron microscope images of the LMA5 fiber coated with a 200 nm of Au. Bottom left image brightness and contrast levels were modified in order to show the microstructured region, its scale bar applies to all images in the bottom row. Due to Au layer covering the core of the LMA5 fiber, less optical output is clearly visible. Laser power was set to 17 %.

Next, we look on the optical output of the LMA5 fiber which was covered with an Au layer, however at the center of the core we etched a circular shape to the Au layer by using the FIB. We made two versions: a version that has a circle with a diameter of 2 μm and the other version, that has a circle with a diameter of 6 μm. A 2 μm circle was made

in the LMA5 fiber that was mentioned previously in the figure 4.15. A 6 μm circle was made in the LMA5 fiber that was etched in the HF acid. A Tescan Lyra3 images are in the figure 4.16. In the images, the contrast between the etched circle and the Au layer is visible. The 2 μm version is in the top row and the 6 μm version is in the bottom row. The 6 μm version has a defect made during the FIB etching process. Above the 6 μm etched circle, there is an another etched circle, however it is not fully etched, so it is still covered with some amount of Au. It seems that this defect does not effect the optical output which is in the figure 4.17. The 6 μm version was etched in the HF acid, so its cladding is smaller.

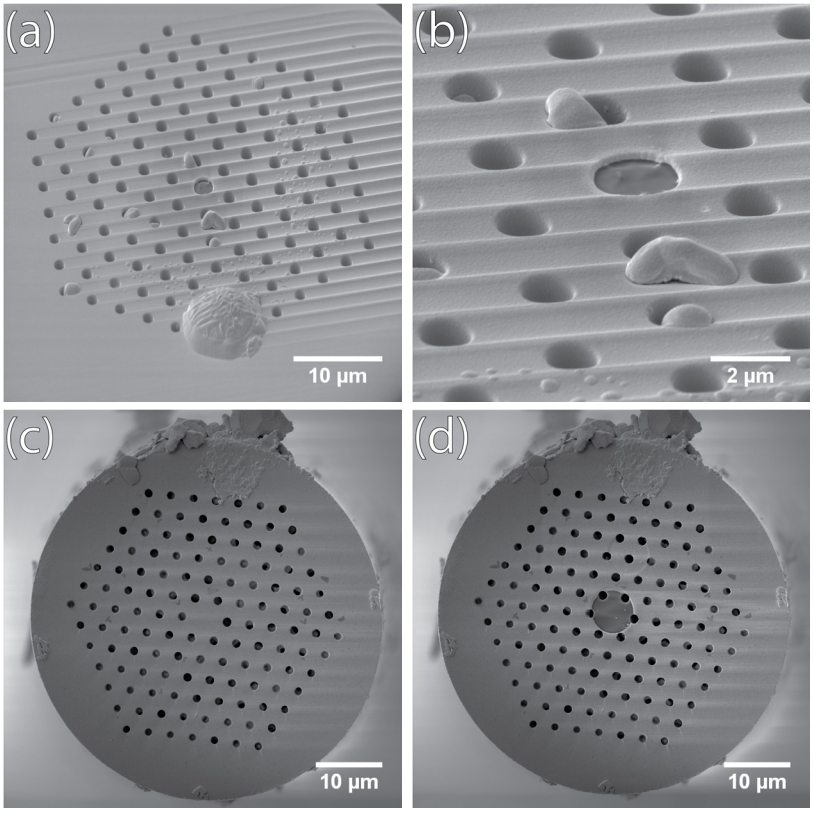

Figure 4.16: The first row shows a 2 μm circle etched in the Au layer, the second row shows a 6 μm circle etched in the Au layer. Both fibers are LMA5, top LMA5 fiber was not etched in the HF acid, bottom one was etched in the HF acid.

The optical output of such modified fibers is in the figure 4.17. The LMA5 fiber with a 2 μm etched circle is in the first row. In the second row is the LMA5 fiber with a 6 μm etched circle. Brightness and contrast were changed in the first and the second columns only. In the optical output of the 6 μm LMA5 fiber, besides the square-like diffraction pattern (which will be discussed) there seems a circular diffraction pattern, concentric with the etched circle to be emerging (most visible in the image (e)). These rings could be an Airy discs originating from the edge of the 6 μm circle, however these rings seems to be broken and not fully enclosing the etched circle. It seems that there is no significant difference in the optical outputs between the 2 μm and the 6 μm versions of the LMA5 fibers. This could be due to laser having too much optical power, thus the image could have been saturated. The laser power was set to 17 % which in this case seems to be too

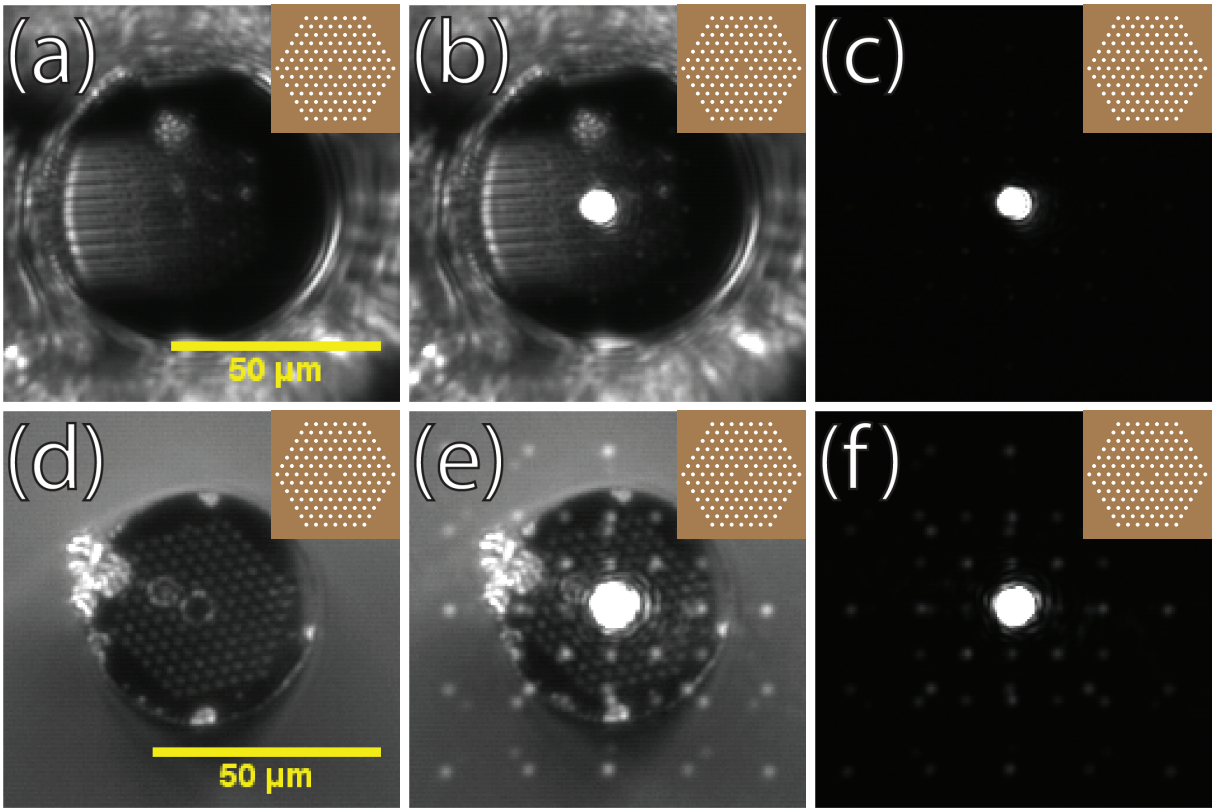

Figure 4.17: Optical output of the LMA5 fibers with a 2 μm hole (upper row) and a 6 μm hole (bottom row). The 6 μm hole is visible and a series of broken rings emerges. Laser power was set to 17 %.

high. We keep the laser power to this value to have a direct comparison between the two cases, one with a FIB non-etched layer and one with a FIB etched circle in the layer.

Next, we look at what happens when the laser beam spot is slightly off-axis relative to the core of the fiber. Naturally, the optical output intensity lowers. This was tested with the LMA5 fiber with a 6 μm circle etched by FIB in to it. The optical output is in the figure 4.18.

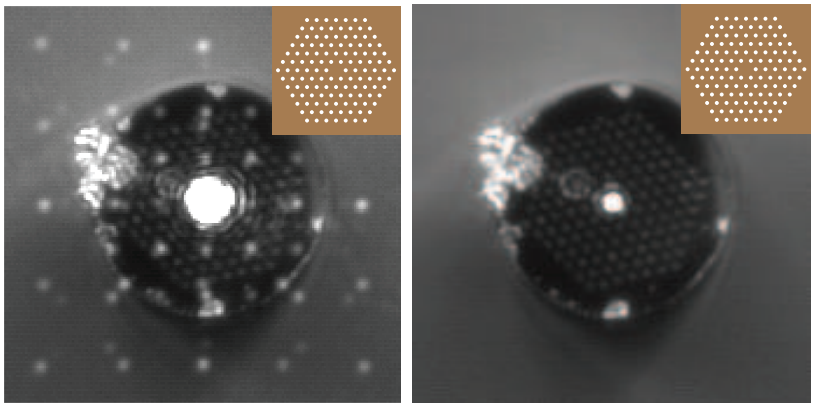

Figure 4.18: The left image is the same as the LMA5 fiber in the figure 4.17 (e), the same scale bar applies. In the right image, we put the laser beam spot slightly off-axis relative to the fiber's core. Laser power was set to 17 %.

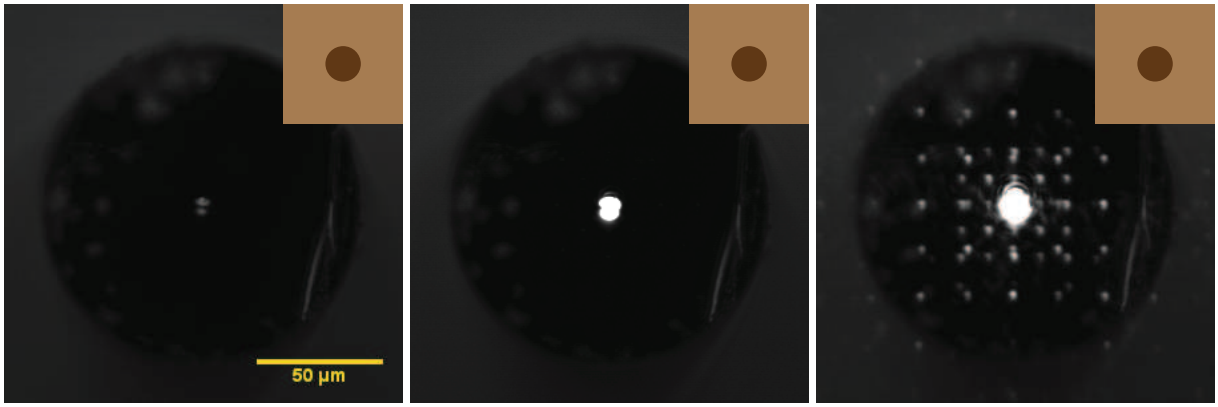

Figure 4.19: A conventional SM600 fiber used to show different levels of the optical output relative to the laser power. From the left image to the right, the laser power is increasing.

The left image is the same as the image (e) in the figure 4.17. The right image shows an optical output with a laser beam spot being slightly off-axis relative to the fiber's point of entry. Besides lower intensity, it seems that the optical output has a smaller area, however it remains its circular shape and it is located in the center of the fiber's solid core. The defect that was mentioned in the previous paragraph is clearly visible.

The effect of increasing the laser power on the optical output is shown in the figure 4.19. From the left to the right image, the intensity of the laser is increasing. The optical output keeps its qualitative characteristic, although its intensity naturally increases. The SM600 fiber was used. A diffraction pattern is present in all images. This could mean that the diffraction pattern does not originate in the PCFs.

We end this chapter with a discussion relative to the problem of the square-like diffraction pattern that is emerging in most of the figures containing images of the optical output of the fibers. As the pattern is square-like, there is a high probability, that the reason of the diffraction is the pixel array of the CCD camera. Nothing else in the optical microscope contains an element that could represent a grid with a square-like pattern, and thus be a source of the diffraction. When we rotated the fiber, the diffraction patterns have not been changed. This is the indication that the diffraction patterns do not originate from the fiber. When we rotated the camera (which is mounted onto a rotation platform), the diffraction patterns have not been changed. This is the indication that there might be a square-like grid pattern inherent to the camera itself. For final test, we interchanged the CCD cameras in the LBIS and the optical microscope. After interchanging the CCD cameras, we decided that it is best to set the LBIS with the scratched silica wafer again (correlating a focused laser beam with a sharp image formed at the CCD). We noticed that there is the same diffraction pattern emerging using the silica wafer sample. We concluded that the diffraction is inherent to the monochromatic CCD camera itself. Another interesting point is that there are more than one spatial frequency (probably two) occurring in the square-like diffraction pattern and that the intensity of the maxima (bright spots) is not constant. Presence of a two spatial frequencies could be due to the CCD camera having a protective layer. The diffraction pattern itself could be due to the CCD camera's pixel grid or some kind of a mask that the camera uses. We decided that we use the monochromatic CCD camera in the LBIS and the color CCD camera in the optical microscope. So, with the new setup, the optical output could look like this one shown in the figure 4.20. In the figure, the points of entry of the LMA5 fiber are captured in the

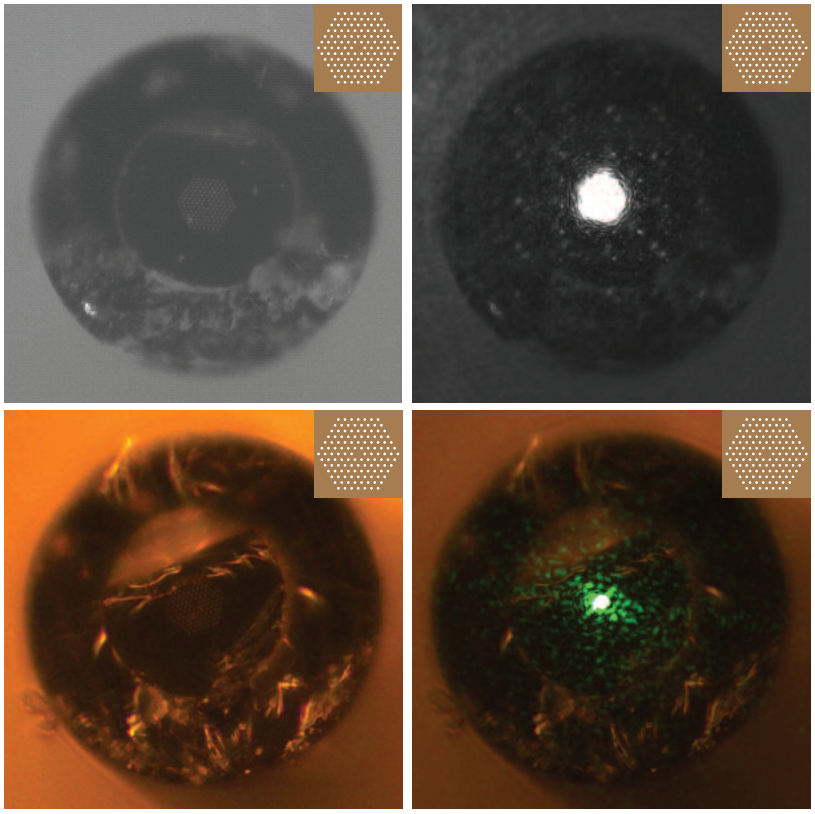

Figure 4.20: Top row images are from the LBIS (now monochromatic) and show the points of entry. The square-like diffraction pattern is visible. Bottom row images are from the optical microscope (now color) and show the endpoints. Brightness and contrast was altered in the left column of images.

top row of the images. The endpoints of the LMA5 fiber are captured in the images in the bottom row of the figure. However, as this was done in the late period of the work, all images remain in the old setup.

We also measured the dependence of the bending loss of the LMA5 fiber. With a radii of the bending up to 5 mm we did not measure any loss of optical output. With more bending, the optical output decreased, however bending the LMA5 fibers this much could lead to breakage of the fiber.

5. Integrating a SNOM probe on a solid-core PCF (LMA5 fiber)

In this chapter we summarize our efforts to modify a tip of the SM600 fiber by attaching a conventional SNOM probe tip onto the solid-core of the LMA5 fiber. This process is done using a SEM Tescan Lyra3 with a guidance of Ing. Mgr. Tomáš Šamořil, Ph.D.

First, the LMA5 fibers are etched with the 40% HF acid to obtain a proper diameter (approx. 45 μm), and the fibers are coated with an Au layer. Then we prepare conventional SNOM probes made of conventional optical fibers (SM600) using the Turner HF acid etching method [3]. Additional resources on how to etch conventional SNOM probes were acquired from dissertation thesis written by Ing. Petr Dvořák, Ph.D. [42]. These SNOM probes are then overlaid with a 3 nm Ti adhesion layer and 200 nm Au layer using the Kaufman deposition chamber located in the laboratories of IPE. As it was discussed in the last paragraph of the chapter concerning the HF acid etching, the actual thickness of the etched fibers is approximately (70 $\pm$10) nm. However, the actual thickness could still vary with different fibers, because they can have different lengths and shapes. To see the actual thickness, we cut the etched SNOM probes using the FIB, images are shown in the figure 5.1. As we are not very skillful with making the SNOM tips using the Turner method, the quality of the resulting SNOM tips differ and in result, they are too thin, as we were etching them for too long (75 min). Also, cutting of the SNOM tips is required for making an aperture from which the light can escape.

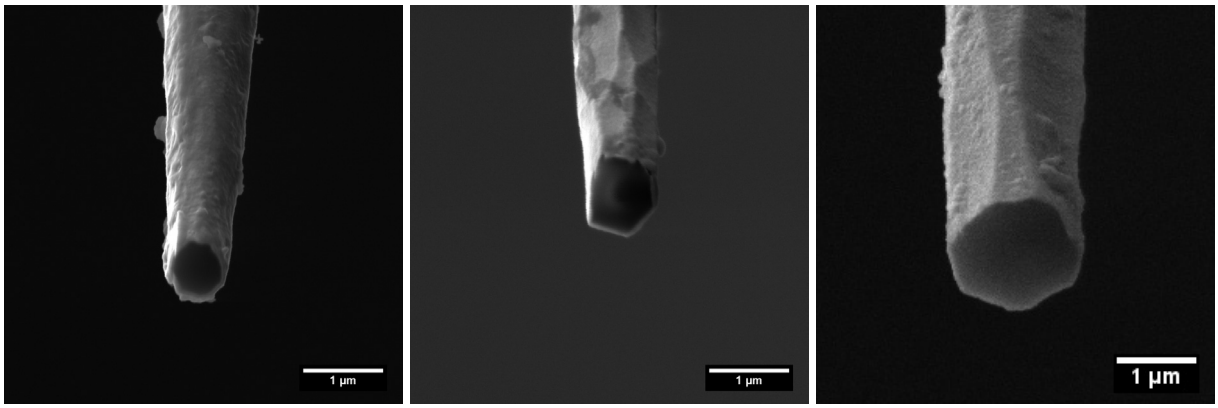

Figure 5.1: Thickness of the Au layer of a three different SNOM tips shown in their cross section made by cutting them by using the FIB. The quality of the tips differ.

After the SNOM probes are made, we proceed to attaching them onto the LMA5 fibers. First the SNOM probes are checked if they are not damaged (broken tip is frequent) and the endpoint of the LMA5 fiber is checked for damage, dust particles or any other inequalities. In the figure 5.2 which consists of several images, we are presenting a guide on how the SNOM probes are being cut in Tescan Lyra3 microscope using GIS [43] and nanomanipulator [44]. In the first step (a) and (b), an aperture is made into the tip of the SNOM probe. Next, the nanomanipulator is put in a close proximity of the SNOM probe (c) in a way that a small gap remains between the SNOM probe and nanomanipulator. This is due to later step which involves cutting of the attached SNOM probe off the nanomanipulator. The connecting bridge is made by using the FIBID technique with a Pt precursor (d). After the bridge is made, the SNOM probe is cut from the rest of

the fiber (e) and (f). This images are from the first session of total four, and it was not successful as the SNOM probe fell from the nanomanipulator due to a collision with the LMA5 fiber. It is necessary to mention, that the nanomanipulator sometimes made small sudden jumps, this complicated the whole process and can be partially avoided by not moving the nanomanipulator, but moving with the fiber instead, whenever it is possible.

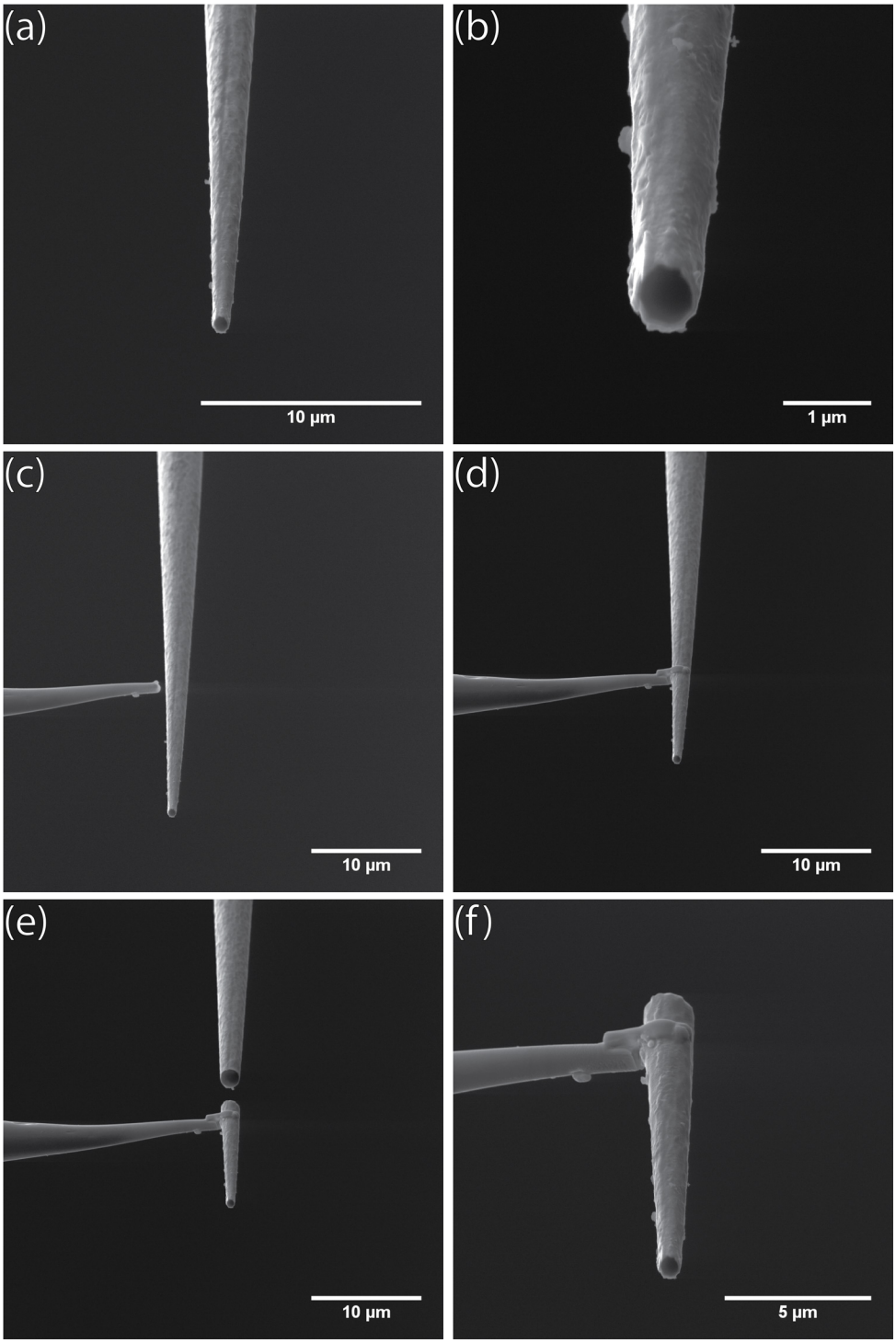

Figure 5.2: Experiment No. 1. An image guide showing steps in the process of attaching a SNOM probe onto a nanomanipulator.

In the second session, we decided to use an adhesive which hardens under an electron beam irradiation, SemGlu [45]. Using the nanomanipulator, a small droplet of SemGlu is put onto the LMA5 fiber's solid core. Then the SNOM probe is caught onto the nanomanipulator by utilizing the FIBID technique as it was described in the previous paragraph. Cut SNOM probe is put into the droplet of the SemGlu and hardened with an electron beam of high voltage (30 kV) and with high amount of beam current. Finally, glued SNOM probe is released from the nanomanipulator by cutting the Pt connection bridge with the FIB. SEM images showing the process of attaching the SNOM probe onto the LMA5 fiber are shown in the figure 5.3. In the (a) and (b) images, the SNOM probe is put into the droplet of SemGlu and hardened with the electron beam. The image (a) is taken by the FIB.

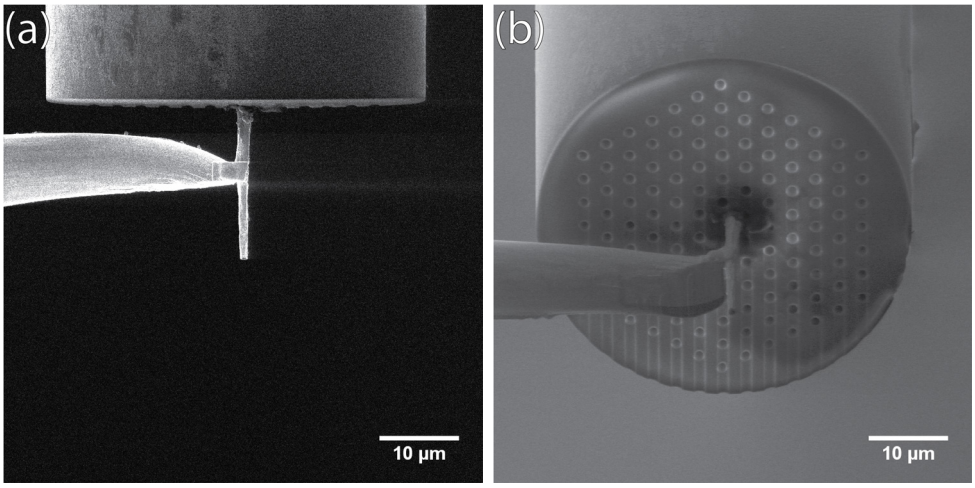

Figure 5.3: Experiment No. 2. Attachment of a SNOM probe onto the LMA5 fiber's solid core using SemGlu.

SEM images showing the results from different angles are shown in the the figure 5.4. In the images (a) and (b) a SemGlu clump is formed besides the SNOM probe. In addition, during putting the SemGlu onto the LMA5 fiber, the SemGlu is spread across the surface of the microstructured region which could lead to its sealing. This could be resolved by additional etching by the FIB. In the image (d) it is visible that the SNOM probe is placed slightly off-axis the LMA5 fiber. The image (c) is captured with the FIB.

We examined an optical output of the modified LMA5 fiber in the optical microscope. The images taken can not confirm that the light is coupled from the LMA5 fiber to the SNOM probe. The images are shown in the figure 5.5 and are showing the fiber under the approx. 30° angle. In the most left image, the microstructured region and SNOM probe are visible. The middle image shows the same region with a laser on a set to a power of 10 % (2 mW). In the last image, the power is set to 30 % (6 mW). When comparing the first and third image, we can notice, that there are bright spots in the SNOM probe region, however it is not sufficient. The reason could be that the SNOM probe is slightly off-axis, so the light coupling could be weak. There is also a strong source of light coming from the solid core of the LMA5 fiber which could dominate the weak source of light of the SNOM probe. After we captured the optical output, we proceeded to attaching of the fiber onto a tuning fork for the AFM. However, during the manipulation with the fiber, the SNOM probe fell down.

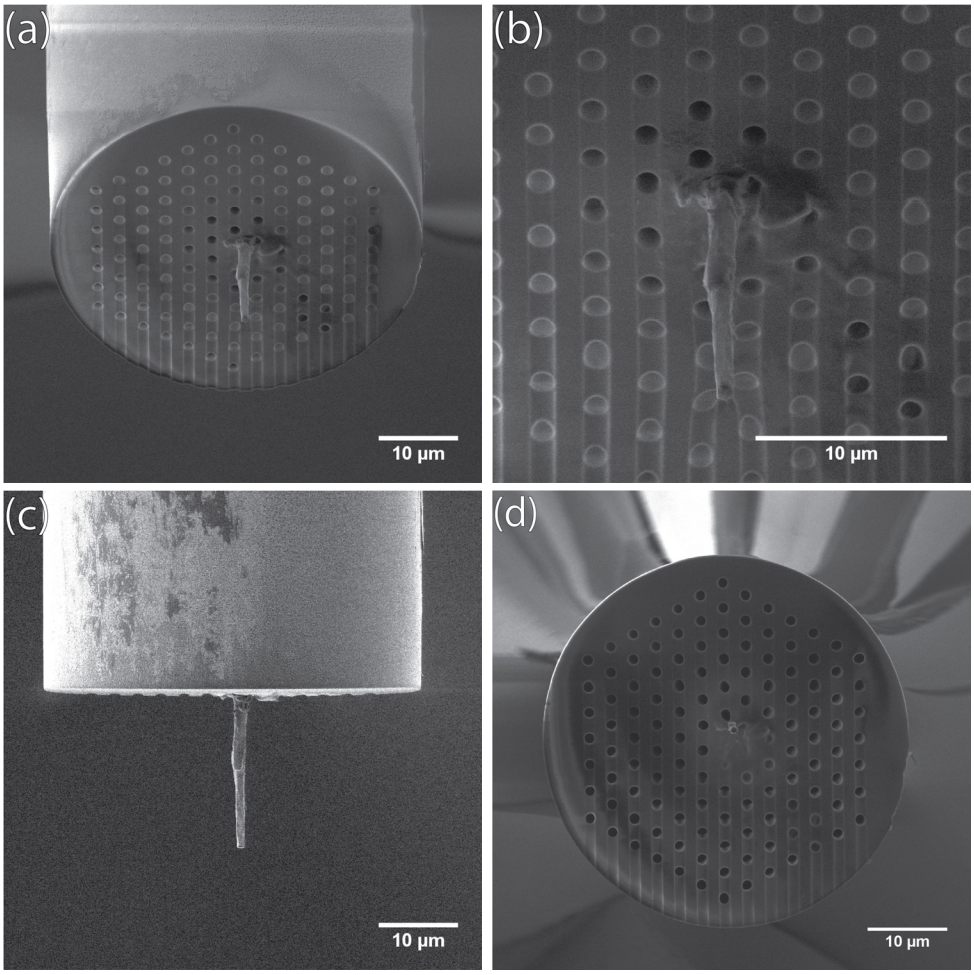

Figure 5.4: Experiment No. 2. Successful attachment of a SNOM probe onto the LMA5 fiber's solid core using SemGlu.

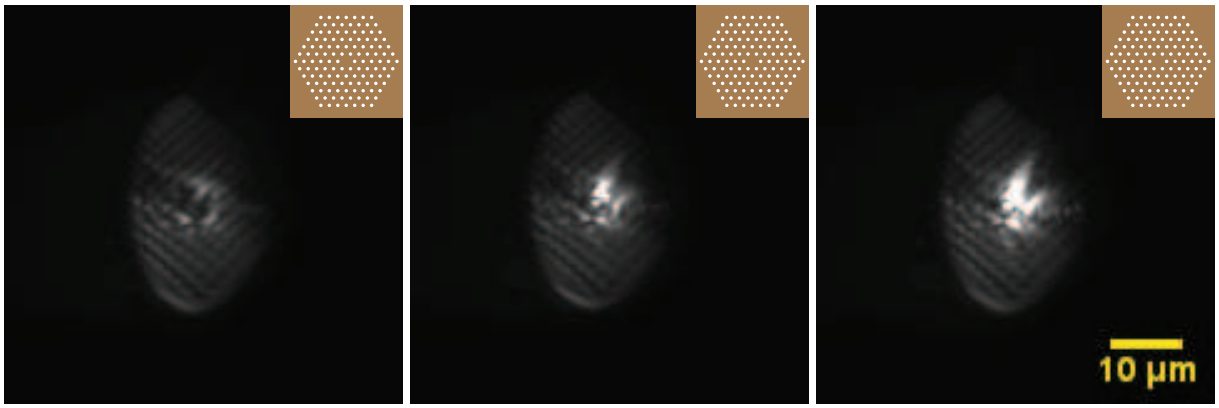

Figure 5.5: An optical microscope images of the LMA5 fiber modified with the SNOM probe taken under the 30° angle. From the left image to the right: laser off, laser on 10%, laser on 30%.

In the third session, we decided that at first we try to attach the SNOM probe onto the nanomanipulator by using the SemGlu, instead of the Pt precursor FIBID technique. The LMA5 fiber that we used was coated with Au layer and a 6 μm circle was etched by FIB onto its solid core (it is the same fiber as in the figure 4.16 (d)). The LMA5

fiber is shown in the figure 5.6 (a) and by comparing with the figure 4.16 (d), it seems that the edges of the etched circle appear to be slightly damaged, as if the Au layer in proximity of the etched circle, would want to exfoliate from the surface. A time interval between those two images is approx. one week. The SNOM probe attached onto the nanomanipulator using the SemGlu is in the figure 5.6 (b). This approach proved to be not successful. The SNOM probe fell down when attaching it to he LMA5 fiber, this could be due to the SemGlu being not hardened enough. However, the major issue consisted in the SemGlu spreading on the SNOM probe, thus covering the probe in the adhesive by a large amount. We decided that we use the FIBID technique to attach the SNOM probe onto the nanomanipulator.

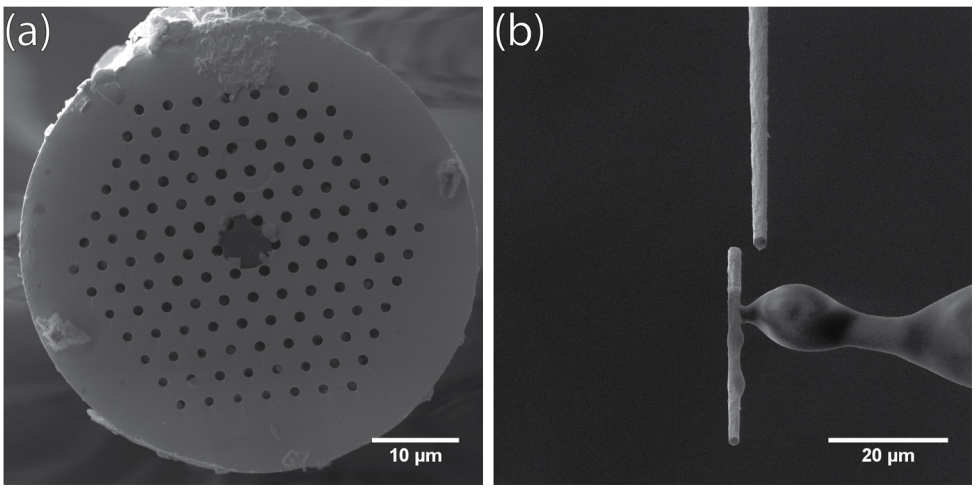

Figure 5.6: Experiment No. 3. A SNOM probe attached onto a nanomanipulator by the SemGlu.

The results of the third session are shown in the figure 5.7. In the image (a), the SNOM probe is being put into the SemGlu, that was previously applied to the etched circle in the LMA5 fiber's core. The images (b) and (c) show the resulting probe from different angles. In the image (c), it is visible that there is a Pt covering the rest of the etched circle. Due to shadowing of the SNOM probe, the gas containing a Pt precursor was not able to reach one part of the etched circle, thus remains uncovered. However, the area with the Pt layer blocks the light coming out of the solid core of the LMA5 fiber. At the tip if the SNOM probe, shown in the image (d), we noticed that there is a thin pin-like shaped body that could serve as an AFM tip. It is worth to mention that the SemGlu after hardening is stronger than the Pt layer deposited by the FIB. Although, the stability of the SemGlu remains questionable, e.i. we are not sure how it behaves outside the vacuum chamber of the SEM.

The optical output is shown in the figure 5.8. In the images (a) and (b), the fiber is captured from the front, with a laser on and with a laser off, respectively. There are a ring-like patterns emerging, and with a bright circle inside. This bright circle, it seems, have a smaller diameter than the etched circle.

Then we captured the fiber under the angle of 30° and it confirms that the light is coupled from the LMA5 fiber to the SNOM probe. The images are shown in the figure 5.9. The power of the laser was set to 50 % (10 mW). In the image (a), the tip of the SNOM probe is in focus. The image (b) captures the same situation with a LED lighting

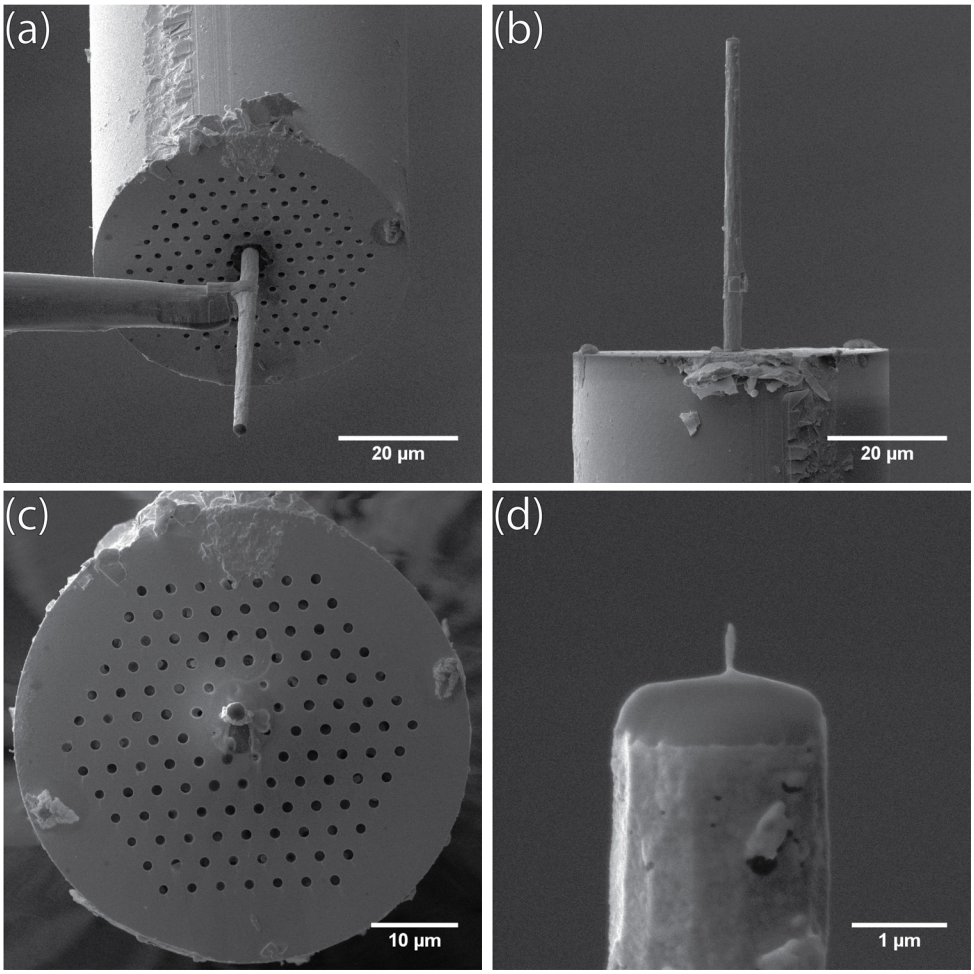

Figure 5.7: Experiment No. 3. SNOM probe attached onto an etched circle of the LMA5 fiber's solid core. The rest of the etched circle is partially covered with a Pt layer.

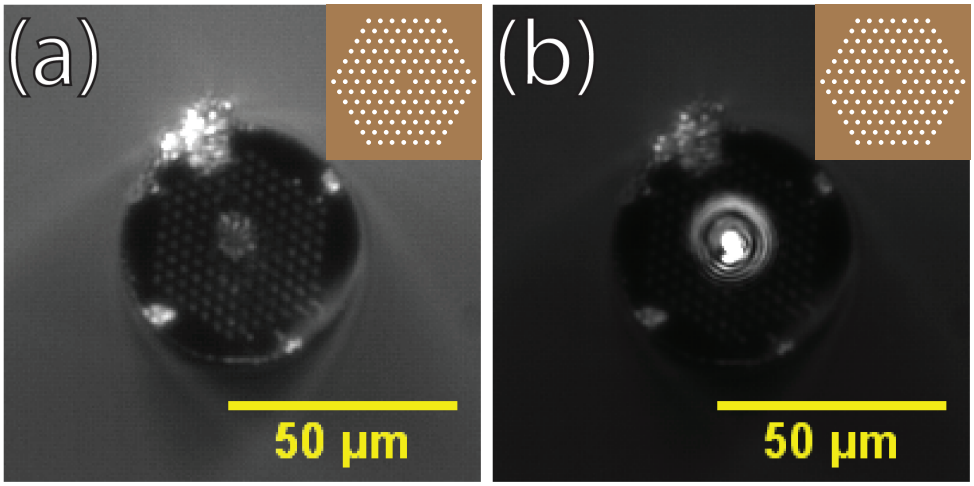

Figure 5.8: The optical output of the LMA5 fiber prepared in the third session. Captured the front of the fiber.

off. The image (c) shows a source of light emerging in the part of the etched circle, that was not covered with the Pt layer. The image (d) shows the same situation with the LED

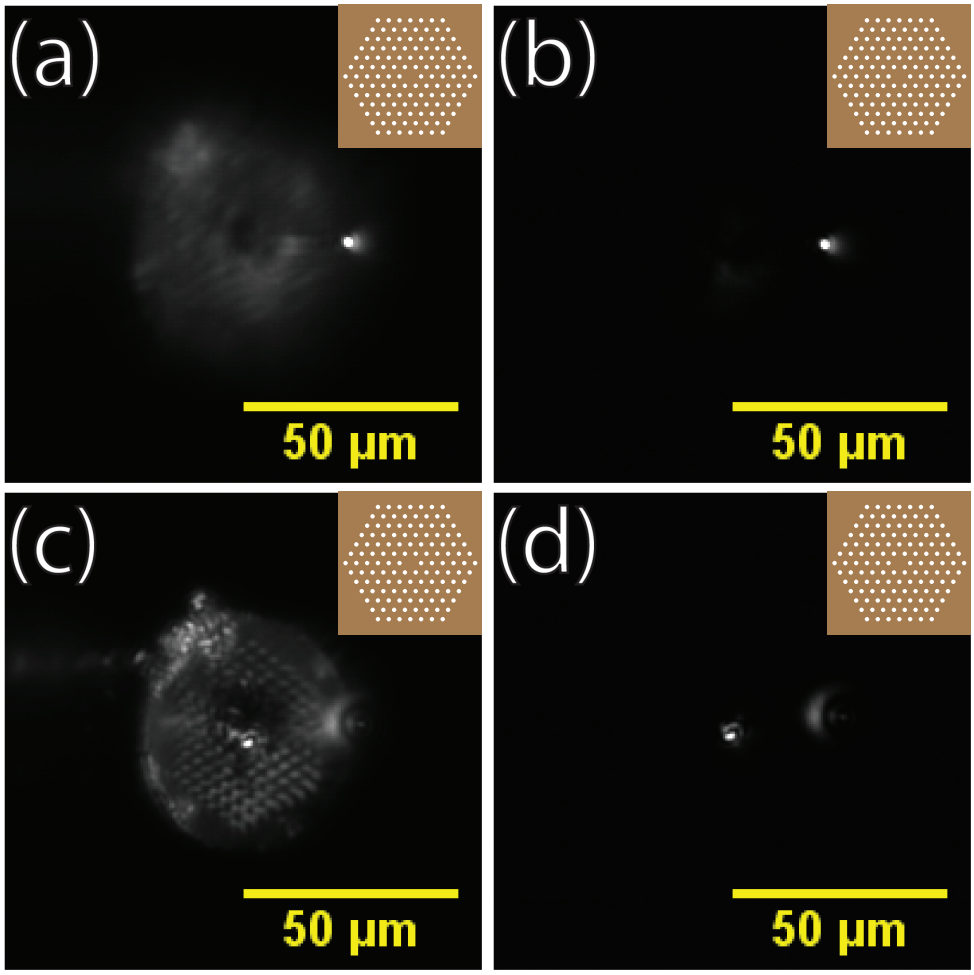

Figure 5.9: The optical output of the LMA5 fiber prepared in the third session. Captured under the 30° angle.

lighting off. Unfocused tip of the SNOM probe is visible. When the coupling of the light was confirmed, we proceeded to attaching of the fiber onto a tuning fork for the AFM.

In the last (4) session we tried to repeat the results from the previous session. The LMA5 fiber that we used had a 2 μm etched circle in the core. We aimed for attaching a SNOM probe in a way, that the probe covers the whole etched circle. Additionally, we decided that we make a smaller aperture to the SNOM probe. The somehow larger apertures used in previous sessions was due to having a direct confirmation of the light coupling, because smaller apertures could not be visible in the far-field in the optical microscope. The resulting images are shown in the figure 5.10. The image (a) shows a cross section of the LMA5 fiber with the 2 μm etched circle. It is the same fiber as in the figure 4.16 (a) and (b). The attached SNOM probe is shown in the image (b), the probe nicely covers the 2 μm etched circle. Even, the adhesive did not spread too much on the microstructured region. The aperture of the tip of the SNOM probe is shown in the image (c). Unluckily, during the manipulation, the probe fell off the fiber. And as we did not have good SNOM probes at the moment, we did not have a replacement and the session was over.

To conclude this chapter, it was shown that there is a coupling from the LMA5 fiber's solid core into the SNOM probe made out from a conventional optical fiber (SM600).

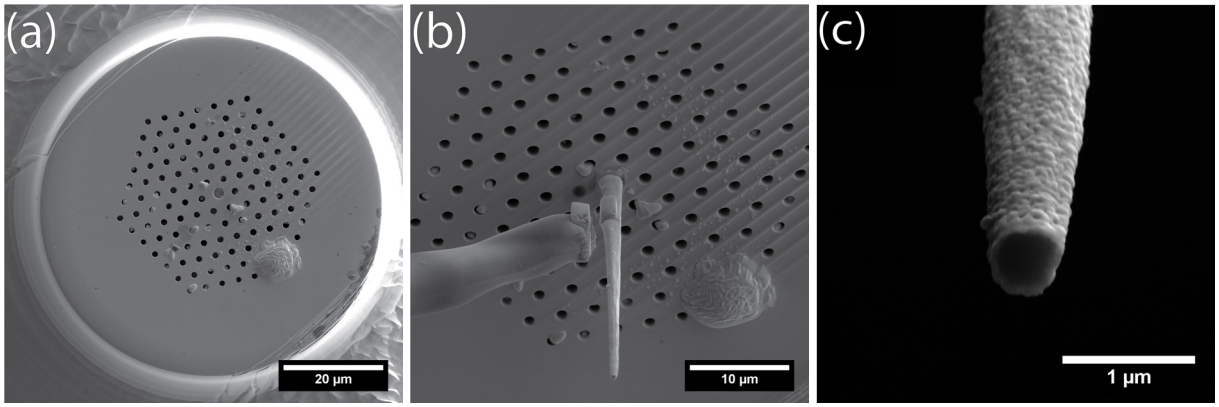

Figure 5.10: Experiment No. 4. The SNOM probe covers the 2 μm etched circle and has an 500 nm aperture.

Even though, there is an adhesive located between the LMA5 and SM600 fibers. In the future, hopefully, we will be able to attach a SNOM probe that has a small aperture, as it could be more interesting to perform a SNOM measurement with it.

6. AFM integration into SEM

In this chapter we document the process of integration of the atomic force microscope developed in the laboratories of the IPE, into the electron microscope Tescan Vega.

6.1. NanoGIS

In this section we briefly describe two assemblies. First, a special door compatible with the Tescan Vega microscope, that is used as a platform for mounting the AFM. This door have a series of KF ports, that are necessary for the AFM electronics connections, and for connecting the NanoGIS. The door was developed by Ondrej Černek in his bachelor thesis [46]. The door enables a movement of the mounting platform only in one direction, however the door is designed in a way, that the sample inserted into the AFM can approach the SEM objective. A rendered image of the door is in the figure 6.1.

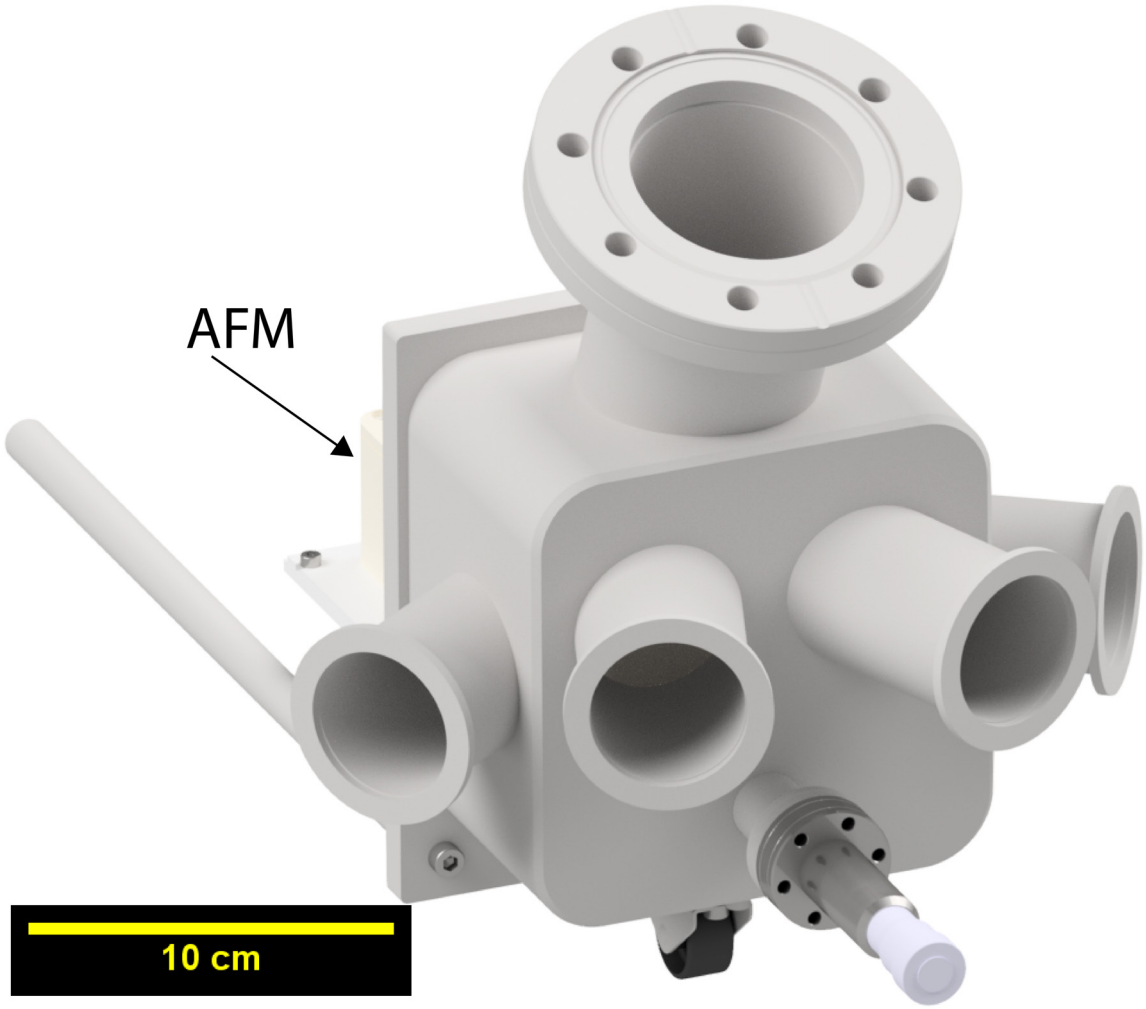

Figure 6.1: A rendered image of the Tescan Vega door assembly used for mounting the AFM.

The second assembly presented in this section is the NanoGIS. The NanoGIS was developed in collaboration with Ondrej Černek, and it was developed in order to isolate the PCF from the ambient environment. It is used as a vacuum chamber that can be filled with various gases which can fill the PCF. Thought the fiber which we can transport the gas to the SEM, hence the code name NanoGIS, where the acronym GIS stands for gas injection system. The LBIS is mounted onto the NanoGIS and through glass viewport can guide the laser beam into the PCF. There are additional ports for possible future upgrades, e.g. for contacting various devices that could be inserted inside the NanoGIS. There is a Pirani [47] gauge to measure the vacuum levels. There is a needle valve used for controlling the inlet of the working gas inside the NanoGIS. One of the tubes is used for the fiber and the other one is used to connect the NanoGIS with the SEM chamber, so it can be pumped down by the SEM pumping system. A rendered image of the NanoGIS assembly is in the figure 6.2.

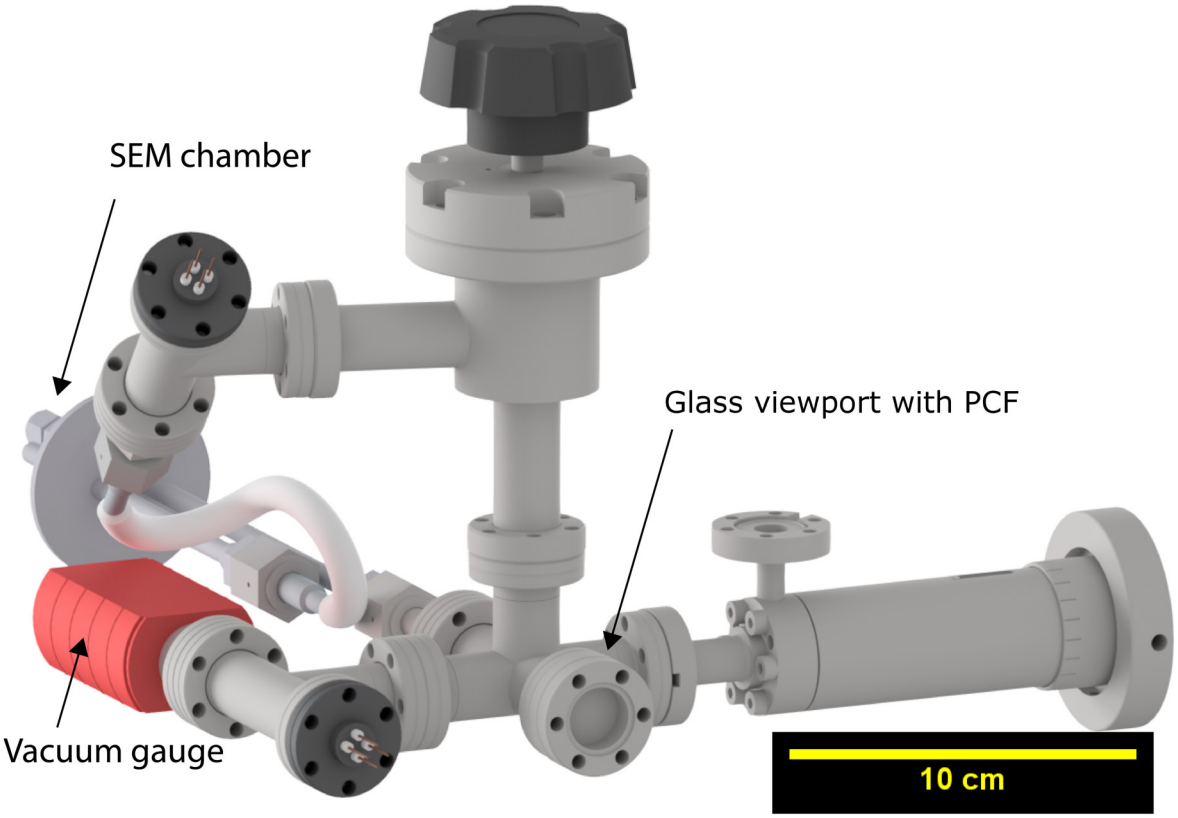

Figure 6.2: A rendered image of the NanoGIS assembly.

6.2. AFM in SEM

A photograph showing the two previously mentioned assemblies put together is in the figure 6.3. The AFM is located inside the SEM chamber. NanoGIS is connected to the special door and a LMA5 fiber is inserted inside the NanoGIS. The LBIS is mounted onto the NanoGIS with its LED lighting on. The NanoGIS is put onto a moving platform to

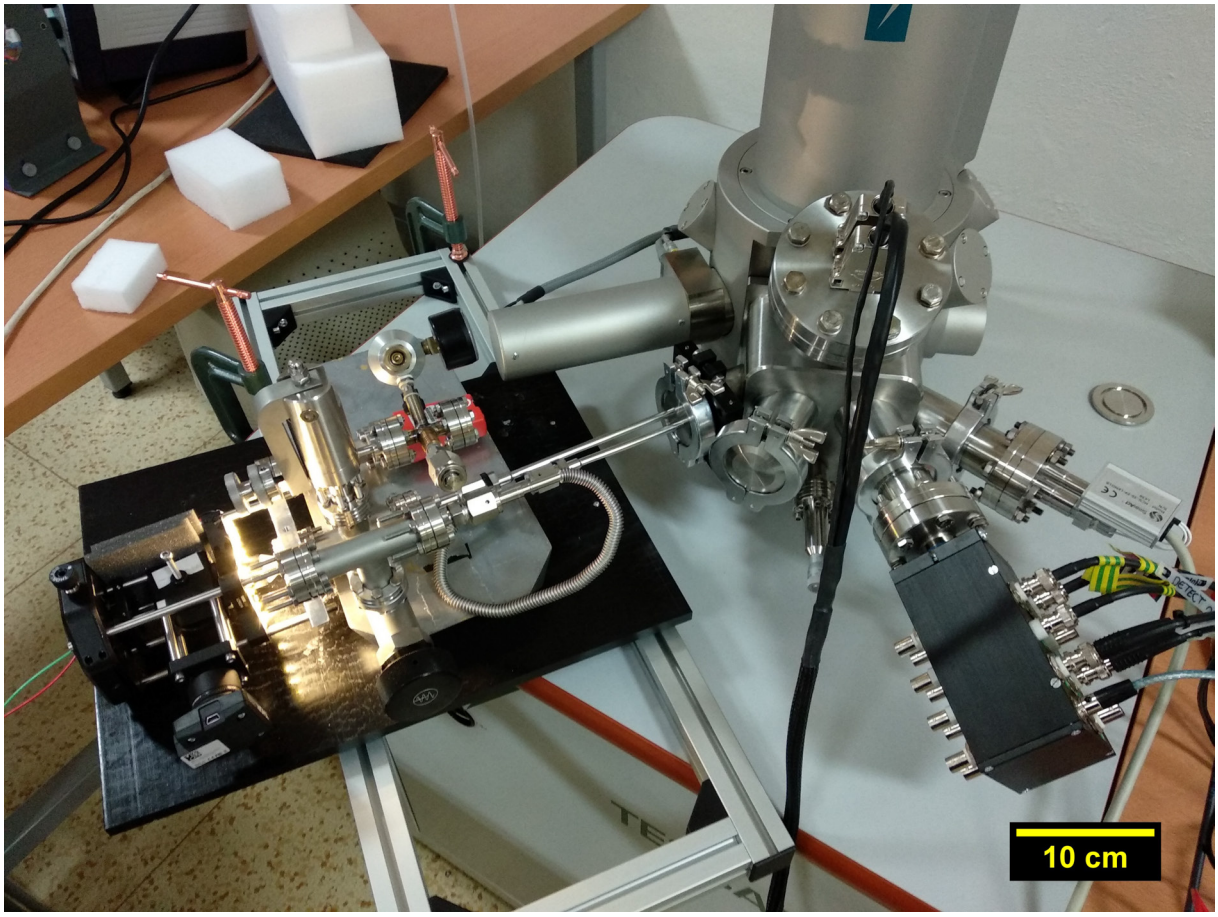

Figure 6.3: A photograph of the special door and NanoGIS assemblies put together. Mounted onto the SEM.

decrease a stress put to the two pipes of the NanoGIS, so the NanoGIS can easily move along the moving door. These two pipes are fragile and caution is required when opening and closing the door. During taking this photograph, the gas can was not inserted into the NanoGIS.

The AFM with the LMA5 fiber is shown in the photograph in the figure 6.4. The AFM microscope is mounted onto the door platform and the LMA5 fiber, attached to the tuning fork, is mounted via the probe holder to the AFM. There is a testing copper sample loaded to the AFM. The LMA5 fiber is secured onto the AFM via Kapton tape. This solution is not only temporary. The LMA5 fiber is bent, although the bending is acceptable considering the optical throughput, it may cause too much strain on the adhesive between the tip and tuning fork. In this configuration, where the tuning fork is set perpendicular to the surface of a sample, that is, the tuning fork is in a shear mode, the AFM can be inserted beneath the SEM objective. In the future, we are planning to place permanently a photodiode [48] next to the place where we are placing samples in order to have a confirmation, that the light passes through the fiber. As it was mentioned previously, even when the LBIS is tuned for maximum optical throughput, any vibration or bump to the table can cause loss of signal, and if the fiber is located in the SEM, there is no other way to tune up the LBIS again. Another reason, to have a photodiode available, is that it can be used for calibrating various laser diodes, that do not have an optical feedback built in which is used for controlling optical power of the laser diode.

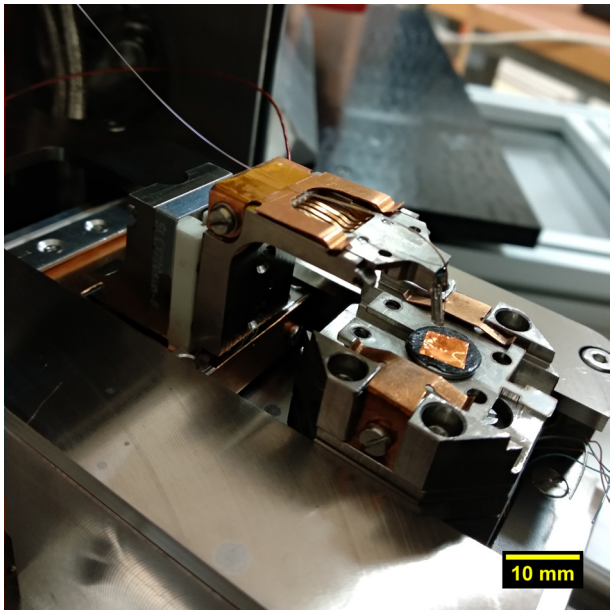

Figure 6.4: A photograph of the AFM inserted inside the SEM chamber, with LMA5 as an AFM probe.

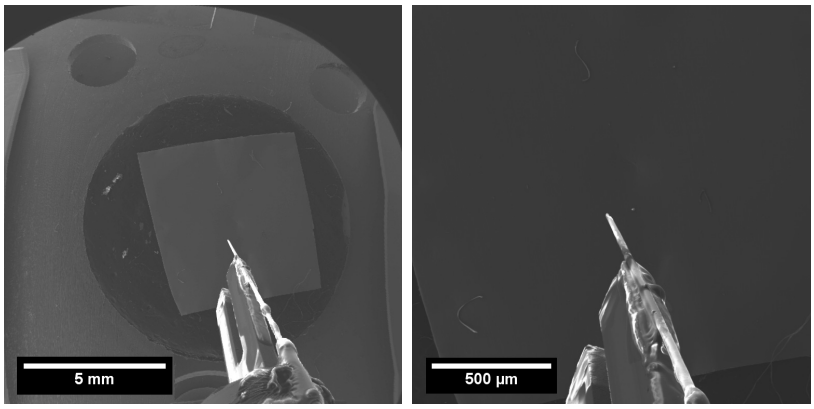

Figure 6.5: A SEM images showing the LMA5 fiber attached to the tuning fork of the AFM.

The SEM images showing the AFM and the LMA5 fiber glued onto the tuning fork are shown in the figure 6.5. We can notice that one electrode of the tuning fork is not being charged, that is because one pin of the tuning fork is grounded. The reason, why the LMA5 fiber, glued on that particular electrode, is being charged, might be the adhesive getting in between the electrode and fiber. It might be beneficial to try to make the fiber grounded, as the built up charge could have a negative effect on the measurement. For example, the built up charge could discharge whenever the tip of the fiber is in a close contact with the sample, which could damage the tip.

We glued the LMA5 fibers onto the tuning fork as is shown in the scheme in the figure 6.6. We put the fiber onto the tuning fork in a way that the fiber is touching the yellow ring of the tuning fork by its acrylate coating, and the fiber's cladding is touching one of the electrodes of the tuning fork. First, the glue is applied to the acrylate area in order to lock the fiber onto the tuning fork. After the glue is dried, a small droplet of the glue

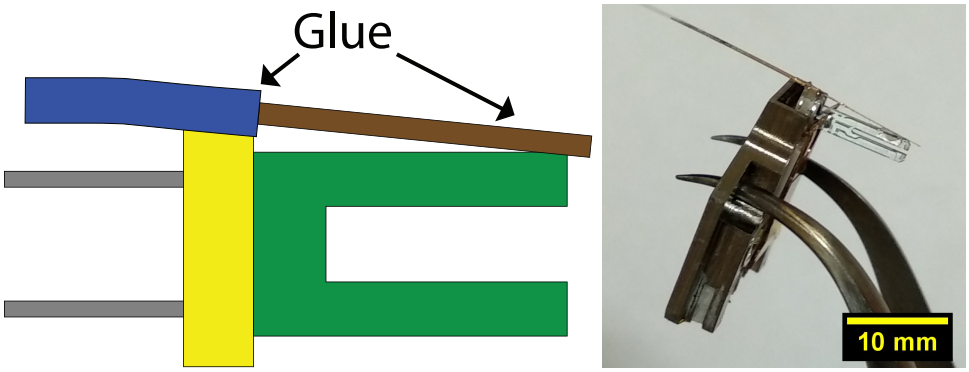

Figure 6.6: A scheme showing a process of gluing the fiber onto the tuning fork. Photograph is in the right image.

is applied to the cladding area (brown) to finish the gluing process. The photograph of the LMA5 fiber glued onto a tuning fork and inserted in a probe holder is shown in the right image in the figure 6.6. After a 24 hour of drying of the glue, the probe is ready for measurement.

We have successfully measured topography with the probes that we prepared. However, the quality of the tips of the probes was not appropriate. That is why the measured topography is not satisfactory, however it proves, that in principle we are able to measure the topography with the prepared LMA5 fibers.

In the case of using tuning forks with glued fibers, we had to set the AFM in an amplitude modulation mode, instead of a frequency modulation mode. This is usual for SPMs that allows SNOM technique [49] of measurement. The reason is low quality factor of the probes. A tuning fork alone should have a quality factor approx. 10 000. When only a droplet of an adhesive is applied onto the tuning fork, the quality factor is reduced to approx. 3000. And when a fiber is glued onto the tuning fork, the quality factor could drop to approx. 500. Our prepared probes had the quality factor equal to approx. 100. This low quality factor is inefficient for a PLL feedback system used in the frequency modulation mode. The reason why the quality factor of our prepared probes is that low, might consist in applying too much of an adhesive onto the tuning fork. Due this low quality factor, we decided that we use the amplitude modulation mode, and we got our first results. An issue could rise when the AFM operates in a vacuum, due to relatively slow changing of the pressure. Any change of pressure affects the amplitude of the tuning probe's oscillations, which could interfere with the amplitude modulation feedback. It takes approx. 10-15 hours to stabilize the pressure inside the Tescan Vega chamber, with the NanoGIS installed. However, any significant change of the frequency response should be suppressed within approx. 20 minutes of pumping. Besides low quality factor, another issue is that the shape of the frequency response of the tuning forks is not satisfactory. Often, there are several peak in the frequency response. The reason might consist in putting a large amount of the glue onto the tuning fork's electrode. More additional weight could severely alter the tuning fork's oscillations. Basically it disrupts tuning fork's symmetry and could add resonant modes. Another reason might be the cladding of the fiber itself, it could behave like a spring, adding resonance modes to the tuning fork. The solution could consist in making the cladding a bit loose, so it does not have a tension and can not interfere with the modes of the tuning fork.

The fibers that we glued onto the tuning fork were only for testing purposes, and they had not been prepared for measuring the topography, i.e. they did not have sharp tips, that are necessary for AFM measurement. The images showing the topography of a calibration sample [50] are shown in the figure 6.7. We measured with two different LMA5 testing fibers.

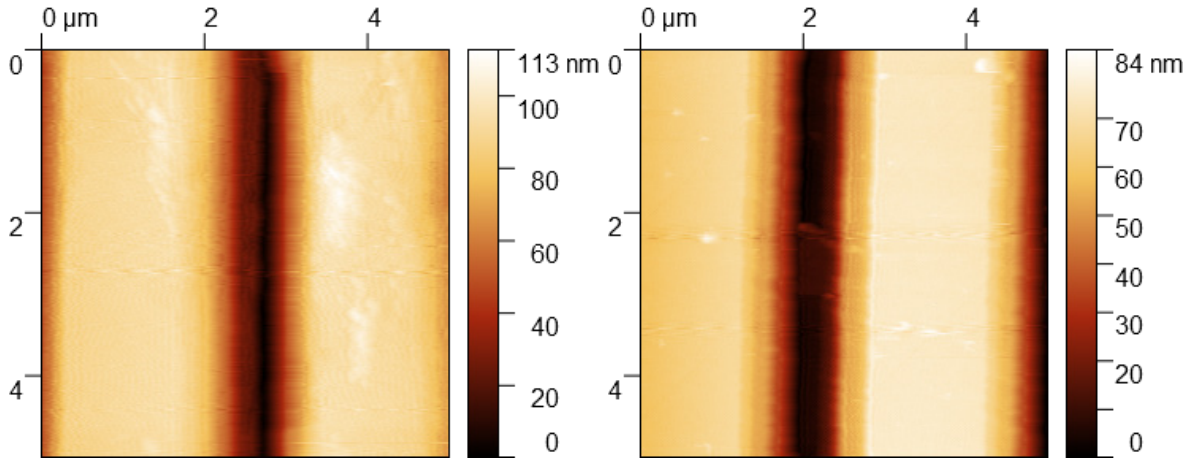

Figure 6.7: A topography of a calibration sample measured with a two different LMA5 testing fibers.

The SNOM probe LMA5 fiber that we prepared in the third session on page 45, have a sharp tip that could be sufficient for AFM measurement. However, the cladding of this fiber is too long, it sticks out of the tuning fork's electrode by approx. 1 cm which is too much. The fiber is shown in the figure 6.8. We decided that in the future, after the fibers are etched and coated with an Au layer, they will be glued onto the tuning fork, and only after that they will be modified, e.g. by the FIB, FIBID etc.

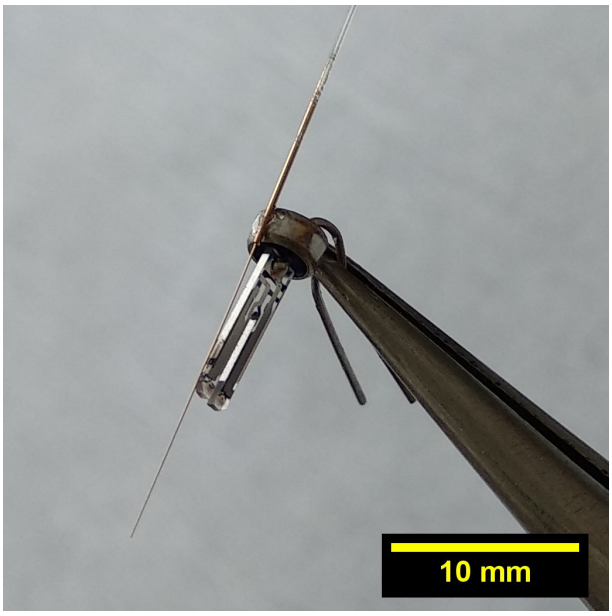

Figure 6.8: A photograph of the SNOM probe LMA5 fiber (prepared in the third session) glued to a tuning fork.

Although, we were not that successful with the probes made using the LMA5 fibers, we have successfully measured a topography of the testing Cu sample with an Akiyama probe [51], and with the AFM located inside the pumped SEM chamber of the Tescan Vega SEM. The images captured by the SEM are in the top of the figure 6.9, the measured topography is in the image below.

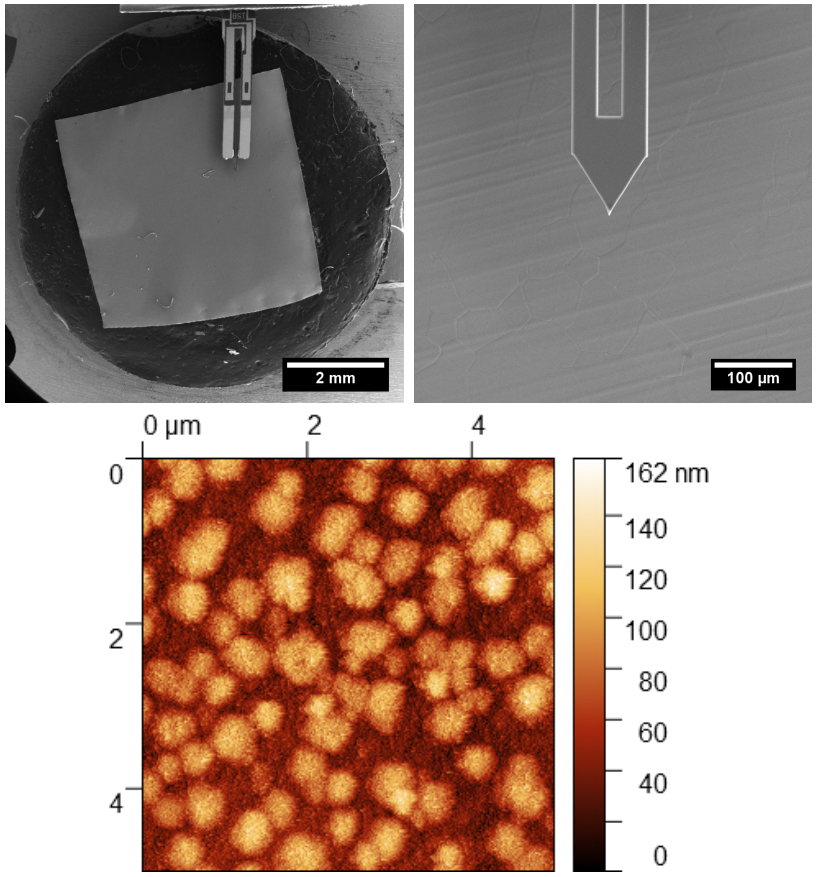

Figure 6.9: A SEM images showing an Akiyama probe ready to measure a topography of the testing Cu sample. Below, a measured topography in a SEM chamber under vacuum conditions.

Conclusion

This diploma thesis deals with a photonic crystal fibers (PCFs), their modification and adaptation for scanning probe microscopy. Brief introduction to photonic crystals and PCFs is presented in the first and second chapter, respectively.

Experiments that involve etching of the PCFs in the HF acid are documented in the third chapter. We developed a technique that allows us to etch the cladding of the PCF without damaging a microstructured region. We also reduced the amount of underetching of acrylate coating. The etching process is repeatable. There is still a room for improving the etching process, utilizing e.g. control of the ambient temperature and vapor pressure of the HF acid.

The experimental work required to assemble two optical setups is described in the fourth chapter. The first one, a laser beam insertion system (LBIS) is used for guiding the light into the PCF, which is inserted inside a GIS assembly. The GIS assembly, together with the LBIS, forms a NanoGIS assembly. NanoGIS is used for gas insertion and pressure control. The other assembly is an optical microscope which is used for inspection of the PCF's endpoint and control of the optical output of the PCF.

The fifth chapter documents the process of attaching a conventional SNOM probe to a solid core of the PCF. We have proven that the light can be coupled from the solid core of the PCF into the SNOM probe, even if there is an adhesive layer at the interconnection between the two fibers. We attempted to make a sharper tip on the SNOM probe for later AFM measurement, however, we have not been successful yet. Although, the SNOM probe modified PCF has a better defined tip, it is too long when glued to a tuning fork. We decided that in the future, the fibers will be glued to a tuning fork after the PCF is etched. And only after that they will be modified.

The sixth and final chapter, summarizes our efforts to insert an AFM into the vacuum chamber of Tescan Vega SEM. For testing purposes, we measured a topography of a test Cu sample under vacuum conditions, using commercially available Akiyama probe. We managed to acquire a topography image of a calibration sample with the PCF probe glued to a tuning fork as well. PCFs used for testing did not have sharp tips, the quality of the measurement was not very good. However, it has proven that in principle we are able to perform an AFM measurement with the probe. In future it should be possible to improve the quality factor of the probes, which is still low. This basically prevents the AFM from operating in a frequency modulation mode. However, an amplitude modulation mode of operation seems to be working sufficient.

The achieved results showed that by mastering the technique of preparation of SNOM probes of specific properties we are able to introduce a working gas and light into the SEM chamber, and perform AFM and SEM measurements. The future research will focus on modifying the surfaces by utilizing the light and working gas, and on improving the quality of the prepared SNOM probes.

Bibliography

[1] KNIGHT, J. C. et al.: *Pure silica single-mode fibre with hexagonal photonic crystal cladding.* Optical Fiber Communication Conference, Vol. 2, 1996.

[2] QAZI, H. H. et al.: *Single-mode D-shaped optical fiber sensor for the refractive index monitoring of liquid.* Journal of Modern Optics, Vol. 63, pp. 1-6, 2015.

[3] TURNER, D. R.: *Etch Procedure for Optical Fibers.* US patent 4469554, 1983.

[4] NenoVision: LiteScope. Available at: https://www.nenovision.com/litescope/litescopetm/description/

[5] JOANNOPOULOS, J. D. et al.: *Photonic Crystals: Molding the Flow of Light. Second Edition.* Princeton University Press, 286p, 2008. ISBN: 978-0-691-12456-8. Available at: http://ab-initio.mit.edu/book/

[6] JOHNSON, S. G. et al.: *Photonic crystals. The Road from Theory to Practice.* Springer, 156p, 2002. ISBN: 0-7923-7751-6.

[7] JACKSON, J. D. *Classical Electrodynamics. 3rd Edition* Wiley, 832p, 1998. ISBN: 978-0-471-30932-1.

[8] ASHCROFT, N. W. et al.: *Solid State Physics* Brooks/Cole, 826p, 1976. ISBN: 0-03-083993-9.

[9] FLOQUET, G.: *Sur les équations différentielles linéaires à coefficients périodiques.* Annales scientifiques de l'École Normale Supérieure, Vol. 12, pp. 47-88, 1883.

[10] BLOCH, F.: *Über die Quantenmechanik der Elektronen in Kristallgittern.* Zeitschrift für Physik, Vol. 52, pp. 555–600, 1929.

[11] SAJEEV J.: *Strong localization of photons in certain disordered dielectric superlattices.* Physical Review Letters, Vol. 58, p. 2486, 1987.

[12] YABLONOVITCH, E.: *Inhibited Spontaneous Emission in Solid-State Physics and Electronics.* Physical Review Letters, Vol. 58, p. 2059, 1987.

[13] MEKIS, A. et al.: *High Transmission through Sharp Bends in Photonic Crystal Waveguides.* Physical Review Letters, Vol. 77, pp. 3787-3790, 1996.

[14] RAJAN, R. et al.: *The Dawn of Photonic Crystals: An Avenue for Optical Computing.* IntechOpen, Vol. 6, pp. 119-132, 2018.

[15] POLI, F. et al.: *Photonic Crystal Fibers. Properties and Applications.* Springer, 233p, 2007. ISBN: 978-1-4020-6325-1.

[16] ZOLLA, F. et al.: *Foundations of Photonic Crystal Fibres.* Imperial College Press, 376p, 2005. ISBN: 1-86094-507-4.

[17] YEH, P. et al.: *Theory of Bragg fiber.* Journal of the Optical Society of America, Vol. 68, pp. 1196-1201, 1978.

[18] FINK, Y. et al.: *A dielectric omnidirectional reflector.* Science, Vol. 282, pp. 1679-1682, 1998.

[19] TEMELKURAN, B. et al.: *Wavelength-scalable hollow optical fibres with large photonic bandgaps for CO 2 laser transmission.* Nature, Vol. 420, pp. 650-653, 2002.

[20] ThorLabs: SM600 - Single Mode Optical Fiber. Available at: https://www.thorlabs.com/drawings/d2dfdc3bdf1978ae-C28C89DF-E40F-EB17-E12310D9533F6849/SM600-SpecSheet.pdf

[21] NKT Photonics: LMA-5 - Single mode 5 μm core fiber. Available at: https://www.nktphotonics.com/wp-content/uploads/sites/3/2015/01/LMA-5.pdf

[22] RUSSELL, P.: *Photonic Crystal Fibers.* Science, Vol. 299, pp. 358-362, 2003.

[23] NKT Photonics: HC-532-02 - Hollow Core Photonic Bandgap Fiber. Available at: https://www.nktphotonics.com/wp-content/uploads/sites/3/2015/01/HC-532.pdf

[24] KNIGHT, J. C. et al.: *Photonic band gap guidance in optical fibers.* Science, Vol. 282, pp. 1476-1478, 1998.

[25] BIRKS, T. A. et al.: *2D photonic band gap structures in fibre form.* Photonic Band Gap Materials, pp. 437-444, 1996.

[26] RICHARDSON, D. J. et al.: *Advances in microstructured fiber technology.* Workshop on Fibres and Optical Passive Components, 2005.

[27] KIANG, K. M. et al.: *Extruded singlemode non-silica glass holey optical fibres.* Electronics Letters, Vol. 38, pp. 546-547, 2002.

[28] EIJKELENBORG, M. van et al.: *Microstructured polymer optical fibre.* Optics Express, Vol. 9, pp. 319–327, 2001.

[29] BARTON, G. et al.: *Fabrication of microstructured polymer optical fibres.* Optical Fiber Technology, Vol. 10, pp. 325–335, 2004.

[30] WU, T. el al.: *Surface plasmon resonance biosensor based on gold-coated side-polished hexagonal structure photonic crystal fiber.* Optics Express, Vol. 25, pp. 20313-20322, 2017.

[31] VAIANO, P. el al.: *Lab on Fiber Technology for biological sensing applications.* Laser Photonic Reviews, Vol. 10, pp. 922-961, 2016

[32] SCHMIDT, M. A. et al.: *Pressure-assisted melt-filling and optical characterization of Au nano-wires in microstructured fibers .* Optics Express, Vol. 19, pp. 12180-12189, 2011.

[33] ThorLabs: FTS4 - Three-Hole Stripping Tool for Fiber Buffers and Jackets. Available at: https://www.thorlabs.com/thorproduct.cfm?partnumber=FTS4

[34] ThorLabs: S90R - Ruby DualScribe™ Fiber Optic Scribe. Available at: https://www.thorlabs.com/thorproduct.cfm?partnumber=S90R

[35] CNI: Single longitudinal mode green laser at 532 nm. Available at: http://www.cnilaser.com/PDF/MSL-III-532.pdf

[36] ThorLabs: Diode-pumped solid state laser diode DJ532-40. Available at: https://www.thorlabs.com/drawings/d2dfdc3bdf1978ae-C28C89DF-E40F-EB17-E12310D9533F6849/DJ532-40-SpecSheet.pdf

[37] ThorLabs: Miniature Temperature Controller MTD415T. Available at: https://www.thorlabs.com/drawings/d2dfdc3bdf1978ae-C28C89DF-E40F-EB17-E12310D9533F6849/MTD415TE-DataSheet.pdf

[38] ThorLabs: Peltier Module TECF2S. Available at: https://www.thorlabs.com/thorproduct.cfm?partnumber=TECF2S

[39] Taiwan Semiconductor: Fast Switching Schottky Barrier Diode DO-35. Available at: https://www.tme.eu/Document/74c28c81e57d48e9bc7d38a28838589e/BAT42-R0.pdf

[40] Vishay: Small Signal Zener Diode 2.7 V. Available at: https://www.tme.eu/Document/2139075dd07d897b7581cf8a6b61c201/BZX55C10-TAP.pdf

[41] Owon: Power Supply Unit P4305. Available at: https://static.eleshop.nl/mage/media/downloads/Owon_P4000.pdf

[42] DVOŘÁK, P.: *Nanofotonika.* Brno: Vysoké učení technické v Brně, Fakulta strojního inženýrství, 2018. 134 s. Vedoucí práce prof. RNDr. Tomáš Šikola, CSc.

[43] Tescan: Gas Injection System. Available at: https://www.tescan.com/en-us/technology/accessories/gis

[44] Tescan: Nanomanipulator. Available at: https://www.tescan.com/en-us/technology/accessories/nanomanipulators

[45] Kleindiek Nanotechnik: SemGlu. Available at: https://www.nanotechnik.com/semglu.html

[46] ČERNEK, O. *Využití speciálního optického vlákna v komoře elektronového mikroskopu.* Brno: Vysoké učení technické v Brně, Fakulta strojního inženýrství, 2019. 43 s. Vedoucí Ing. Michal Pavera, Ph.D.

[47] Edwards: Pirani gauge APG100-XM. Available at: https://shop.edwardsvacuum.com/products/d02601000/view.aspx

[48] Vishay: Silicon PIN photodiode 540 nm VEMD5510CF. Available at: https://www.tme.eu/Document/c62ca3476f688c0c08c4b6ead0401455/VEMD5510CF.pdf

[49] NT-MDT: NTegra Solaris. Available at:
http://www.optophase.com/Brochure/nt%20mdt/98_ntegra_solaris.pdf

[50] NT-MDT: Test grating - TGZ2. Available at:
https://www.ntmdt-tips.com/products/view/tgz2

[51] Nanosensors: Akiyama-Probe. Available at:
https://www.akiyamaprobe.com/

7. List of abbreviations

SPM	Scanning Probe Microscopy
AFM	Atomic Force Microscopy
SNOM	Scanning Near-Field Optical Microscopy
PC	Photonic Crystal
PCF	Photonic Crystal Fiber
HF	Hydrofluoric
PTFE	Polytetrafluoroethylene
PMMA	Polymethyl Methacrylate
PBG	Photonic Bandgap
SEM	Scanning Electron Microscopy
GIS	Gas Injection System
LBIS	Laser Beam Insertion System
CCD	Charge-Coupled Device
LED	Light-Emitting Diode
PC	Physical Connector
FC	Ferrule Connector
TEC	Thermoelectric Cooler
DPSS	Diode-Pumped Solid State
BNC	Bayonet Neill–Concelman
FIB	Focused Ion Beam
FIBID	Focused Ion Beam Induced Deposition
IBAD	Ion Beam Assisted Deposition
IPE	Institute of Physical Engineering
KF	Klein Flange

8. Appendix

In the appendix we give a lists containing items acquired from ThorLabs, that are used in the LBIS and optical microscope.

LBIS		
Part number	Quantity	Part description
CXYZ1/M	1	XYZ Translation Mount for Ø1” Optics, M6 Taps
AD12F	2	SM1-Threaded Adapter for Ø12 mm Cylindrical Components
CFC-8X-A	2	Adj. FC/PC and FC/APC Collimator, f = 7.5 mm
LCP02/M	1	30 mm to 60 mm Cage Plate Adapter, M4 Tap
LM1XY/M	1	Translating Lens Mount for Ø1” Optics

Optical microscope		
Part number	Quantity	Part description
RP01/M	1	Rotation Platform
SM1A3	1	Microscope Objective to SM1 Adapter
SM1A9	1	Adapter, External C-Mount Threads
SM1L03	2	1” Stackable Lens Tube
SM1L05	2	Stackable lens mount for 1”
SM1Z	1	optic-usable depth 1/2
SM2L30	1	Z Translator
MB3045/M	1	3 inch SM2 Lens Tube
BS013	1	Aluminium Breadboard, 300 mm x 450 mm x
RMS10X	1	12.7 mm, M6 taps
SM2L03	2	400-700nm Broadband Beam Splitter Cube
SM2A6	1	25.4mmX25.4
CRM1/M	1	10X Microscope Objective
ER12	2	2 inch Diameter, Stackable Lens Tube,
ER18	2	0.30 inches
DCC1545M	1	SM1 to SM2 Series Thread Adapter
DJ532-40	1	Inline Cage Assembly Rotation Mount
LCP01B	3	Extension Rod 12”
LCP02/M	2	Extension Rod 18”
ER1-P4	1	CMOS Camera, 1280x1024, Monochr., USB2.0
ER3-P4	1	40mW, 532nm, DPSS laser diode
MDT693B	1	60mm Cage Mounting Bracket
CML05	1	30mm to 60mm Cage Plate
DTS25/M	3	Extension Rod 1 inch: Pack of 4
DTSA03/M	1	Extension Rod 3 inch: Pack of 4
TTL180-A	1	CS to C-Mount Adapter, 5mm Length
RP03/M	1	25mm Dovetail Translation Stage
LCP30	1	DTS Stage Angle Bracket Metric
LCP8S	1	30mm 4-Port Prism/Mirror Cage Mount, M4